

İSTANBUL TECHNICAL UNIVERSITY ★ GRADUATE SCHOOL OF SCIENCE
ENGINEERING AND TECHNOLOGY

**CHARACTERIZATION AND APPLICATIONS OF EUTECTIC FREEZE
CRYSTALLIZATION**

M.Sc. THESIS

Mohammadreza AKBARKERMANI

Department of Chemical Engineering

Chemical Engineering Programme

SEPTEMBER 2019

İSTANBUL TECHNICAL UNIVERSITY ★ GRADUATE SCHOOL OF SCIENCE
ENGINEERING AND TECHNOLOGY

**CHARACTERIZATION AND APPLICATIONS OF EUTECTIC FREEZE
CRYSTALLIZATION**

M.Sc. THESIS

Mohammadreza AKBARKERMANI
(506151016)

Department of Chemical Engineering

Chemical Engineering Programme

Thesis Advisor: Doç. Dr. Fatma Elif GENCELİ GÜNER

SEPTEMBER 2019

İSTANBUL TEKNİK ÜNİVERSİTESİ ★ FEN BİLİMLERİ ENSTİTÜSÜ

**ÖTEKTİK DONMA KRİSTALİZASYONUN ÖZELLİKLERİ VE
UYGULAMALARI**

YÜKSEK LİSANS TEZİ

**Mohammadreza AKBARKERMANI
(506151016)**

Kimya Mühendisliği Anabilim Dalı

Kimya Mühendisliği Programı

Tez Danışmanı: Doç. Dr. Fatma Elif Genceli GÜNER

EYLÜL 2019

Mohammadreza AKBARKERMANI, a M.Sc. student of ITU Institute of Science and Technology student ID 506151016, successfully defended the thesis entitled “CHARACTERIZATION AND APPLICATIONS OF EUTECTIC FREEZE CRYSTALLIZATION”, which he prepared after fulfilling the requirements specified in the associated legislations, before the jury whose signatures are below.

Thesis Advisor: Doç. Dr. F. Elif Genceli GÜNER

Istanbul Technical University

Jury Members: Prof. Dr. Hanzade ACMA

Istanbul Technical University

Prof. Dr. Ozgul TASPINAR

Piri Reis University

Date of Submission : 4 September 2019

Date of Defense : 2 September 2019



FOREWORD

This work was supported by Research Fund of Istanbul Technical University. Project Number: MGA-2017-40779. (Bu Çalışma İstanbul Teknik Üniversitesi BAP-Bilimsel Araştırma Projeleri Kordinasyon Birimince Desteklenmiştir. Proje Numarası: MGA-2017-40779.

I especially thank to honorable my dear thesis advisor Assoc. Dr. F. Elif Genceli GÜNER for her lead and giving opportunity to me carry out my master thesis.

In addition, I would like to thank my laboratory partners Ayça ARAT, Mecra SOYSAL, Zeynep EKIN, Pınar YACAN, Gamze NEŞE and Seda CANPOLAT for contributions to perform my laboratory studies.

Finally, I thank very much to my dear family for their motivation, support, helps through the project.

September 2019

Mohammadreza AKBARKERMANI
(Chemical Engineer)



TABLE OF CONTENTS

	<u>Page</u>
FOREWORD	vii
SYMBOLS	xiii
TABLE OF TABLES	xvii
TABLE OF FIGURES	xxi
ÖZET	xxv
1. INTRODUCTION	1
2. EUTECTIC FREEZE CRYSTALLIZATION OF BORIC ACID	3
2.1. Introduction	3
2.1.1 Boron and boron compounds	3
2.1.2 Applications of boron compounds	3
2.1.3 Boron reserves and history	4
2.1.4 Boric acid	4
2.1.5 Eutectic Freeze Crystallization	6
2.1.5.1 Definition and separation principle	6
2.1.5.2 EFC process and its advantages	7
2.1.6 Evaporation	9
2.2 Material And Methods	9
2.2.1 Material and methods for eutectic freeze crystallization	9
2.2.1.1 EFC material	9
2.2.1.2 EFC Experimental setup	10
2.2.1.3 EFC Experimental Procedure	12
2.2.2 Material and methods for evaporation	12
2.2.2.1 Evaporation material	12
2.2.2.2 Evaporation experimental setup	13
2.2.2.3 Evaporation experimental procedure	14
2.2.3 Concentration measurement.....	14
2.2.4 Measurement of crystal size.....	15
2.2.5 Single crystal XRD measurement	16
2.2.6 Production rate	17
2.3 Results and Discussion.....	18
2.3.1 Eutectic point determination	18
2.3.2 Metastable zone width (MSZW) and nucleation rate	20
2.3.3 Salt crystal size and growth kinetics	23
2.3.4 Production rate	29
2.3.5 Crystal structures of boric acid salts around the eutectic point.....	32
2.3.6 Crystallization of boric acid aqueous solution by evaporation	34
2.3.7 Comparison of energy consumption between the evaporation and EFC process.....	38
2.4 Conclusion.....	39
3. MODELING OF HEAT TRANSFER IN EFC PROCESS FOR AQUEOUS SODIUM CHOLORIDE SOLUTION	41

3.1 Introduction	41
3.1.1 Fundamentals of the melt crystallization process	41
3.1.1.1 Supersaturation	42
3.1.1.2 Nucleation	43
3.1.1.3 Crystal growth	44
3.1.2 Eutectic freeze crystallization (EFC)	45
3.1.2.1 Definition and separation principle	45
3.1.2.2 EFC process and its advantages	46
3.1.3 Sodium chloride solution	47
3.1.4 Ice layer formation	48
3.1.5 Usage of a scraper in EFC processes	48
3.1.6 The state of art	49
3.2 Qualitative Analysis of EFC Process	50
3.2.1 Qualitative analysis of EFC process in non-crystallizing condition	50
3.2.1.1 Scraper Power Consumption (P_s)	51
3.2.1.2 Heat transfer through a scraped surface	53
Coolant heat transfer coefficient	54
Solution heat transfer coefficient	56
Heat transfer through the bottom of the crystallizer	58
3.2.1.3 Heat balance under unsteady state	58
3.2.2 Qualitative analysis of EFC process in the crystallizing condition	60
3.2.2.1 Effect of crystal formation on the solution physical properties	61
3.2.2.2 The scraper power consumption	64
3.2.2.3 Heat transfer through a scraped surface	65
3.2.2.4 Heat of crystallization	66
3.3. Results And Discussion	67
3.3.1 Crystallizer specifications and process conditions	67
3.3.2 Heat transfer modeling of sodium chloride solution system in the non-crystallizing condition	68
3.3.2.1 Scraper power consumption	68
3.3.2.2 Heat transfer through a scraped surface	70
Heat transfer through the bottom of the crystallizer	70
Coolant heat transfer coefficient	70
Solution heat transfer coefficient	73
Overall heat transfer coefficient	74
The coolant outlet temperature, the heat flux, and the crystallizer inner bottom temperature	76
3.3.3 Heat balance under unsteady state condition	82
3.3.4 Heat transfer modeling of sodium chloride solution system in the crystallizing condition	86
3.3.4.1 Effect of crystal formation on the solution physical properties	86
3.3.4.2 Effect of crystal formation on Re , α_{sl} and $U'_{overall}$	88
3.3.4.3 Effect of crystal formation on Q , P_s and Hf	90
3.3.4.4 Effect of coolant temperature, coolant volumetric flow rate and scraper rotational speed on ice production	92
3.4 Conclusion	95
REFERENCES	97
Appendix A	113
Appendix A.1: Single crystal XRD Report	113
Appendix A.2: Metastable Zone Width (MSZW) calculations	115

Appendix A.3: Crystal size determination	116
Appendix A.4: Production rate and mass balance.....	118
APPENDIX B	122
Appendix B.1 Calculations in non- crystalizing condition	122
Appendix B.2 Calculations In Crystalizing Condition.....	140
CURRICULUM VITAE.....	153





SYMBOLS

A_t	:Area of tube
a	:Thermal diffusivity
C_{EUT}	:Eutectic concentration
c_{ps}	:Thermal capacity of solution
c_{pi}	:Thermal capacity of ice
c_{pst}	:Thermal capacity of ice
c_{pc}	:Thermal capacity of coolant
d_t	:Diameter of tube
Fr	:Froude number
G	:Rate of crystal growth
g	:Gravity acceleration
H_{fs}	:Solution enthalpy of fusion
H_{fi}	:Ice enthalpy of fusion
H_{fst}	:Ice slurry enthalpy of fusion
L	:Characteristic length
L_t	:Length of tube
M	:Molality
m	:Total mass of solution
m_c	:Mass of crystals
N	:Scraper rotational speed

Nu	:Nusselt number
Ne	:Newton number
n	:Number of scraper blade
P_s	:Scraper power consumption in non-crystallizing condition
Pr	:Prandtl number
$\dot{Q}_{coolant}$:Heat flux from coolant to the solution
\dot{Q}_{loss}	:Heat of loss from the wall of crystallizer
\dot{Q}_{ice}	:Heat of ice crystallization
\dot{Q}_{salt}	:Heat of salt crystallization
\dot{Q}_{sl}	:Heat of crystallization for this study
Re	:Reynolds number
T_{EUT}	:Eutectic temperature
T_{in}	:Coolant inlet temperature
T_{out}	:Coolant outlet temperature
T_{cool}	:Average of inlet and outlet temperature of coolant
T_b	:Temperature of bottom crystallizer
T_{sol}	:Temperature of solution
t	:Time
$U_{overall}$:Overall heat transfer coefficient
\dot{V}	:Coolant volumetric flow rate

Greek symbols

α_{cool}	:Coolant heat transfer coefficient
α_s	:Solution heat transfer coefficient

α_{bottom}	:Heat transfer coefficient through the bottom of crystallizer
ρ_s	:Density of solution
ρ_i	:Density of ice
ρ_{sl}	:Density of ice slurry
ρ_c	:Density of coolant
μ_{Li}	:Chemical potential of liquid
μ_{So}	:Chemical potential of solid
μ_s	:Viscosity of solution
μ_i	:Viscosity of solution
μ_{sl}	:Viscosity of solution
λ_s	:Thermal conductivity of solution
λ_i	:Thermal conductivity of ice
λ_{sl}	:Thermal conductivity of ice slurry
λ_{bottom}	:Thermal conductivity of crystallizer bottom
φ_m	:Crystal mass fraction
φ_v	:Crystal volume fraction
δ	:Thickness of crystallizer bottom
π	:Number pi
$\Delta\mu$:Potential difference
ΔH	:Enthalpy of formation
ΔT_{LN}	:Logarithmic mean temperature difference



TABLE OF TABLES

	<u>Page</u>
Table 2.1: Specifications of the maximum impurity concentration of Boric Acid ...	10
Table 2.2: The amounts of MSZW related parameters for boric acid-water system crystallizing under eutectic conditions.	23
Table 2.3: Crystal size measurement and calculation results	25
Table 2.4: Calculation of the settling velocities.....	32
Table 2.5: Operating Conditions and Energy Requirements.....	38
Table 3.1: Properties of sodium chloride solution at the eutectic point	67
Table 3.2: Physical properties of coolant at different inlet temperature	68
Table 3.3: Variation of Re based on the rotational speed changes.....	69
Table 3.4: The relationship between the volumetric flow rate of coolant and the Reynolds number and Nusselt number.....	71
Table 3.5: Process conditions which obey heat balance in the steady state.....	82
Table A.1: Data collection details for EFC	113
Table A.2: The calculation spread sheet of Figure 2.12.....	115
Table A.3: Characteristic radius calculation from Image J results.	117
Table A.4.1: The data spread sheet to determine the total mass of produced crystals.	118
Table A.4.2: The spreadsheet of weight percent calculation of boric acid in (a) initial solution (b) filtered crystal, (c) passed solution and (d) residual solution.	119
Table A.4.3: The amount of produced ice and boric acid over time.....	121
Table B.1: The variation of the Reynolds number of solution based on the scraper rotational speed.....	122
Table B.2: The scraper power consumption in non-crystalizing conditions as function of rotational speed for flat-blade turbine.....	123
Table B.3: The scraper power consumption in non-crystalizing conditions as function of rotational speed for pitched-blade impeller	123
Table B.4: The scraper power consumption in non-crystalizing conditions as function of rotational speed for marine-type propeller.....	124
Table B.5: The relation between the volumetric flow rate and coolant heat transfer coefficient	124
Table B.6: The solution heat transfer coefficient as a function of the scraper rotational speed.....	125
Table B.7: The calculations spreadsheet of overall heat transfer coefficient as a function of the coolant volumetric flow rate	126
Table B.8: The calculations spreadsheet of overall heat transfer coefficient as a function of the scraper rotational speed.....	127
Table B.9: The calculations spreadsheet of the coolant outlet temperature, the heat flux from the coolant to the solution and the temperature of the inner bottom of crystallizer as a function of the coolant inlet temperature. ..	128
Table B.10: The calculations spreadsheet of the coolant outlet temperature, the heat flux from the coolant to the solution and the temperature of the inner	

bottom of crystallizer as a function of the coolant volumetric flow rate.	129
Table B.11: The calculations spreadsheet of the coolant outlet temperature, the heat flux from the coolant to the solution and the temperature of the inner bottom of crystallizer as a function of the scraper rotational speed	130
Table B.12: The calculations spreadsheet of the time required to cool down the solution at $T=-30^{\circ}\text{C}$	132
Table B.13: The calculations spreadsheet of the time required to cool down the solution at $T=-29^{\circ}\text{C}$	133
Table B.14: The calculations spreadsheet of the time required to cool down the solution at $T=-28^{\circ}\text{C}$	134
Table B.16: The calculations spreadsheet of the time required to cool down the solution at $V=10^{-3}\text{m}^3\text{s}^{-1}$	135
Table B.17: The calculations spreadsheet of the time required to cool down the solution at $V=5*10^{-3}\text{m}^3\text{s}^{-1}$	136
Table B.18: The calculations spreadsheet of the time required to cool down the solution at $V=0.01\text{m}^3\text{s}^{-1}$	136
Table B.19: The calculations spreadsheet of the time required to cool down the solution at $V=5*10^{-2}\text{m}^3\text{s}^{-1}$	137
Table B.20: The calculations spreadsheet of the time required to cool down the solution at $N=50\text{rpm}$	138
Table B.21: The calculations spreadsheet of the time required to cool down the solution at $N=100\text{rpm}$	138
Table B.22: The calculations spreadsheet of the time required to cool down the solution at $N=150\text{rpm}$	139
Table B.23: The calculations spreadsheet of the solution physical properties as a function of ice mass fraction.....	140
Table B.24: The calculations spreadsheet of the Reynolds number, Prandtl number, Nusselt number solution heat transfer coefficient and overall heat transfer coefficient as a function of ice mass fraction	141
Table B.25: The calculations spreadsheet of the heat flux from the coolant to the solution, the scraper power consumption and the slurry enthalpy as a function of the ice mass fraction.....	141
Table B.26: The time required to produce various amounts of ice crystals at $T_{cool}=-30^{\circ}\text{C}$	142
Table B.27: the time required to produce various amounts of ice crystals at $T_{cool}=-29^{\circ}\text{C}$	143
Table B.28: The time required to produce various amounts of ice crystals at $T_{cool}=-28^{\circ}\text{C}$	144
Table B.29: The time required to produce various amounts of ice crystals at $T_{cool}=-27^{\circ}\text{C}$	145
Table B.30: Time required to produce various amounts of ice crystals at $V=10-3\text{m}^3\text{s}^{-1}$	146
Table B.31: The time required to produce various amounts of ice crystals at $V=5*10^{-3}\text{m}^3\text{s}^{-1}$	146
Table B.32: The time required to produce various amounts of ice crystals at $V=0.01\text{m}^3\text{s}^{-1}$	147
Table B.33: The time required to produce various amounts of ice crystals at $V=0.05\text{m}^3\text{s}^{-1}$	148

Table B.34: The time required to produce various amounts of ice crystals at $N=150$ rpm.....	149
Table B.35: The time required to produce various amounts of ice crystals at $N=100$ rpm.....	150
Table B.36: The time required to produce various amounts of ice crystals at $N=50$ rpm.....	151





TABLE OF FIGURES

	<u>Page</u>
Figure 2.1: The crystal structure of boric acid (Shuvalov and Burns 2003a).	5
Figure 2.2: General phase diagram for a binary aqueous solution.....	7
Figure 2.3: Schematic representation of EFC process.	8
Figure 2.4: (a) Crystallizer; (b) Cooling machine; (c) Agilent digital multimeter photos.....	11
Figure 2.5: The experimental set-up of EFC process.....	11
Figure 2.6: The evaporation experiment setup.	13
Figure 2.7: Automatic titrator (Schott Titronic Universal).	15
Figure 2.8: Crystal imaging via microscope set-up.....	16
Figure 2.9: Bruker D8 VENTURE Crystal XRD photo.....	17
Figure 2.10: The vacuum filtration photo.	18
Figure 2.11: Concentration-Temperature diagram for boric acid.	19
Figure 2.12: Temperature-Time diagram of boric acid.....	20
Figure 2.13: Metastable zone width versus the cooling rate of boric acid solution..	22
Figure 2.14: Typical pictures of boric acid crystals (left) and ice crystals (right) under EFC operation.....	23
Figure 2.15: Time vs. Crystal characteristic radius graph for (a) $\Delta T = 3.6\text{ }^{\circ}\text{C}$, (b) $\Delta T = 4.3\text{ }^{\circ}\text{C}$, (c) $\Delta T = 6.5\text{ }^{\circ}\text{C}$	27
Figure 2.16: Growth rate of boric acid versus the supersaturation under eutectic operation conditions	28
Figure 2.17: Mass growth rate of boric acid versus the supersaturation under eutectic operation conditions	29
Figure 2.18: Produced amounts of salt (orange) and ice (blue) versus time.....	31
Figure 2.19: Temperature-Time Graph of Boric Acid Solution.....	33
Figure 2.20: Photo of crystal used for structure determination in single crystal XRD measurement.....	33
Figure 2.21: Crystal Stacking of H_3BO_3	34
Figure 2.22: Intermolecular Hydrogen Bonds of H_3BO_3	34
Figure 2.23: Main Structure Pictures of H_3BO_3	34
Figure 2.24: Temperature-Time Graph of Boric Acid Solution for evaporation method	36
Figure 2.25: Formed boric acid crystal by evaporation	37
Figure 3.1: Solubility diagram showing stable, labile and metastable zones	42
Figure 3.2: The relationship between free energy with undercooling.....	43
Figure 3.3: General phase diagram for binary aqueous solutions.	45
Figure 3.4: Schematic representation of EFC process	46
Figure 3.5: Phase diagram of NaCl solution according to Taschenbuch für Chemiker und PhysikernBand	47

Figure 3.6: Scale formation during the EFC process.	48
Figure 3.7: Scheme of heat transfer in a crystallizer in non-crystallizing condition	50
Figure 3.8: Scheme of the selected impeller	52
Figure 3.9: (a) flat-blade turbine, (b) pitched-blade impeller (c) marine-type propeller,	52
Figure 3.10: Schematic representation of heat transfer in coolant surface.	54
Figure 3.11: Development of the temperature profile after each scraper blade pass.	56
Figure 3.12: The heat balance in the EFC process under unsteady state and in non- crystallizing condition.....	59
Figure 3.13: The heat balance in the crystallizing condition.	60
Figure 3.14: The enthalpy of solution as a function of sodium chloride concentration	63
Figure 3.15: The scraper power consumption in non-crystallizing conditions as a function of rotational speed for (square) flat-blade turbine, (circle) pitched-blade impeller, (triangle) marine-type propeller.....	69
Figure 3.16: Relation between the volumetric flow rate and coolant heat transfer coefficient	72
Figure 3.17: The relationship between rotational speed and solution heat transfer coefficient	73
Figure 3.18: The effect of rotational speed on the overall heat transfer coefficient .	74
Figure 3.19: The overall heat transfer coefficient as a function of coolant volumetric flow rate	75
Figure 3.20: The coolant outlet temperature (square), the heat flux from the coolant to the solution (circle) and the temperature of crystallizer inner surface (triangle) as a function of coolant inlet temperature.	77
Figure 3.21: The coolant outlet temperature, the heat flux from coolant to the solution and temperature of crystallizer inner surface as a function of coolant volumetric flow rate	79
Figure 3.22: The coolant outlet temperature, the heat flux from coolant to the solution and temperature of crystallizer inner surface as a function of the scraper rotational speed.	81
Figure 3.23: The solution temperature as a function of time at the various coolant temperature.	83
Figure 3.24: The solution temperature as a function of coolant volumetric flow rates over time	84
Figure 3.25: The solution temperature as a function of time in different amounts of stirrer rotational speed.	85
Figure 3.26: Density, thermal conductivity, specific heat and viscosity of slurry as a function of ice mass fraction.....	86
Figure 3.27: Reynolds number, Nusselt number, heat transfer coefficient of slurry and overall heat transfer coefficient as a function of ice mass fraction..	89
Figure 3.28: The heat flux, scraper power consumption and enthalpy of slurry as a function the ice mass fraction.	91
Figure 3.29: The ice mass as a function of time at various amount of coolant temperature	92
Figure 3.30: Ice mass production versus time at different coolant volumetric flow rate	93
Figure 3.31: The ice mass as a function of time at different scraper rotational speed	94

CHARACTERIZATION AND APPLICATIONS OF EUTECTIC FREEZE CRYSTALLIZATION

SUMMARY

One of the serious problems throughout the world is to access fresh water. Natural water and industrial wastewater are suitable sources to provide fresh water. Besides, most of these water sources contain valuable minerals. It is important to choose a sustainable method to provide fresh water and extract valuable minerals economically. One of the novel technologies to gain water and valuable minerals from an impure fluent is Eutectic Freeze Crystallization (EFC). EFC is a more economical way in comparison with similar methods such as evaporation. Separation principle of EFC is to isolated ice and salt from a saline solution based on their density differences at the eutectic point.

Boron compounds have many usage areas in different industrial operations. Turkey has the 2/3 of overall earth's boron deposits and huge amount of production and usage rate bringing up a waste problem. These wastes causing environmental problems, air, soil and water pollution. A both ecologically friendly and economically beneficial option is recovery of boron minerals from waste water ponds. In this section, boric acid which is one of the major boron compounds is investigated to recover from an aqueous solution. Eutectic Freeze Crystallization (EFC) method is applied to extract ice and boric acid from the solution. In this study, boric acid-water system eutectic point is confirmed at $-0.75\text{ }^{\circ}\text{C}$ and 2.5 wt% and

- the nucleation rate of the boric acid crystals
- growth rate of the boric acid crystals
- production rate of the boric acid and ice crystals

under batch eutectic operation are investigated.

The nucleation rate is proportional to the Metastable Zone Width (MSZW) and calculated based on that. In this research, MSZW is the difference between the minimum temperature of the solution and the eutectic temperature. In this study, the nucleation rate is calculated based on MSWZ and the nucleation rate constant and nucleation order are determined.

Another important parameter to characterize boric acid and water system for EFC process is the growth rate. the growth rate is the process that nuclei begin to grow into visible size. In this study, ice and salt crystals grew around 1 hour residence time, under eutectic conditions. The crystal particles were screened via OLYMPUS BX51. Moreover, the crystal size was determined by Image J software.

In this study production rate for ice and salt is considered. the production rate is a significant parameter which can show the ability of the system to extract the

component. In this investigation, the production rate of ice and boric acid salt is determined. However, due to the experiments were carried at the ambient temperature and above the melting point of ice, there is a contradiction in the production rate of ice.

In comparison with EFC process and evaporation for boric acid-water system, EFC method consumes much less energy than evaporation method. Eutectic Freeze Crystallization provides an attractive method for extraction of boric acid salt from its aqueous solution. In this study, In addition to the energy consumption, the growth rate of boric acid crystals in EFC were compared with the evaporation method. According to the result of this study, the growth rate of boric acid crystals in EFC process is much less than the evaporation method.

At the end of this section, the crystal structure of boric acid is considered around the eutectic point via single crystal XRD method. Unit cell of boric acid (H_3BO_3) synthesized around eutectic point, is reported to be different from literature studies.

One of the most abundant salts on earth is sodium chloride which is contained in most of natural sources and industrial wastewaters. In previous studies, extraction of sodium chloride from saline solutions via EFC was compared to various conventional methods, such as evaporation. EFC process was reported to be energetically more favorable.

In the second part of thesis, separation of ice and sodium chloride by a batch EFC process is considered theoretically. In this regard, at first, the heat transfer at the different process condition in the non-crystallizing condition with the constant solution temperature at the eutectic temperature (T_{EUT}) is evaluated.

In this condition, the inlet temperature of coolant (T_{in}) is directly related to the outlet temperature of coolant (T_{out}) and the inner bottom of crystallizer (T_b) and is inversely related to the heat flux from the coolant to the solution (\dot{Q}_{cool}). In this condition, the coolant volumetric flow rate (\dot{V}) does not affect significantly T_{out} , \dot{Q}_{cool} and T_b at higher flow rates. Furthermore, in non-crystallizing condition T_{out} , \dot{Q}_{cool} and T_b are not influenced significantly by the scraper rotational speed (N). In the second step of non-crystallizing condition, unsteady state condition of the solution temperature is considered. In this condition, the cooling rate of the solution is directly proportional to \dot{V} and inversely related to N and the coolant temperature (T_{cool}).

Finally, heat transfer in the crystallization condition and effect of crystal particles on the physical properties of the solution are determined. Due to mainly formed ice crystals, properties of ice is assumed as the whole crystal particles's property. Results show that, effect of ice crystals on the physical properties of the solution except viscosity is negligible. Furthermore, time required to produce specific amounts of crystals is directly related to coolant temperature, inversely related to coolant volumetric flow rate and inversely and directly related to the scraper rotational rates at speeds lower and higher than 100 rpm, respectively.

ÖTEKTİK DONMA KRİSTALİZASYONUN ÖZELLİKLERİ VE UYGULAMALARI

ÖZET

Dünyadaki önemli sorunlardan birisi tatlı suya ulaşmaktır. Doğal su ve endüstriyel atık su, tatlı su sağlamak için uygun kaynaklardır. Ayrıca, bu su kaynakları çoğu değerli mineraller içerir. Tatlı su sağlamak ve değerli mineralleri ekonomik olarak çıkarmak için sürdürülebilir bir yöntem seçmek önemlidir. Saf olmayan bir akışkandan su ve değerli mineraller elde etmek için kullanılan yeni teknolojilerden biri Ötektik Donma Kristalizasyonu (ÖDK)'dur. ÖDK, evaporasyon gibi benzer ayırma yöntemleriyle karşılaştırıldığında daha ekonomik bir yoldur. ÖDK 'nun ayrılma ilkesi, ötektik noktada tuzlu sudan buz ve tuz elde edip, yoğunluk farklılıklarına dayanarak ayırmaktır.

Bor bileşikleri, farklı endüstriyel işlemlerde birçok kullanım alanına sahiptir. Dünyadaki bor yataklarının 2 / 3'ü Türkiye'dir. Ek olarak Türkiye, atık sorununa yol açan büyük miktarda üretim kapasitesine ve kullanım oranına sahiptir. Bu atıklar çevre sorunlarına, hava, toprak ve su kirliliğine neden olmaktadır. Hem çevre dostu hem de ekonomik açıdan faydalı bir seçenek, bor minerallerinin atık su havuzlarından geri kazanılmasıdır.

Bu bölümde, başlıca bor bileşiklerinden biri olan borik asit, sulu bir çözeltiden geri kazanılmak üzere incelenmiştir. Çözeltiden buz ve borik asidi çıkarmak için Ötektik Donma Kristalizasyonu (ÖDK) yöntemi uygulanır.

Bu çalışmada, borik asit-su sisteminin ötektik noktası $-0.75\text{ }^{\circ}\text{C}$ ve bu sıcaklıkta konsantrasyonu ağırlık olarak % 2.5 olarak doğrulanmıştır. Ayrıca,

- Borik asit kristallerinin çekirdeklenme oranı,
- Borik asit kristallerinin büyüme hızı,
- Borik asit ve buz kristallerinin üretim hızı,

kesikli ötektik sistemde incelenmiştir.

Çekirdeklenme hızı Metastabil Bölge Genişliğine (MSBG) ile orantılıdır ve buna göre hesaplanır. Bu çalışmada, MSBG, çözeltinin minimum sıcaklığı ile ötektik sıcaklık arasındaki farktır. Bu çalışmada çekirdeklenme hızı MSBG esas alınarak hesaplanmış ve çekirdeklenme hızı sabiti ve çekirdeklenme sırası belirlenmiştir.

ÖDK prosesi için borik asit ve su sistemini karakterize eden diğer bir önemli parametre ise büyüme hızıdır. Büyüme hızı, çekirdeklerin görünür büyüklükte büyümeye

başladığı procestir. Bu çalışmada, buz ve tuz kristalleri ötektik koşullar altında yaklaşık 1 saat tutularak büyümeleri gözlemlenmiştir. Kristal parçacıkları OLYMPUS BX51 ile görüntülenmiştir. Ek olarak, kristal boyutu Image J yazılımıyla belirlenmiştir.

Bu çalışmada, buz ve tuz için üretim hızı ele alınmıştır. Üretim hızı, sistemin ekstraksiyon kabiliyetini gösteren önemli bir parametredir. Bu araştırmada, buz ve borik asit tuzu üretim hızı incelenmiştir. Bununla birlikte, deneyler ortam sıcaklığında ve buzun erime noktasının üstünde yapıldığı için, buzun üretim hızında bir tutarsızlık gözlenmiştir.

Borik asit-su sistemi için, ÖDK işlemi ve evaporasyon ile karşılaştırıldığında, ÖDK yöntemi evaporasyon yönteminden çok daha az enerji tüketir. Böylece, Ötektik Donma Kristalizasyonu, borik asit tuzunun sulu çözeltisinden ekstrakte edilmesi için alternatif bir yöntem sağlar. Bu çalışmada, enerji tüketimine ek olarak, ÖDK 'deki borik asit kristallerinin büyüme hızı evaporasyon yöntemiyle karşılaştırılmıştır. Bu çalışmanın sonucuna göre, ÖDK işleminde borik asit kristallerinin büyüme hızı evaporasyon yönteminden çok daha düşüktür.

Bu bölümün sonunda, borik asidin kristal yapısı ötektik nokta etrafında tek kristalli XRD metodu ile değerlendirilmiştir. Ötektik nokta çevresinde sentezlenen borik asit (H_3BO_3) birim hücrelerinin literatür çalışmalarından farklı olduğu gözlemlenmiştir.

Yeryüzündeki en çok bulunan tuzlardan biri, doğal kaynakların ve endüstriyel atık suların çoğunda bulunan sodyum klorürdür. Önceki çalışmalarda, sodyum klorürün ÖDK yoluyla tuzlu su çözeltilerinden ekstraksiyonu evaporasyon gibi çeşitli geleneksel yöntemlerle karşılaştırılmıştır. Bu çalışmalarda ÖDK sürecinin enerjik olarak daha avantajlı olduğu belgelenmiştir.

Yeryüzündeki en çok bulunan tuzlardan biri, doğal kaynakların ve endüstriyel atık suların çoğunda bulunan sodyum klorürdür. Önceki çalışmalarda, sodyum klorürün ÖDK yoluyla tuzlu su çözeltilerinden ekstraksiyonu evaporasyon gibi çeşitli geleneksel yöntemlerle karşılaştırılmıştır. Bu çalışmalarda ÖDK sürecinin enerjik olarak daha avantajlı olduğu belgelenmiştir.

Bu çalışmada, buz ve sodyum klorürün çözeltilerden kesikli ÖDK işlemi ile ayrılması teorik olarak ele alınmıştır. Bu bağlamda, ilk önce, farklı işlem koşullarında, kristalleşmeyen durumdaki ötektik sıcaklıkta sabit bir çözelti sıcaklığı (T_{EUT}) ile ısı transferi değerlendirilmiştir. Soğutucunun giriş sıcaklığı (T_{in}) doğrudan soğutucunun çıkış sıcaklığı (T_{out}) ve kristalleştiricinin (T_b) iç sıcaklığı ile doğrudan ilgili ve soğutucudan çözeltiliye olan ısı akısı (\dot{Q}_{cool}) ile ters orantılıdır.

Bu durumda, soğutucu hacimsel akış hızı (\dot{V}) daha yüksek akış hızlarında T_{out} , \dot{Q}_{cool} ve T_b 'yi önemli ölçüde etkilemez. Ayrıca, kristallenmenin olmadığı durumda (T_{out}), (\dot{Q}_{cool}) ve (T_b), karıştırıcı/kazıyıcı dönme hızından (N) önemli ölçüde etkilenmez. Kristalleşmeyen durumun ikinci aşamasında, çözelti sıcaklığının kararsız hal durumu göz önünde bulundurulmuştur. Bu durumda, çözeltilinin soğutma hızı doğrudan \dot{V} ile doğrudan orantılı ve N ve soğutucu sıcaklığı (T_{cool}) ile ters orantılıdır. Son olarak, kristalleşme koşulundaki ısı transferi ve kristal parçacıklarının çözeltilinin fiziksel özellikleri üzerindeki etkisi belirlenmiştir.

Çoğunlukla oluşan buz kristalleri nedeniyle, buz parçacıkları tüm kristal parçacıklarının özelliği olarak kabul edilir. Sonuçlar, buz kristallerinin, viskozite dışındaki çözeltilinin fiziksel özellikleri üzerindeki etkisinin önemsiz olduğunu

göstermektedir. Ayrıca, belirli miktarlarda kristal üretmek için gereken süre, soğutucu akışkan sıcaklığıyla doğrudan ilgilidir, soğutucu akışkanın hacimsel akış hızı ile ters olarak ilişkilidir ve sırasıyla 100 rpm'den daha düşük ve daha yüksek hızlarda karıştırıcı/kazıyıcı dönüş hızlarıyla ters ve doğrudan ilgilidir.





1. INTRODUCTION

One of the most common concerns which affects people all over the world is insufficient access to clean water which can threaten even water-rich areas (Malato et al. 2009). Furthermore, the rapidly growing population, energy demand, and industrialization are causing a lot of waste problems. These problems will continue to increase, and it is expected to increase globally up to 70 percent by 2025 (Hoornweg and Bhada-Tata 2012). One of the main environmental problems facing industries is hypersaline production because the disposal of this kind of production has the high potential to contaminate groundwater (Randall et al., 2011). Therefore, the novel and economical technologies must be considered to extract water and also valuable minerals such as salt from a natural source like the sea and the wastewater produced from an industrial process (Pramanik et al. 2016). According to previous studies, in addition to fresh water the salts in brine is recovered by evaporation, nanofiltration, calcinations, membrane crystallization, electrolytic processes, Eutectic Freeze Crystallization and so on (Kim, 2011). Eutectic Freeze Crystallization (EFC) which is novel technology, offers mostly efficient separation method of brines and concentrates in order to recover pure water and salt. Eutectic Freeze crystallization which advances based on the density differences between the ice and salt can be better alternative for evaporative crystallization and cooling crystallization which are the conventional methods to separate highly soluble salts from their aqueous solution.

In this study, the primary purpose is characterization of the Eutectic Freeze Crystallization of sodium chloride-water ($\text{NaCl-H}_2\text{O}$) and boric acid-water ($\text{H}_3\text{BO}_3\text{-H}_2\text{O}$).

In the study, the first stream, the synthetic boric acid system, was used for the characterization of the Eutectic Freeze Crystallization of boric acid-water system in the 1 liter experimental apparatus of the EFC. In this case, all experiments were initially carried out using a 2.5% boric acid aqueous solution. After confirming the eutectic point of boric acid-water system which is $-0.75\text{ }^\circ\text{C}$, growth kinetics of the boric acid crystals under batch eutectic operation is investigated. The obtained quantities,

sizes and growth rates of the crystals and the energy required to form the crystals by EFC are then compared to conventional Evaporative Crystallization (EvC) method. According to the results, it was observed that the crystal growth rates are close to each other for both methods. However, EFC method consumes much less energy than EvC method. In addition, the crystal structure of the boric acid salt which synthesized around the eutectic point crystallization has compared with crystal structure as the structure synthesized at room temperature that documented in the literature.

Finally, the heat transfer in a batch Eutectic Freeze Crystallization for the aqueous sodium chloride solution was considered. In this regard, the main parameters like the coolant temperature to control and optimize dependent variables such as heat flux from the coolant to the solution, in both non-crystallizing and crystallizing conditions were discussed. The following actions were considered in the context of this section.

- The scraper power consumption and heat flux from the coolant to the solution in non-crystallizing steady state.
- The required time to cool down the solution until the eutectic temperature and the effect of independent parameters such as the solution temperature on this time.
- The scraper power consumption and the heat flux from the coolant to the solution under the crystallizing condition;

The required time to produce crystals in the crystallizing condition and effect of independent parameters such as coolant temperature on this time.

2. EUTECTIC FREEZE CRYSTALLIZATION OF BORIC ACID

2.1. Introduction

2.1.1 Boron and boron compounds

Boron is a nonmetallic element which can be found in nature as boric acid (H_3BO_3) and sodium borate ($\text{Na}_2\text{B}_4\text{O}_7 \cdot 10\text{H}_2\text{O}$) that is known as borax (Farhat et al., 2013). In 1808, for the first time boron was generated in an impure form by Sir Humphrey Davy who electrolyzed molten boric acid. Also in this year, Gay-Lussac and Thenard synthesized boron by the reaction of potassium with boric acid (E. House and E. House, 2016).

Naturally, most of the earth's soil contains boron with average concentration between 10 ppm and 20 ppm. However, concentrated and suitable size of boron minerals which are mainly in the form of boron-oxygen compounds, are rare. These compounds are mainly found in Turkey, the United States and some other regions where are arid with a history of hydrothermal activity such as volcanism (Woods, 1994a).

2.1.2 Applications of boron compounds

Boron is a vital nutrient which plays a significant role in nutrition and metabolism. However, boron influences steroid hormone metabolism and decreases cancer risk (Hosmane, 2012). Furthermore, boron has remarkable effects on the plants. Deficiency of boron causes terminal shoots death, short internodes, and even death of plants (M. Shaaban, 2010; Kabay et al., 2010). Although boron is necessary for the organism, the excessive amount can act toxic. Thus, the concentration of boron in a water stream must be considered (Parks And Edwards, 2005).

In industry, boron minerals are mainly applied to produce glass (52%) such as insulation type glass fiber, textile type glass fiber, and borosilicate glass. Another main usage of boron minerals is in the ceramic industry (12%). In the ceramic industry, boron minerals are mostly applied in the generation of ceramic glaze (Sokmen and

Buyukakinci, 2018). Boron compounds are also used in nuclear technology, heat resistant materials, dyestuff, detergent and food industry (Nasef et al., 2014).

2.1.3 Boron reserves and history

The estimated boron ore resources are by approximately 885 billion tons throughout the world (Mahdi et al., 2017). Turkey is the largest producer of boron compounds in the world and has most of the production with 39% followed by USA 24%, Argentina 14% and Chile 10% (Schlesinger and Vengosh, 2016).

For the first time, mining of the boron compounds was started in Chile in 1852. In the following, the boron element was discovered in Clear Lake by John Veatch. Boron mining in Turkey was started in 1865 by a French company called Campaign Industrielle Desmazures, with mining of the calcium borate pandermite (priceite, $4\text{CaO}_5\text{B}_2\text{O}_3 \cdot 7\text{H}_2\text{O}$) from the Aziziye Mine near Susurluk (Kitahama et al. 2005; Woods 1994b). The demand increase encouraged companies to extract boron compounds in large scale in Turkey and USA (Kitahama et al., 2005).

2.1.4 Boric acid

One of the most stable and soluble components of boron is orthoboric acid, which is also known as boric acid. Boric acid is an inorganic acid and its chemical formula is H_3BO_3 (Prutting and Cervený 1998; Howe 1998). Boric acid is a white and powdery crystalline solid. Molecular weight, specific gravity at 20°C , boiling point and melting point of boric acid are 61.8 g/mol, 1.44, 300°C and 171°C , receptively (Pohanish 2017). In the crystal structure of boric acid, three acid molecules bind to a boron atom. The hydrogen atom of the acid molecule is connected to an oxygen atom directly which is at a greater distance from the oxygen atoms of adjacent molecules (Bethell and Sheppard 1955). The crystal structure of the boric acid molecule is shown in Figure 2.1.

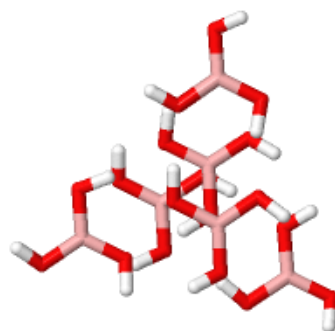


Figure 2.1: The crystal structure of boric acid (Shuvalov and Burns 2003a).

Boric acid is a benign component in consumer components such as mattresses, futons and furniture because intrinsic toxicity is low in these stuffs (Horrocks and Price, 2008).

Boric acid can be extracted from an aqueous solution either (a) by physical extraction such as crystallization, or (b) by a chemical reaction which makes an ester (Matsumoto et al., 1997; L.YuS.M.Reutzl-Edens, 2003).

2.1.6 Boric acid removal

Although boric acid is known to be a safe component in the environment, it might be dangerous to human beings and animals in significant doses (Kondaiah et al., 2008; Weir and Fisher, 1972). MeWalter in 1907 reported that, boric acid which was used in medicine for infants, has a notable poisoning effect (Goldbloom and Goldbloom, 1953). Boric acid concentration, 1000 to 2000 ppm boron equivalents, can induce testicular atrophy in animals such as dogs and rats (Ku et al., 1993). Human beings may be exposed to boric acid through drinking water, foodstuffs and inhalation during mining and industrial processing (Moore and Committee, 1997). Boric acid poisoning includes vomiting, nausea, acute kidney failure and neurotoxicity (Restuccio et al., 1992). A recent study reports that excess boric acid might also be toxic to the reproductive system of both genders (Fort et al., 2016).

As excess of boric acid cause several problems to human beings and animals, it has to be recovered properly. The removal of boric acid from aqueous solution is complicated, since conventional physical and biological treatment methods cannot decrease the level of boric acid in a solution significantly (Şahin, 2002). Proven effective methods to remove boric acid are stated to be adsorption and membrane

based technologies such as reverse osmosis (Dydo and Turek, 2013; Wolska and Bryjak, 2013). These methods are suitable for low boron concentration in a solution (Guan et al., 2016). At higher boron concentrations, alternative methods have to be considered. Besides, in the boron mining and processing plants, boron containing aqueous waste streams are generated. They are mainly stored in large ponds. Discarding these wastes in the ponds, have both environmental and economic significance. As an alternative to storage, in this study, recovery of boric acid from the synthetic waste pond aqueous concentration is investigated via Eutectic Freeze Crystallization (EFC). The knowledge gained on EFC is compared to conventional evaporation method.

2.1.5 Eutectic Freeze Crystallization

2.1.5.1 Definition and separation principle

In process industry common conventional methods to separate highly soluble salts from their concentrated aqueous solution are either cooling or evaporation crystallization. In the evaporation method, energy consumption is high and frequently not economical. Due to the residual solubility at a low temperature, the cooling crystallization is not a highly-efficient process (Zijlema et al., 2000; van der Ham et al., 1998). Eutectic Freeze Crystallization (EFC), which is a novel technology, is a good candidate at this stage. EFC process, operates around eutectic point, crystallizes ice and salt simultaneously and separates these solids by their density differences (Randall et al., 2011). The solubility for a binary phase diagram for a eutectic system is shown in Figure 2.2. The temperature and the concentration of a solid which is in equilibrium with the solution can be determined by the solubility lines. The intersection of ice and salt solubility lines is called eutectic point (point C) (Genceli et al. 2005).

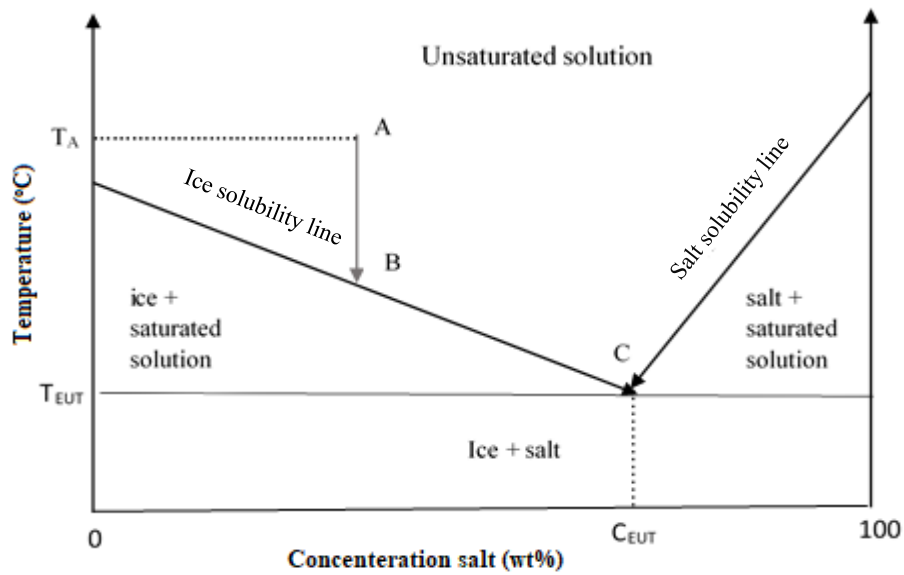


Figure 2.2: General phase diagram for a binary aqueous solution.

When a solution having a temperature and concentration value at point A is cooled until point B (located on the ice solubility line), ice starts to be formed. Upon further cooling, while solution temperature decreases, its concentration increases towards point C. Point C is the eutectic point (EP) and over there ice and salt crystallize at the same time. The temperature and concentration of solution at EP are called eutectic temperature (T_{EUT}) and eutectic concentration (C_{EUT}). Having a starting solution with a higher concentration than the eutectic point would set in motion the salt formation first followed by the ice crystallization (van der Ham et al. 1999).

2.1.5.2 EFC process and its advantages

EFC process flow scheme in terms of basic units are introduced in Figure 2.3. Feed solution is sent to the crystallizer where it is treated around eutectic conditions, i.e. ice and salt are crystallized simultaneously within the crystallizer. Due to prevention of scaling, the stirrer of the crystallizer is operated fast which prevents ice and salt to separate efficiently. Thus, following crystallizer ice and salt slurry outlets are sent to a separator column where they are separated due to their density difference. Ice slurry is collected from the top of the separator and then sent to the wash column. Sucking the mother liquid in the wash column would yield pure ice, i.e. pure water production. Mother liquid in eutectic composition sucked from the wash column is sent back to the crystallizer.

The salt slurry collected from the bottom of the separator is sent to filtration unit where pure salt is separated from its mother liquid. The filtered mother liquid at eutectic concentration is also recycled back into the crystallizer. Theoretically, the efficiency of the EFC process in the production of pure ice and solid salt is 100%, which is one of the attractive advantages of this system (Williams et al. 2015).

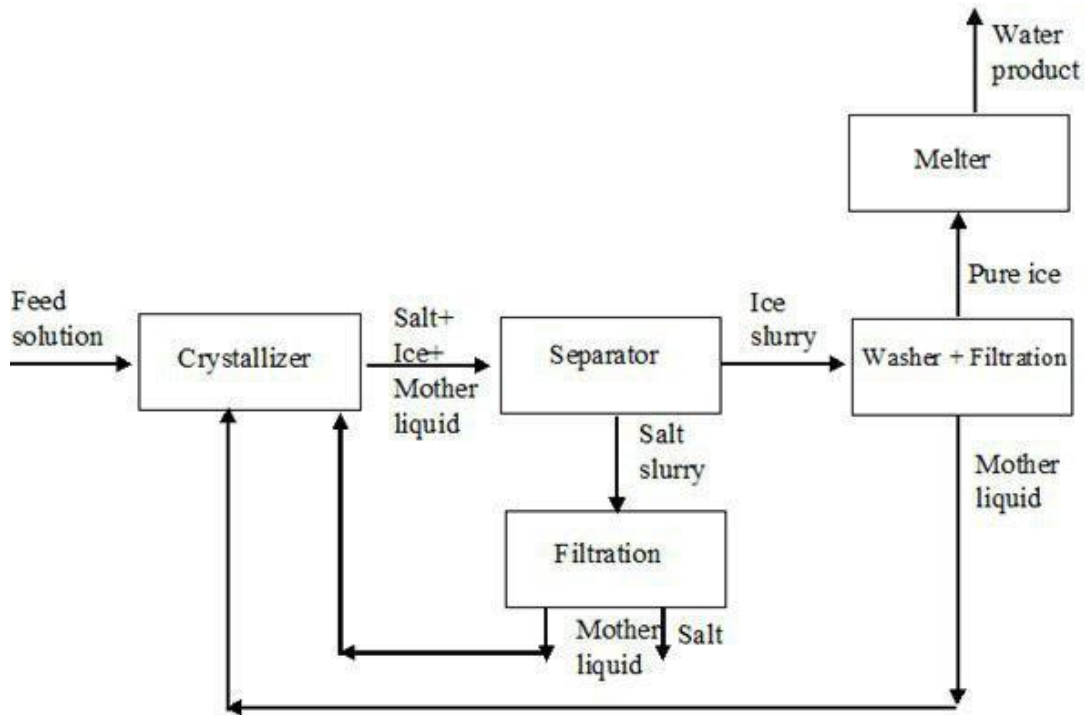


Figure 2.3: Schematic representation of EFC process.

In addition to the high efficiency of the EFC process, one can list the other advantages of this process as follows:

- Energy consumption in EFC process is less than the evaporation since the heat of evaporation is six times higher than the heat of fusion (Randall et al. 2011).
- In EFC process, the low operating temperature decreases the corrosion potential. Thus, cheaper construction materials can be used (Randall et al. 2011).
- Due to no further chemical compounds are added to the system, EFC process is not so complicated, cheap and environmentally friendly (Lorain et al. 2001).

The economic aspect of EFC process is highly dependent on the composition of the solution. As stated above, the energy consumption of EFC process is stated to be low due to the cheaper operating cost in comparison with the evaporative crystallization. However, the capital cost of EFC process is calculated to be higher than the evaporative crystallization (Randall et al. 2011).

2.1.6 Evaporation

Evaporation is one of the conventional physical methods to separate a liquid from a dissolved by applying energy (Rao et al. 2017). In the evaporation process, water is generally used as a solvent and the desired product is obtained from a concentrated solution. The evaporation process is used for diversity of material such as metals, alloys and elemental semiconductors (Griesser 2016).

The energy requirement to drive evaporation process is a significant amount which is named as the latent heat of evaporation (McCann and Bryson 2015). In this process, the solution is heated and consequently concentrated. Therefore, the supersaturation is created via evaporating water (the solvent). Finally, the supersaturated solution is kept at the room temperature to cool naturally and let the crystals to nucleate and grow.

The economic analysis of various separation methods reveals that although evaporation is the most common method to recover mineral, some other methods such as membrane separation are cheaper and more popular (Kim 2011).

2.2 Material And Methods

2.2.1 Material and methods for eutectic freeze crystallization

2.2.1.1 EFC material

The objective of this study was to determine eutectic point, growth kinetic and production rate of the boric acid-water system under Eutectic Freeze Crystallization. Thus, experiments were designed for 2.5 wt% boric acid (H_3BO_3) aqueous starting solution. The synthetic solution was prepared using more than 99.5% boric acid (Merck, impurity content given in Table 2.1) and deionized water. Deionized water had a conductivity of 0.067 $\mu s/cm$.

Table 2.1: Specifications of the maximum impurity concentration of Boric Acid

Impurity	% Composition
Undissolved compound	0.003
Ammonium (NH ₄)	0.001
Carbonate (CO ₃)	0.05
Chlorine (Cl)	0.0005
Phosphate (PO ₄)	0.001
Sulphate (SO ₄)	0.0025
Arsenic (As)	0.0002
Calcium (Ca)	0.005
Heavy Metals (Pb)	0.002
Magnesium (Mg)	0.002
Iron (Fe)	0.0005

In this study, ethylene glycol was used as an indirect coolant.

2.2.1.2 EFC Experimental setup

Experiments were carried out in a 1-liter plastic beaker used as a crystallizer. The crystallizer was placed in a double walled glass vessel and indirectly cooled via ethylene glycol solution between the crystallizer and the double walled vessel. Ethylene glycol as a coolant was circulated via Julabo circulator FP40 cooling machine with a 2.3 kW capacity at a range of -40 °C and 200 °C. Temperature data was measured with two sensors (T₁ and T₂) and recorded in a 10 seconds interval with an Agilent multimeter (model LXI 349772A) connected to Temp-Control thermistors (model NTC-8315). The thermistors had an accuracy of ±0.01 °C and resistances at 0 °C as 32.7 kΩ (Genceli et al., 2015). The first sensor (T₁) was immersed in the solution and the second one (T₂) was immersed in the coolant between the crystallizer and the double walled vessel. For following the temperature variations in the setup inline, also a PT100 temperature sensor having ±0.1°C accuracy was used whenever necessary. In the experiments, Ika Rw 20 agitator -working with 220 V, 50Hz- was used to stir the solution in a range of 60-2000 rpm. In Figure 2.4, the photos of crystallizer, cooling

machine and Agilent digital multimeter; and in Figure 2.5, the experimental set-up is presented. Stuart modal CD162 type magnetic heater was used to accelerate the dissolution of boric acid in deionized water. Examination of the crystals after reaching the eutectic point was done under Olympus BX51 microscope.

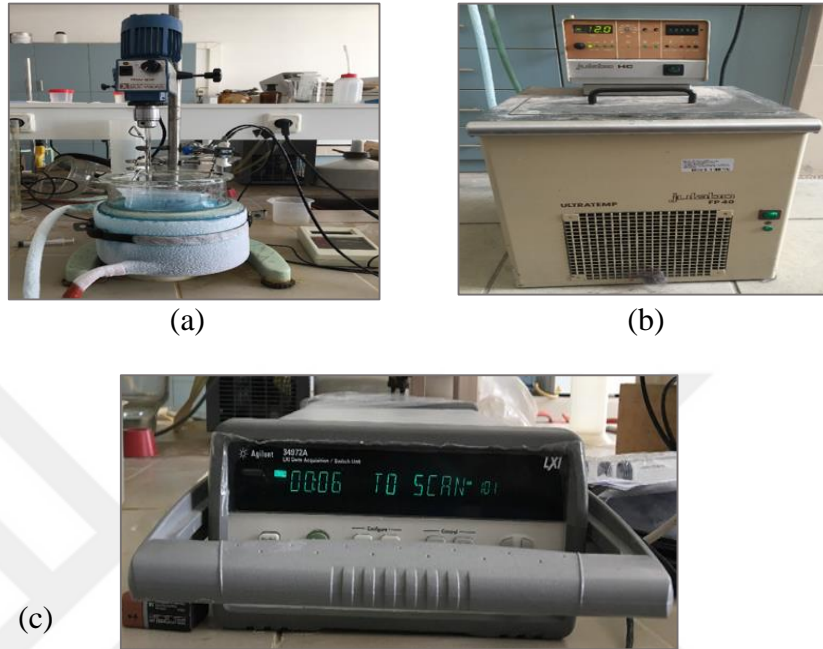


Figure 2.4: (a) Crystallizer; (b) Cooling machine; (c) Agilent digital multimeter photos.

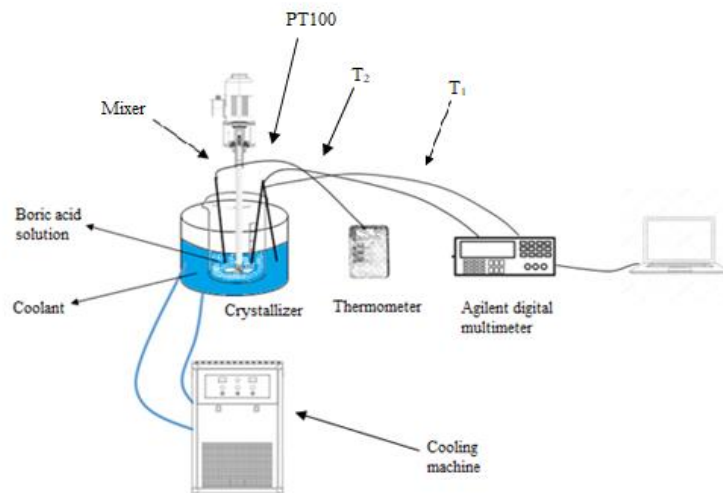


Figure 2.5: The experimental set-up of EFC process.

2.2.1.3 EFC Experimental Procedure

The synthetic boric acid solution was prepared by dissolving 25 g of boric acid in deionized water summing up 1000 grams in a 1-liter volumetric flask. In order to have a homogenous solution, the mixture was stirred with a magnetic mixer for 1 hour over a heater kept at 40 °C. Before starting the experiment, 10 ml sample was taken for detecting the boric acid concentration via titration. The solution was poured into the crystallizer in the experimental setup and Ika Rw 20 type mixer was set to 200 rpm stirring rate. The cooling machine was started with a temperature set point of -6 °C. According to the cooling machine's set temperature, the supersaturation of the solution which is the driving force of crystallization process was regulated. All through the experiments, the supersaturation was defined to be the temperature difference between solution (T_1) and ethylene glycol coolant (T_2) measured temperatures.

As solution temperature started to be cooled down, ice formation was mostly visualized first. This was followed by the temperature jump seen on the temperature profile. When the system reached eutectic point, salt and ice crystals were seen at the same time. The salt samples were then collected from the solution at around 15 minutes, 30 minutes, 45 minutes and 60 minutes after eutectic conditions were achieved. The salt crystals were observed under the camera with 5X magnification of the Olympus BX51 microscope. Experiments were repeated with the cooling machine set temperatures at -8 °C and -10 °C following the same procedure. At each different cooling machine set temperatures i.e. supersaturations, the growth rate of the crystals was then determined.

2.2.2 Material and methods for evaporation

In the second part of this study, the evaporation method was applied to determine the growth rate of a boric acid salt from aqueous solution. The energy consumption of this process was also carried out to compare to the one of EFC.

2.2.2.1 Evaporation material

Evaporation experiments were carried out with 2.5 wt% synthetic boric acid (H_3BO_3) aqueous solution. The aqueous solution was prepared by dissolving 2.5 g boric acid (H_3BO_3) of Merck Company and by taking 25g of boric acid in a 1-liter volumetric

flask and adding deionized water and until 1000 grams. The impurity content of boric acid and water quality were the same as stated in section 2.2.1.1.

2.2.2.2 Evaporation experimental setup

In the evaporation experiments, a magnetic heater-mixer (Stuart brand CD162), a rotary evaporator (Heidolph brand), a titrator (Schott Titronic Universal), and a vacuum filter devices (ILMVAC) were used.

The evaporation experiments were done in a rotary evaporator. In the evaporator, the solution was placed in a 500 ml rotator flask. The temperature of solution was increased indirectly via hot water placed in a heating bath. The heating bath temperature and rotation speed were controlled via two distinct knobs. Both knobs were illuminated by the two switches in front. Using water, the temperature of heating bath was ranged between 20 to 100 °C. The flask rotation speed was adjusted between 10 to 280 rpm. In the system, there was a condenser with a coolant (generally cold water) to condensate evaporated feed. At the bottom of the condenser, there was a collecting flask to catch the condensed product. In the evaporator, the evaporation flask was moved up/down in the heating bath by immersing lift which performs manually. Moreover, the pressure of system was adjusted using a vacuum system which could decrease pressure of the system up to 0.1 bar (Radleys company, 2018). In Figure 2.6, the scheme of evaporation experiments setup is shown.



Figure 2.6: The evaporation experiment setup.

2.2.2.3 Evaporation experimental procedure

Approximately 500 ml of the prepared 2.5 wt% boric acid aqueous solution was taken up in the rotary evaporator. In this unit, the temperature, the rotational speed and the vacuum were set to 45°C, 60 rpm and 1atm, respectively. A constant flow of cold water was provided to the evaporator for the condenser section. Evaporation process began with increasing temperature of the solution. Evaporated part of the solution, condensed via cold water flow, was assembled in the container section of the evaporator as a liquid.

The rotary evaporator was operated until the water was vaporized from the solution and collected in a container approximately 300 g. After evaporation, the resulting concentrated boric acid solution was allowed to cool down to room temperature naturally. In some experiments, when the cooled solutions reached about room temperature, the seed crystals were added. After about 3-4 hours, the size distributions of the crystals were measured to determine approximate crystal growth rate.

2.2.3 Concentration measurement

Solubility diagram of a system is a function of temperature and concentration. One of the conventional methods to measure the concentration of the solution at a particular temperature is direct titration. In this study, boric acid titration experiments were carried out by an automatic titrator (Schott Titronic Universal) as shown in Figure 2.7. In Appendix 1, the titration procedure is presented in detail.



Figure 2.7: Automatic titrator (Schott Titronic Universal).

2.2.4 Measurement of crystal size

In order to measure the crystal dimensions, crystals samples were obtained from the crystallizer and placed on a microscope slide. Olympus BX51 optical microscope with 5X lens was used to magnify on to the salt crystals. Photos of salt crystals were taken using a camera connected to the microscope and recorded to a computer via Image-Pro Plus software (Figure 2.8). Image J program was then employed to process the photos. Image J is an expansible tool to analyze the images on any platforms (Collins, 2007; Abràmoff et al., 2004). For each waiting period, from the photographs taken under the microscope, approximately 400 crystals were randomly selected. For the characterization of the crystals, according to Classical Nucleation Theory (CNT) assumption, crystal particles nucleate spherical. We also assume that they further grew in spherical shape. Thus, in 2D images, crystal particles were determined as a circle and the characteristic radius was calculated accordingly (Karthika et al., 2016).

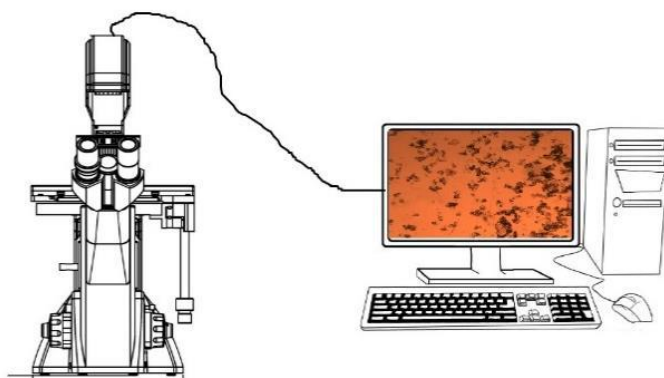


Figure 2.8: Crystal imaging via microscope set-up

2.2.5 Single crystal XRD measurement

X-Ray Diffraction (XRD) provides main information on the molecular structure of solids such as bond distances and bond angles (Andrei S.Batsanov, 1999). In this study, molecular structures of boric acid crystals synthesized under EFC and evaporation methods were compared via single crystal-XRD measurement (Figure 2.9).

The boric acid crystal structure was screened by Bruker D8 VENTURE diffractometer. The diffractometer is on the axis of rotation $1.0^\circ\Phi$ and established with Bruker Kryoflox II cooling system at 100 K which contains graphite monochromated Mo-K α radiation ($\lambda = 0.71073 \text{ \AA}$) (Dolomanov et al., 2009).

The crystal structure was determined by the method of SHELXS-97 and confirmed by SHELXL-2014/7 (Sheldrick, 1997; Sheldrick, 2008). Moreover, the molecules were drawn by version 1.2 of OLEX2 (Dolomanov et al., 2009). Further information on single crystal and instrumental parameters, data collection and calculations is shown in the supporting information file.

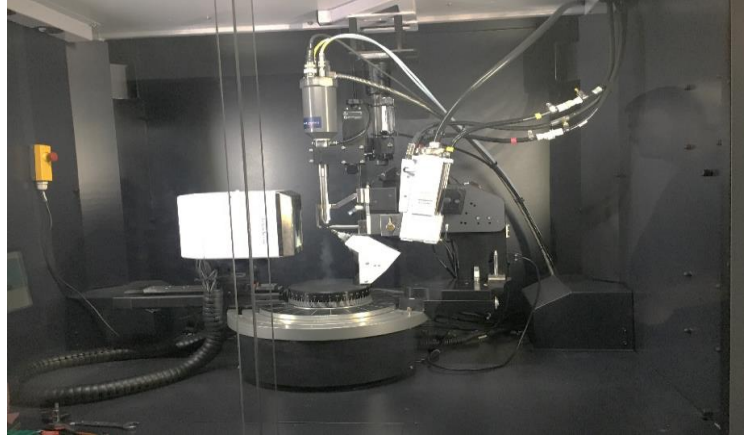


Figure 2.9: Bruker D8 VENTURE Crystal XRD photo.

2.2.6 Production rate

In EFC process, the amounts of produced ice and salt over the residence time is defined as production rate. After crystallization of ice and salt crystals, the slurry was divided into two solids (ice and salt) and a liquid system.

In this investigation, the solid particles were separated from the mother liquor via vacuum filtration (ILMVAC brand) over a glass filter. In the filtration process, a vacuum pump was hired to make a low pressure for passing the liquid part of the slurry through the pores of the filter. By crossing the liquid part, the solid particles were separated from the slurry and stayed at the top of the filter. Since separated ice and salt were together, the total mass of bulk could be determined by weighting. In Figure 2.10, the photo of vacuum filtration to separate solid particles from the solution is shown.

By determining concentration via titration and measuring filtered ice and salt, it is possible to detect the ice and salt production rates. Despite the boric acid crystals, the ice particles are not stable at ambient temperature and are melted. Thus, ice crystals have to be handled in a cold room that is set at sub-zero centigrade temperatures.



Figure 2.10: The vacuum filtration photo.

2.3 Results and Discussion

2.3.1 Eutectic point determination

In EFC system, the first step is to determine the solubility diagram and the eutectic point. Boric acid is soluble in water and its solubility is highly dependent on temperature due to remarkable negative heat of solution (Stewart, 1985). In Figure 2.11, the phase diagram of H_3BO_3 -water system is presented and this curve is plotted regards to Seidell's data (Seidell and Linke, 1965). Accordingly, eutectic temperature and concentration of the system are pointed out to be $-0.75\text{ }^\circ\text{C}$ and $2.5\text{ wt}\%\text{H}_3\text{BO}_3$. Blue and orange lines represent the boric acid equilibrium, and ice equilibrium lines respectively. The black spot on the figure represents the initial composition and temperature of the solution.

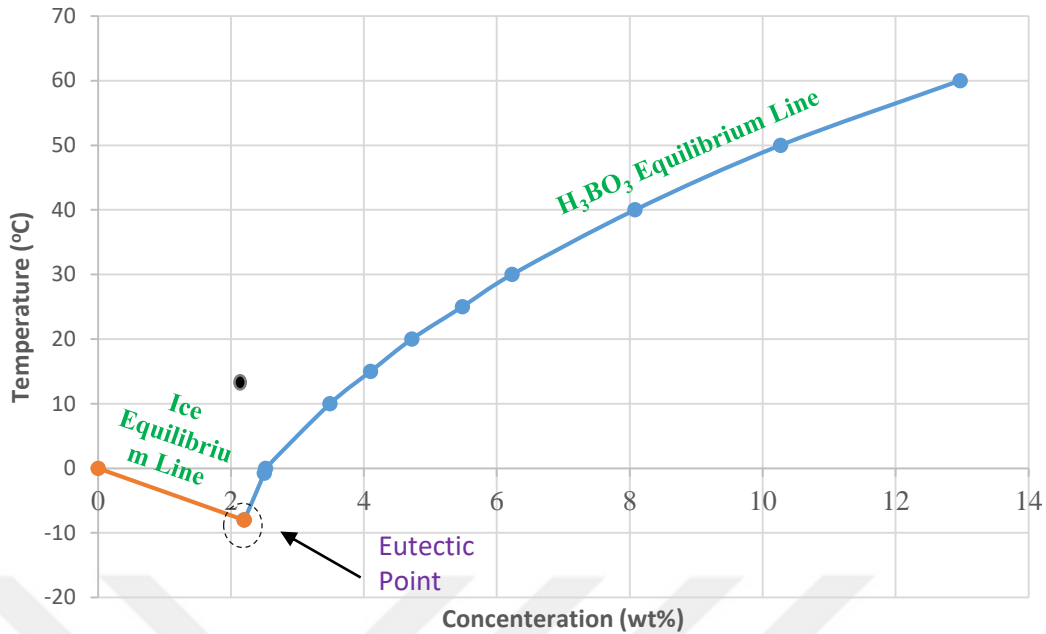


Figure 2.11: Concentration-Temperature diagram for boric acid.

When an experiment was started, the synthetic solution was placed into the crystallizer. As cooling machine was set to a lower temperature, the solution temperature decreased regards to coolant temperature value. A typical coolant temperature (blue line) and solution temperature (red line) vs. time profile is shown in Figure 2.12. Starting from room temperature, as solution temperature decreased and sufficient supersaturation was achieved, nucleation occurred. It was observed that ice always nucleated prior than salt. Ice nucleation was detected based on the temperature jump screened on the temperature profile in Figure 2.12. Release of heat due to ice crystallization was the cause of temperature jump. The salt nucleation moment could not be detected on the temperature graph as a temperature change. Yet, based on visual observation and temperature stability achievement was the proof of reaching the eutectic point. In this study, the eutectic temperature for boric acid was detected to be $-0.79\text{ }^{\circ}\text{C}$. As seen in Figure 2.12, after detecting a temperature jump in the solution, the temperature profile follows a plateau which shows that the system reached the eutectic point. In calculations, driving force for the nucleation and growth of ice and salt crystals is defined to be the difference between coolant and solution temperature. In Figure 2.12, the supersaturation is $7.24\text{ }^{\circ}\text{C}$ and the residence time is 800s. According to this figure, the nucleation occurred and the eutectic point was reached after 1200s.

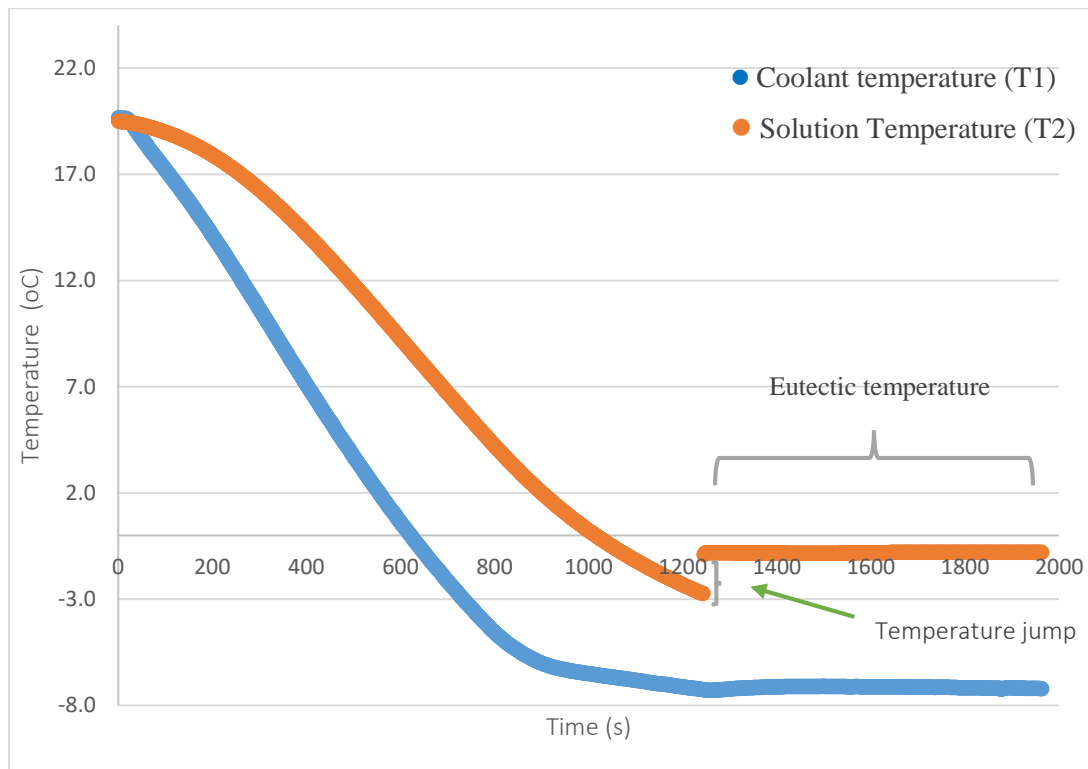


Figure 2.12: Temperature-Time diagram of boric acid.

2.3.2 Metastable zone width (MSZW) and nucleation rate

In crystallization, a supersaturated region in a phase diagram is defined as the area between saturated and labile zones (Christen and Hofmann, 1991). In the cooling crystallization, the difference between saturation temperature of a solution and the primary nucleation temperature is known as supersaturated zone width or metastable zone width (MSZW) (Kadam et al. 2012). MSZW indicates the nucleation kinetics of a system (Kubota 2008). MSZW is a function of several parameters such as rate of supersaturation generation, saturation temperature and impurity level (Barrett and Glennon 2002). In this study, the saturation (equilibrium) temperature of the solution is constant and impurity content of the solution is negligible. Therefore, MSZW can be considered as a function of the rate of supersaturation generation. In EFC process, the rate of supersaturation can be defined as the difference between the minimum temperature of the solution before nucleation and the eutectic temperature (Equation 2.1) (Kim and Mersmann 2001).

$$\Delta T_{max} = T_{EUT} - T_{min} \quad 2.1$$

In Equation 2.1, ΔT_{max} represents the rate of supersaturation generation, T_{EUT} the eutectic temperature and T_{min} the minimum temperature of the solution before

nucleation. The rate of supersaturation generation is corresponding with the maximum supersaturation (Equation 2.2) (Kim and Mersmann, 2001).

$$\Delta C_{max} = \Delta T_{max} \frac{dc}{dT} \quad 2.2$$

In Equation 2.2, ΔC_{max} and dc/dT express the maximum concentration supersaturation and temperature coefficient of solubility, respectively. The rate of supersaturation generation is directly proportional to the cooling rate of solution; i.e. the rate of supersaturation generation increases with increasing cooling rate (He et al., 2011). Thus, the cooling rate of solution also influences the MSZW. The relationship between concentration supersaturation and cooling rate is shown via (Barrett and Glennon 2002):

$$\frac{d\Delta c}{dt} = r \frac{dc}{dT} \quad 2.3$$

In Equation 2.3, r represents the cooling rate of the solution. Moreover, according to the classical nucleation theory, the nucleation rate of the crystal is a function supersaturation and can be expressed by:

$$B_n = k_o \Delta c^n \quad 2.4$$

In Equation 2.4, B_n represents nucleation rate, k_o nucleation rate constant and n nucleation order. If it is assumed that the nucleation rate is equal to the rate of supersaturation generation, for cooling crystallization, mass nucleation rate can be defined as (Lenka and Sarkar, 2014):

$$\frac{dM}{dt} = k_o k_v \rho r_n^3 \Delta c^n = k_n \Delta c^n \quad 2.5$$

Where dM/dt is the mass nucleation rate and $k_n = k_o k_v \rho r_n^3 \Delta c^n$ represent mass nucleation rate constant. Furthermore, k_v , ρ and r are volume shape factor, density of crystal and nuclei radius. Combining Equations 2.2 and 2.5 gives (Lenka and Sarkar 2014):

$$k_n (\Delta T_{max} \frac{dc}{dT})^n = r \frac{dc}{dT} \quad 2.6$$

the constant of nucleation rate, k_n and nucleation order, n can be derived from the log plot of cooling rate, r and MSWZ, ΔT_{max} (Mullin, 2001):

$$\ln(r) = n \ln(\Delta T_{max}) + \ln(k_n) + (n - 1) \ln(\frac{dc}{dT}) \quad 2.7$$

In equation 2.7, dc/dT is the slope of solubility diagram. This value can be obtained from the phase diagram of boric acid-water system as presented in Figure 2.11. In this log plot, the order of nucleation is obtained via slope of the and constant of nucleation rate from the intercept (Lenka and Sarkar, 2014).

In the context of this thesis, several experiments were performed by varying cooling rate where the system was allowed for primary nucleation. As stated before, MSZW was defined to be the maximum difference of the coolant and boric acid solution temperature as shown in Figure 2.12. Using all the collected data, MSZW versus the cooling rate of boric acid solution is drawn in Figure 2.13. In parallel with the literature work, it can be seen that MSWZ is directly proportional to the cooling rate of the solution. Increasing cooling rate increases the MSZW (Shiau and Lu 2014; Omar and Ulrich 2006; Camacho Corzo et al. 2014).

As mentioned above, since nucleation kinetics of the system can be considered by MSZW, higher cooling rate increases the nucleation kinetics of the solution. the calculation spread sheet of Figure 2.13 is presented in Appendix 2.

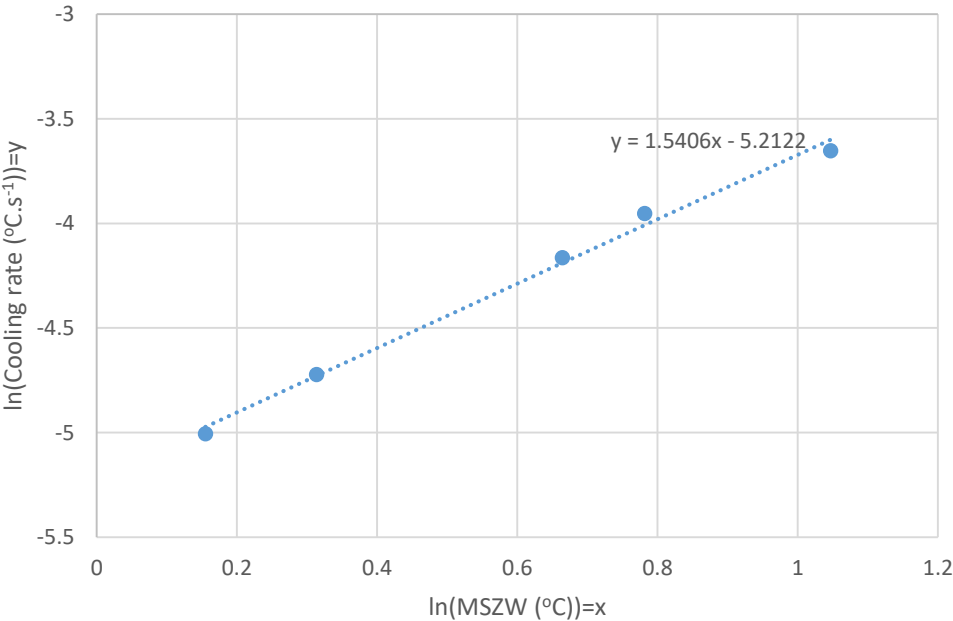


Figure 2.13: Metastable zone width versus the cooling rate of boric acid solution.

Using Figure 2.13 and Equation 2.2, nucleation order (m) and nucleation rate (k_n) of boric acid under eutectic conditions can be calculated. According to Figure 2.13, the other parameters of nucleation are presented in Table 2.2.

Table 2.2: The amounts of MSZW related parameters for boric acid-water system crystallizing under eutectic conditions.

dc/dT g solute (100 g solvent K) ⁻¹	n	k_n
6.11	1.54	2.01×10^{-4}

According to the value of Table 2.2, the nucleation rate of the boric acid can be calculated. Combining Equation 2.5 and 2.6:

$$\frac{dM}{dt} = k_n (\Delta T_{max} \frac{dc}{dT})^n \quad 2.8$$

According to Equation 2.8, the mass nucleation rate dM/dt can be determined as a function of metastable zone width ΔT_{max} .

2.3.3 Salt crystal size and growth kinetics

The most important factor to control crystal shape and growth kinetic is supersaturation. Thus, the modification of crystal shape and size is possible by controlling the supersaturation (Yang et al. 2006). In this study, ice and salt crystals grew around 1 hour, under eutectic conditions. The crystallization process was followed by sampling and taking pictures of the crystals under the Olympus BX51 optical microscope (Figure 2.14). In all pictures, the boric acid crystals typically have are circular (roundish)-rectangular shape. The ice crystals are roughly circular shape. The shape of ice and salt crystals are well agreed with the previous studies (Mullin 2001).

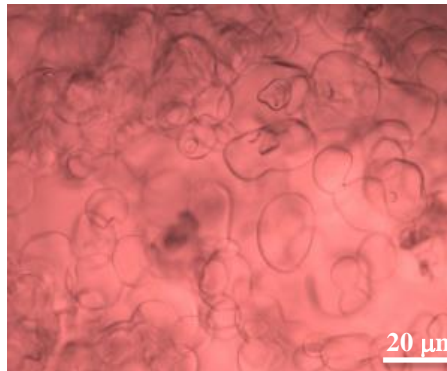


Figure 2.14: Typical pictures of boric acid crystals (left) and ice crystals (right) under EFC operation.

Crystal growth kinetic is a low order supersaturation function which can be characterized by a linear relationship (Civan 2007). The crystal growth is divided into

two mass transfer process: diffusion of salt atoms to the surface of nuclei and assimilation of atoms and nuclei (N.Ye et al. 2017). The rate of crystal growth depends on the ability of a solution to connect the atoms to the surface of the crystal and the ability of the crystal to absorb these atoms (Gilmer and Bennema 1972).

In previous studies, under evaporation, the growth rate of boric acid crystal was determined experimentally and modeled by concentration change as a function of supersaturation. Supersaturation in Şahin et al.'s study is defined as the change of dissolved solute amount. (Şahin et al. 2000). In this thesis, under eutectic freeze crystallization, the growth rate of boric acid is detected as a function of varying supersaturations. Due to the cooling crystallization behavior of EFC, everywhere in this study the supersaturation is defined as the difference between solution temperature and coolant temperature.

The overall growth rate, R_G is a function of the temperature driving force, ΔT and overall mass transfer coefficient, K_G as stated by Mullin (Mullin 2001):

$$R_G = K_G(\Delta T)^r \quad 2.9$$

In equation 2.9, r is an exponent of supersaturation which is changed between 1.5 and 2.5 (Mullin, 2001). Moreover, the overall mass growth rate can be related to the linear growth rate, G (Nývlt 1984):

$$R_G = 3\alpha\rho_c G/\beta \quad 2.10$$

In equation 2.10, α represents volume shape factor, β surface shape factor and ρ_c crystal density. Assuming that the boric acid crystals to be spherical, α/β is determined to be 1/6. Furthermore, the overall linear growth rate can be calculated by varying particle size ΔL with residence time t (Mullin 1976):

$$G = \Delta L/t \quad 2.11$$

In Table 2.3, boric acid salt crystal characteristic radius r , linear growth rates and mass growth rates are shown with various batch residence times and supersaturation. Varying batch times are defined as the residence time of the crystals in the crystallizer after the eutectic point was reached. The salt crystal photos taken under the microscope were used to calculate the characteristic diameter for each ΔT (supersaturation) by the Image J program. In EFC process, the cooling machine which is applied to cool the coolant, is set at different temperature. In Table 2.3, the coolant set points for the

experiments of this study is presented. Details of those calculations are presented in Appendix3.

Table 2.3: Crystal size measurement and calculation results

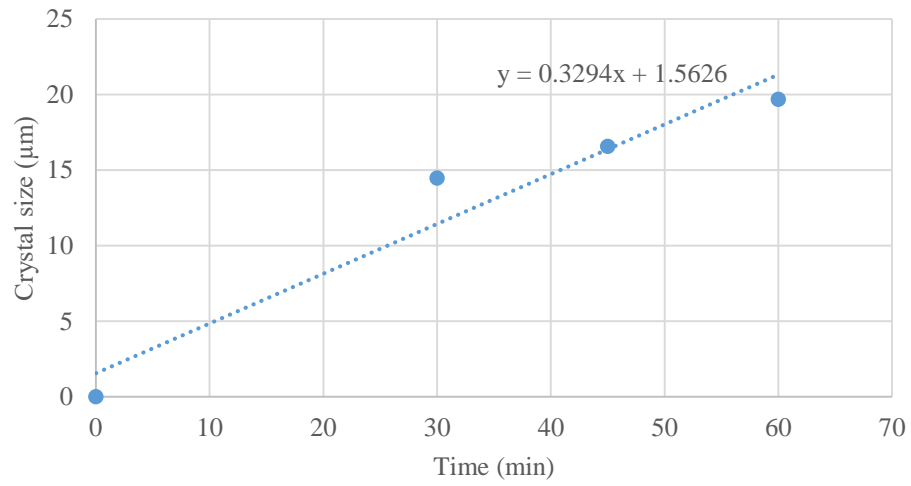
ΔT [°C]	Coolant set point [°C]	Batch Residence Time (min)	r_{charct} (μm)	Growth Rate (G) ($\mu\text{m}/\text{min}$)	Mass Growth Rate (RG) ($\text{kg}/\text{m}^2\text{s}$) \times 10^6
3.6	-6	0	0	0.005483	3.948
		30	14.48		
		45	16.57		
		60	19.67		
4.3	-8	0	0	0.006465	4.6548
		15	9.64		
		60	22.31		
6.5	-10	0	0	0.0098	7.056
		15	10.21		
		30	19.45		
		45	24.77		

Assumptions made during the calculations are listed below;

- Supersaturation (ΔT) = $T_{\text{eutectic inside the crystallizer}} - T_{\text{coolant in between crystallizer and double walled vessel}}$
- Nucleation is neglected.
- Crystal agglomeration and fracture are neglected.
- Growth rate is independent of crystal size.
- Homogenous mixing was carried out in the crystallizer.
- The system is batch. The results are evaluated by assuming a continuous system.

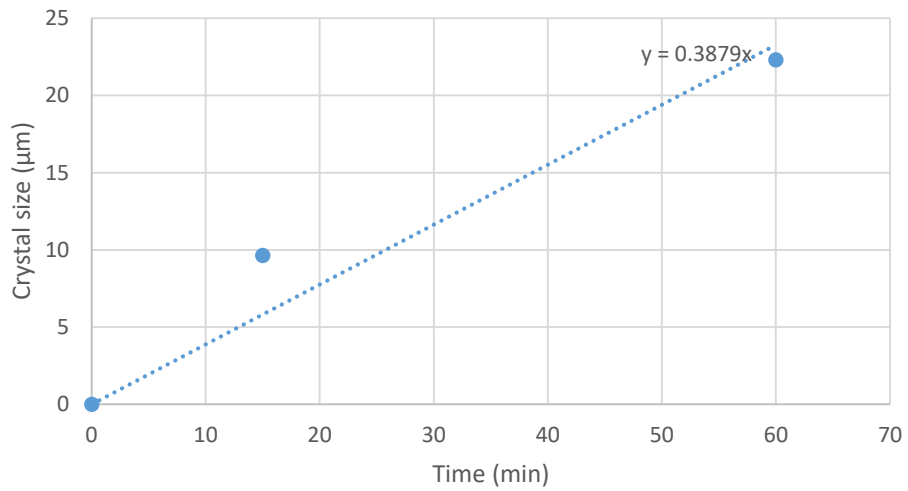
The growth rate of salt crystals was found by putting the characteristic radius (r_{charct}) vs. batch residence time from Table 2.3, linearizing and using the graphic slope of Figures 2.15 (a), (b) and (c) for each supersaturation.

Time- $r_{\text{character}}$ @ 3.6 °C

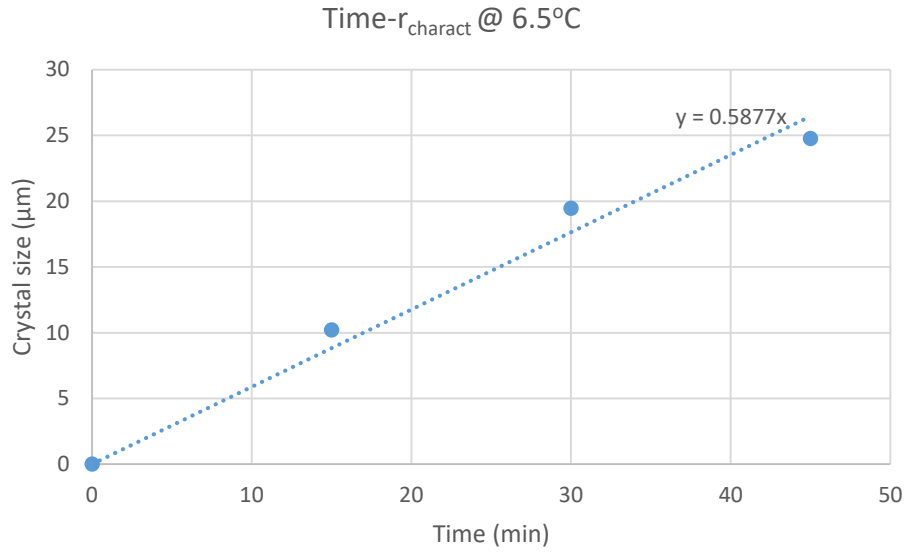


(a)

Time- $r_{\text{character}}$ @ 4.3 °C



(b)



(c)

Figure 2.15: Time vs. Crystal characteristic radius graph for (a) $\Delta T= 3.6$ °C, (b) $\Delta T= 4.3$ °C, (c) $\Delta T= 6.5$ °C.

In Figure 2.15 by linearizing the crystal size against residence time, growth rates ($\mu\text{m/s}$) were determined for various supersaturations. In our defined supersaturation ($\Delta T \approx 3\text{-}7$ °C) range, the growth rate of H_3BO_3 crystals was found to be around 7.5×10^{-9} m/s.

In Figure 2.16, the determined growth rates of boric acid crystals were then presented as a function of supersaturations. According to this figure, it can be seen that supersaturation has a significant effect on growth rate. Therefore, with increasing supersaturation, the growth rate of crystals is increased.

According to Figure 2.16, the growth rate constant for linear growth rate can be calculated via power law. The amounts of k_G and r which represents linear growth rate constant and order of supersaturation, are determined as $1.2 \times 10^{-10} \text{ m}\cdot\text{s}^{-1}\text{K}^{-1}$ and 1.0042. Based on the order of supersaturation, it can be concluded that the linear growth rate is directly related to the supersaturation.

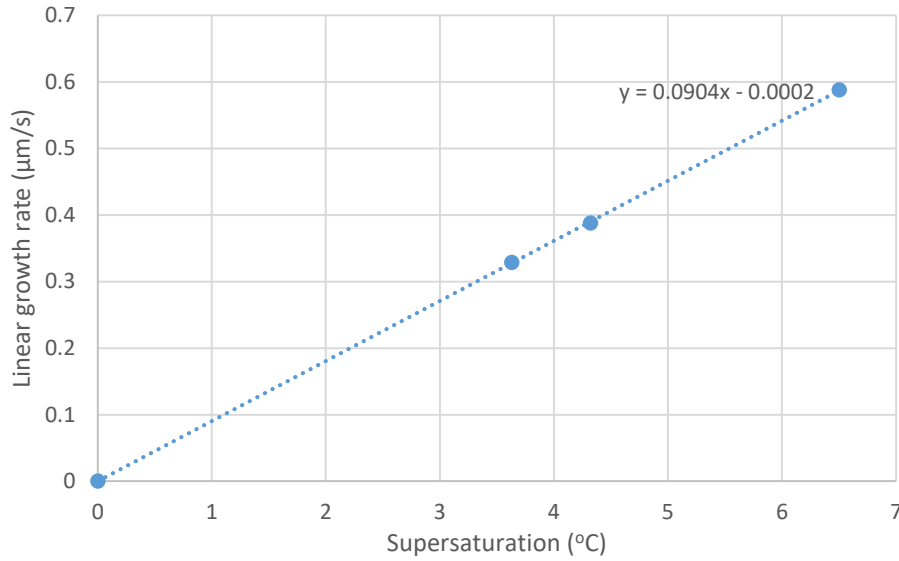


Figure 2.16: Growth rate of boric acid versus the supersaturation under eutectic operation conditions

The mass growth rate can be calculated as a function of the linear growth rate by Equation 2.4. According to Table 2.3, at the supersaturation range between 3 and 7 °C which is defined as difference of solution temperature and coolant temperature,, the mass growth rate is by approximately 5×10^{-6} kg/m²s. According to Equation 2.3, by drawing the mass growth rate versus the supersaturation , K_G and r constants can be determined by power law (Figure 2.17). Due to the power law, the amounts of K_G and r are calculated as 8.97×10^{-8} kg.m⁻².s⁻¹ and 1.0042, respectively. In the previous study on the growth rate of boric acid, the order of supersaturation versus the mass growth rate was ranged between 1.5-2.5 (Şahin et al., 2000). However, in this study, the order of supersaturation is almost 1 and growth rate is changed as a function of supersaturation linearly. Thus, the growth rate of boric acid is found out to be controlled not by surface reaction but only by mass transport, similar to ice growth rate case as reported by Genceli (Genceli, 2008).

During the crystallization process, in addition to the salt nucleation, ice crystals are produced. However, the experiments in this study were carried out at ambient temperature and the characterization of ice crystals were not possible. Since the melting point of ice is 0°C and to consider properties of ice crystals, an environment with a temperature lower than ice melting point is needed.

The calculated parameter can play remarkable role in determining growth rate boric acid crystallization in EFC system. Since the growth rate which predicts the particles size in different residence time, it is an important factor to consider efficiency of EFC process for boric acid and water system.

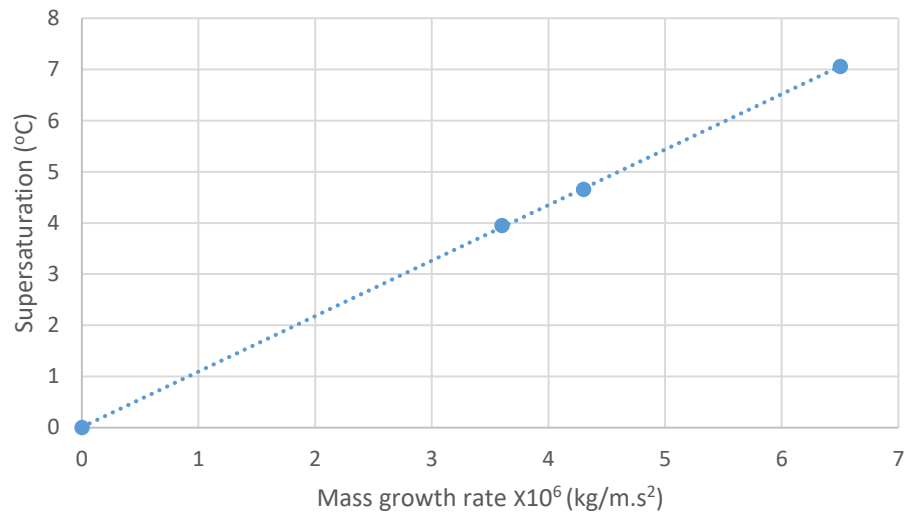


Figure 2.17: Mass growth rate of boric acid versus the supersaturation under eutectic operation conditions.

2.3.4 Production rate

In recent years, one of the main efforts of researchers and engineers in universities and industrial research centers is transforming traditional methods to novel technologies in the industry (Stankiewicz and Moulijn, 2000). Applying new technologies in the industry requires feasibility consideration of the technology to produce hundreds of tons of product per year (Tonkovich et al., 2005).

Production rate is the value of the produced mass of crystals over a specific time period (Ward et al. 2006). Therefore, the production rate determined by the kinetic of the system is an important factor to determine the capability of a process. In this section, the determination of production rate of salt and ice for EFC process via mass balance is presented. Despite the previous section in which ice crystals' growth rate could not be detected, in this section the production rate of ice crystals are calculated via mass balance.

As mentioned above, although the system is batch, we assume system to be continuous since sampling was made in the first 1 hour of the experiment (see Table 2.3). One of the main factor to consider production rate in the continuous process is residence time.

In this section, the residence time for boric acid and ice production rate calculation is assumed to be 1 hour.

The first step to determine the production rate is a mass balance which is defined as follows (Gros et al. 2001):

$$\dot{m}_{sol} = \dot{m}_{res} + \dot{m}_{salt} + \dot{m}_{ice} \quad 2.12$$

In equation 2.12, \dot{m}_{sol} , \dot{m}_{res} , \dot{m}_{salt} and \dot{m}_{ice} represent the mass flow rate of solution, mass flow of residual solution in the crystallizer, salt and ice production rates, respectively. In this study, since the actual system is batch, \dot{m}_{sol} can be considered the constant mass of the mother liquor. In Figure 2.18, the produced amounts of ice and salt versus time are shown. According to this figure, under eutectic freeze crystallization the production rate of salt and ice are calculated from the slope of the data to be 3.03 g.h⁻¹ and 99.16 g.h⁻¹, respectively. The production rate of ice is about 32 times larger than salt production rate. This production rate difference can be referred to as the initial concentration of each component. According to the eutectic point on the phase diagram presented in Figure 2.11, the initial concentration of water is larger than boric acid concentration approximately 39 times larger. However, in the experiment, the proportion of ice to ice is less than initial proportion. Since the experiment was carried out at the ambient temperature and a part of produced ice might be melted during the filtration process. Details of calculations are shown in Appendix A. 4.

In an actual continuous system, the feed flow is important factor to determine the residence time and consequently production rate. The feed flow rate is inversely proportional to the residence time. In other words, increasing the feed flow decreases the amount of formed solid content (Verbeek 2011). Due to feed is stable in this investigation, it is expected that production rate will be linear. In Figure 2.18, despite boric acid production rate that is almost linear, the production rate of ice is deviated. It can be concluded that the temperature of ambient affects crystal particles and melted them before weighting.

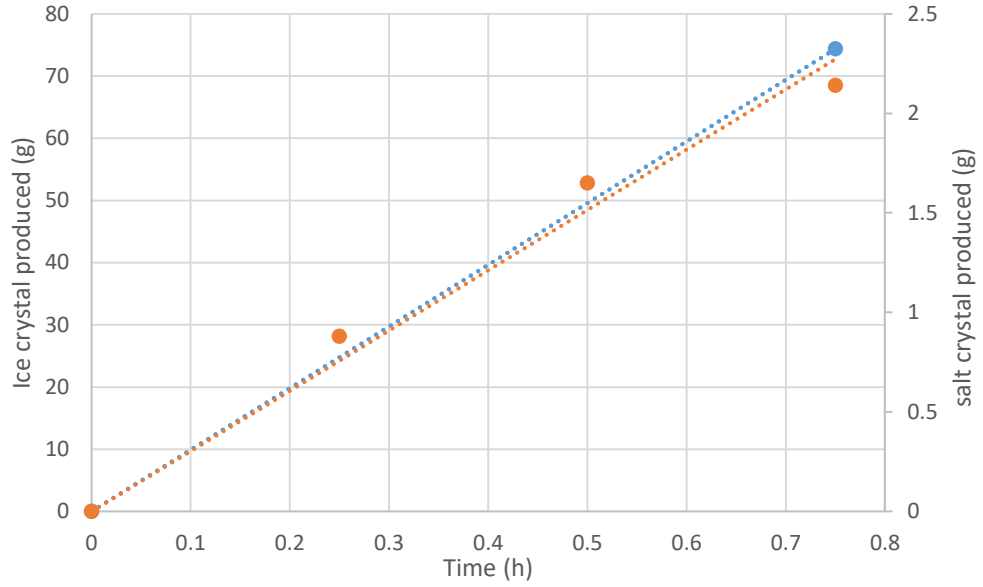


Figure 2.18: Produced amounts of salt (orange) and ice (blue) versus time.

Due to the small particle sizes of boric acid crystals measured (around 10 μm) under 1 hour of residence time, it was observed that boric acid salt crystals were captured within ice crystals. This was an obstacle for the efficient separation of eutectic freeze crystallizer and the separator design presented in Figure 2.3 and Figure 2.4. Due to the nature of EFC process, ice and salt crystals separate due to their density differences. Yet, in the sampling from the crystallizer it was recorded that boric acid crystals were easily captured in ice crystals. Thus, the settling velocity of boric acid was calculated for the system.

Crystals with a higher amount of settling velocities are mainly exposed by attrition and due to decrease of coefficient of variation, the size of maximum and medium crystals are reduced (Mersmann 1999). Stokes's law can be used to calculate the settling velocities of boric acid salt crystal particles in the solution medium.

$$V_{stokes} = \frac{D^2 \times g \times (\rho_k - \rho_s)}{18 \times \mu_s} \quad 2.13$$

Density (ρ_s) of boric acid-water system can be calculated via the following equation:

$$d_{\text{water}} = 0.997 \text{ g/cm}^3 \text{ and } d_{\text{boric acid}} = 1.435 \text{ g/cm}^3$$

$$\rho_s = (0.997 \times 0.975) + (1.435 \times 0.025) = 1.00795 \text{ g/cm}^3 = 1007.95 \text{ kg/m}^3$$

Table 2.4: Calculation of the settling velocities.

ΔT (°C)	D (μm)	D^2 (μm^2)	g (m/s^2)	ρ_k * (kg/m^3)	ρ_s ** (kg/m^3)	μ_s *** kg/(m·s)	V_{stokes} (mm/s)
6.5	50	2500	9.81	1440	1007.95	1.83×10^{-3}	0.32

* (Kim et al., 2019).

** (Şahin, 1999).

*** (Kestin et al., 1978).

According to the results in the previous part, the largest boric acid crystals size of produced salt is about 50 μm . As presented in Table 2.4, using Stokes equation, under eutectic conditions the settling velocity of boric acid crystal with $\approx 50 \mu\text{m}$ size is $3.2 \times 10^{-4} \text{ m/s}$. If it is assumed that the maximum distance for the largest crystal to move is 15.5 cm, based on the settling velocity, the minimum residence time should be 0.13 hour. One hour as residence time can be a suitable time for settling of boric acid crystals. Therefore, there is enough time for ice and salt crystals move upward and downward, respectively and are separated properly.

2.3.5 Crystal structures of boric acid salts around the eutectic point

In this section, to determine the crystal structure definitely, despite the previous section, 4 wt% boric acid concentration was prepared. Using the experimental setup presented in Section 2.2, a cooling profile was applied to the boric acid solution. In Figure 2.19, coolant (blue) and boric acid solution (orange) temperature profiles are given. According to the profile, boric acid crystal nucleation was detected around 7.5 °C. Up on further cooling, lead the crystals to grew larger and they were filtered from the solution just at the eutectic point -0.75 °C before ice crystals nucleated. Boric acid salts collected from the crystallizer were isolated and placed into dry ice. They were then transported to Chemistry Department of Istanbul Technical University for crystalline structure determination via single crystal XRD method as described in Section 2.2.

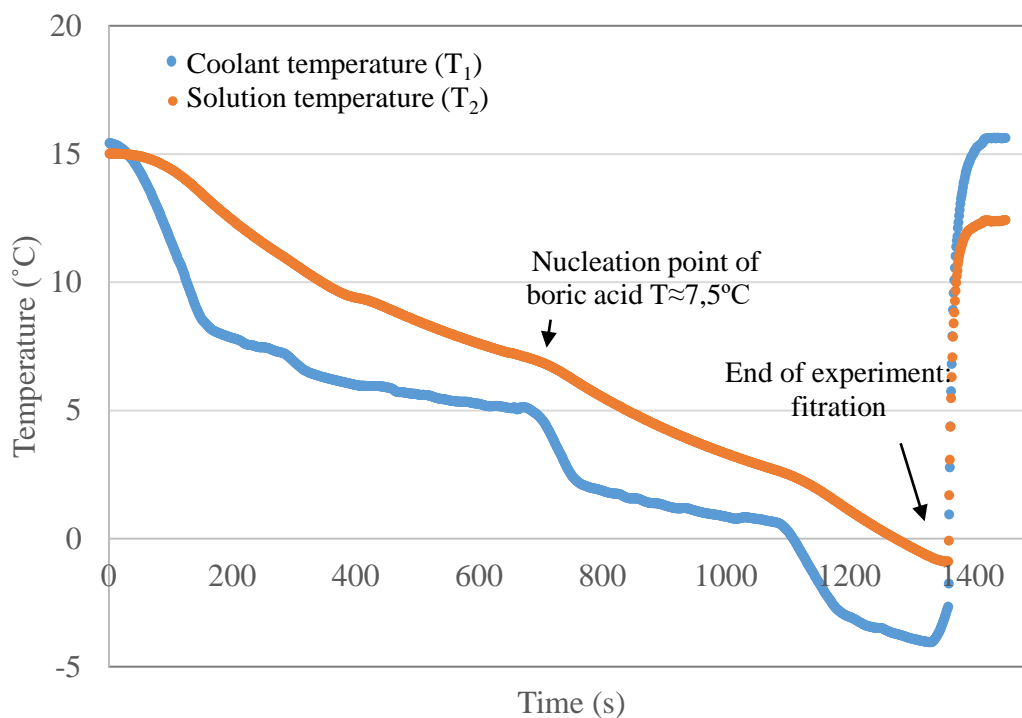


Figure 2.19: Temperature-Time Graph of Boric Acid Solution

A colorless, rod-shaped H_3BO_3 crystal of about $0.01 \text{ mm} \times 0.02 \text{ mm} \times 0.4 \text{ mm}$ appearing in Figure 2.20 was used for X-ray crystallographic analysis and X-ray density data were measured.



Figure 2.20: Photo of crystal used for structure determination in single crystal XRD measurement.

Totally, 1480 pose was taken and the total irradiation time was 3.29 hours. Pose is integrated by using the Bruker SAINT Software package with wide-pose algorithm. The following data are obtained about the crystal H_3BO_3 , triclinic, (space group) $P\bar{1}$, colorless block, unit cell $\underline{a} = 6.336(3) \text{ \AA}$, $\underline{b} = 6.997(3) \text{ \AA}$, $\underline{c} = 7.001(4) \text{ \AA}$, $\alpha = 119.933(12)^\circ$, $\beta = 90.919(15)^\circ$, $\gamma = 102.147(14)^\circ$, $V = 260.3(2) \text{ \AA}^3$, $Z = 4$, $D_{\text{calc}} = 1.578 \text{ g/cm}^3$. In Figures 2.21, 2.22 and 2.23, the crystal stacking, the intermolecular hydrogen bonds and the pictures of the main structure are presented respectively.

Comparing the H_3BO_3 crystal structure unit cells that have been described in previous studies, it is seen that, the unit cell of orthoboric acid (H_3BO_3) synthesized around the eutectic point at this study, is different from the literature (Shuvalov and Burns, 2003b; Zachariassen, 1954).

These crystals crystallized at the eutectic point and room temperature. Although the crystal stacking of the salts is the same, the unit cell bond lengths are different which may be due to differences in crystallization conditions between experiments.

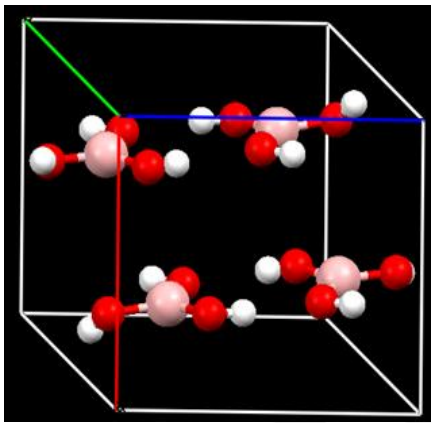


Figure 2.21: Crystal Stacking of H_3BO_3 .

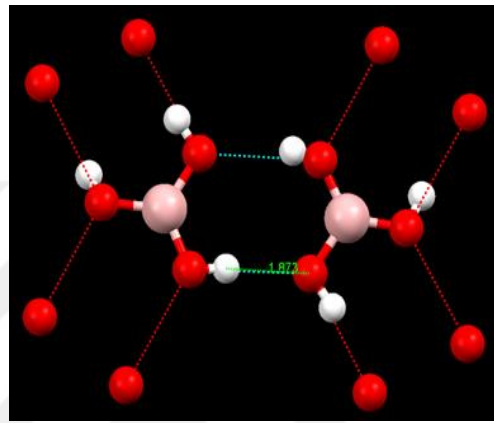


Figure 2.22: Intermolecular Hydrogen Bonds of H_3BO_3 .

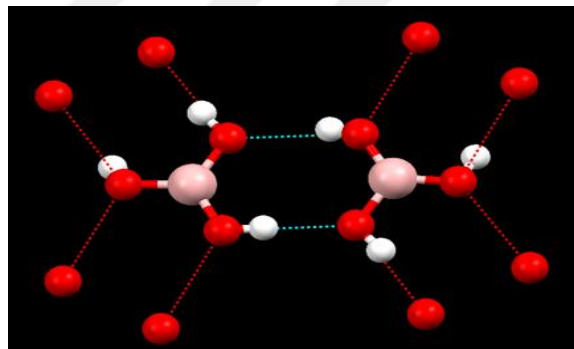


Figure 2.23: Main Structure Pictures of H_3BO_3 .

2.3.6 Crystallization of boric acid aqueous solution by evaporation

In this study, via evaporation method, the boric acid-water solution was concentrated. Then, due to natural cooling, the solution became saturated which led the boric crystals to be nucleated and grew until they reach room temperature. The experimental result of evaporation method was then compared to the ones of eutectic freeze crystallization method. In Table 2.5, the process conditions and result of the evaporation process for an evaporation experiment are presented. The concentration of boric acid in the solution was applied as EFC process 2.5%.

In the evaporation experiment, after vaporizing 342 g water from the solution at 45°C, the concentration of residual solution became 8.16 wt%. The residual solution was cooled naturally at the environment temperature which was 8 °C. The solution was cooled from 45 °C until 8 °C over 232 minutes. During the natural cooling of the solution, 8.4 g boric acid crystals were precipitated. After evaporation experiment, the concentration of solution was determined by titration that it was determined as 3.2 wt%. the validity of these data was examined by mass balance over this process. The calculated error for filtration and titration of this experiment was calculated 5% which is acceptable amount.

Table 2.5: The process conditions and results of the evaporation process.

	Title	Amount	Unit
Initial solution	Amount (Boric acid+ water)	493.02	g
	Amount of Boric acid	D 12.31	g
	Concentration	2.50	**wt %
Evaporation	Temperature	8	°C
	Pressure	1	atm
	Temperature	45	°C
	Speed of rotation	60	rpm
	Amount of evaporated water	342	g
	Amount of residual solution	A 151.02	g
	Amount of sample of initial solution	G 22.81	g
	Concentration of residual solution	8.16	**wt %
crys.*	Initial temperature of residual solution	45	°C
	Ambient temperature	8	°C
	After nucleation (without added crystals) crystallization duration	232	min
Filtration	Amount of precipitated and filtered salt crystals	B 8.4	g
	Amount of filtered solution	128.21	g
	Amount of NaOH for titration of the filtered solution	55.65	ml
	Concentration of filtered solution(calculated by titration)	C 3.2	**wt %
	Amount of salt crystals (calculated by mass balance)	7.73	g
	Error of crystalized salt amount (filtration and titration)	E 5	%

* cryst.: Crystallization

**wt%: Weight percent

$$*** E = 1 - \frac{(D-B) \times 100}{(A-B-G) \times C}$$

In Figure 2.24, the temperature and time graph of boric acid and water system for evaporation method is shown. The blue and orange plots represent the temperature of ambient and solution over time. The experiment was carried out in a cold room which was set at 8 °C. Therefore, the temperature of solution was constant at 8 °C.

The initial temperature of solution was 45 °C, however, it measured from 30 °C and cooled until 8.2 °C. According to the solubility diagram, the concentration of solution is at 8.2 °C must be 3.1 wt%. Based on titration result, the concentration is 3.3 wt% which is similar to the concentration of solution based on solubility diagram at 8.2 °C. According to Figure 2.24, the temperature of solution becomes constant and steady. Therefore, the solution was saturated and more crystals would not be precipitated until the temperature of the room and consequently, the temperature of solution was changed.

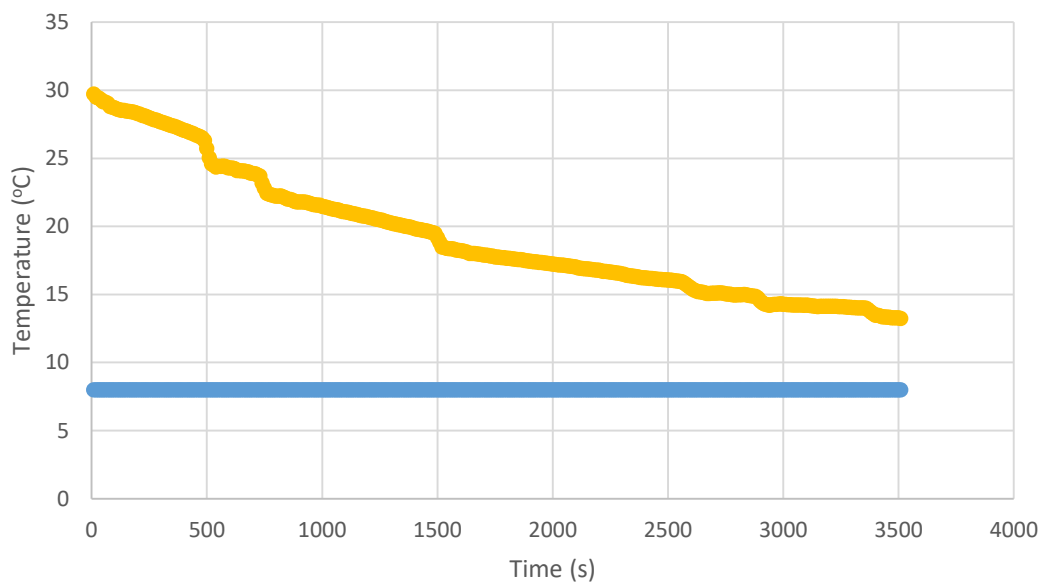


Figure 2.24: Temperature-Time Graph of Boric Acid Solution for evaporation method.

In terms of experimental evaluation, the crystal size in the evaporative crystallization was considered. After natural cooling, the crystal size distribution was measured before filtering boric acid salt. The dimensions of 1000 crystals from at least 30 microscope photographs (such as in Figure 2.25) were randomly selected and their surface area was calculated via Image J program as presented detailed in Section 2.2.4. As shown in Figure 2.25, boric acid salts usually had a hexagonal crystal shape. Totally, averages of around 1000 radii were taken and the average length of crystallized boric acid salts was calculated under experimental operating conditions. The average size of boric acid over 1 hour residence time is calculated 76 μm . The growth rate of crystals can be calculated by dividing the calculated particle size per residence time.

In this experiment, the supersaturation was defined as the logarithmic temperature difference between the temperature of the ambient and solution. Since the temperature of the solution is not constant was decreased from 30 °C to 13 °C over 1 hour. The logarithmic temperature difference is calculated via:

$$\Delta T_{LN} = \frac{(T_{in})-(T_{fin})}{\ln\left(\frac{T_{amb}-T_{in}}{T_{amb}-T_{fin}}\right)} \quad 2.14$$

In Equation 2.14, T_{in} , T_{fin} and T_{amb} represent solution initial, solution final and ambient temperature, respectively. According to this equation, the supersaturation of evaporation experiment is $\Delta T=11.47$ °C. Moreover the growth rate of the boric acid salt crystals was calculated to be 0.021 $\mu\text{m/s}$ under effect of the calculated supersaturation. The growth rate of boric acid crystals, by eutectic point crystallization and $\Delta T=11.47$ °C, was calculated to be 0.0003 $\mu\text{m/s}$. This shows that the growth rate of boric acid crystals, under EFC process is remarkably less than the growth rate of boric acid in the evaporation method. According to the results in Section 2.3.3 and literature, degree of supersaturation in evaporation method for large crystals is more than 2 (Şahin et al., 2000) and the growth rate of boric acid in this process is higher than EFC process. Therefore, the result of the evaporation experiment in this study is confirmed by literature.



Figure 2.25: Formed boric acid crystal by evaporation

2.3.7 Comparison of energy consumption between the evaporation and EFC process

As mentioned previously, EFC process consumes about seven times less energy than evaporation. In this section, two alternatives for recovering salt and water from 2.5 wt% boric acid waste solution content; evaporation and the eutectic freeze crystallization methods are compared energetically.

The energy required for the evaporation system is assumed to be the energy needed to heat the solution temperature to the operating temperature and evaporate the water to the desired amount.

In this context, the equation used for the under vacuum evaporation method is:

$$Q_{EvC.total} = (m_{solution} \times C_{p(solution)} \times \Delta T) + (m_{water} \times \Delta H_{water, evaporation})$$

By using the values given in Table 2.5, the specific heat of solution is calculated as follows :

$$C_{p(solution)} = (wt\%_{boric\ acid} \times C_{p(boric\ acid)}) + ((1 - wt\%_{boric\ acid}) \times C_{p(water)})$$

The energy required for the eutectic freeze crystallization system is assumed to be the energy needed to cool the solution temperature to the operating temperature and to form ice and salt crystals. In this context, the equation used for the eutectic freeze crystallization method is:

$$Q_{EFC.total} = (m_{solution} \times C_{p(solution)} \times \Delta T) + (m_{boric\ acid} \times \Delta H_{salt\ cryst. enthalpy}) + (m_{ice} \times \Delta H_{ice\ crist. enthalpy})$$

The energy requirement for salt crystallization of 2.5%wt boric acid solution was calculated on the basis of under vacuum evaporated crystallization and eutectic freeze crystallization method and results are presented in Table 2.5.

Table 2.5: Operating Conditions and Energy Requirements.

		EvC	EFC	Unit
Operating conditions	Initial temperature of the solution ¹	8	12	°C
	Operating pressure	1	1	atm
	Operating temperature	45	-0,7	°C
	Operating duration τ	3.87	1	hour
	Inlet temperature of coolant	-	-10	°C
	Outlet temperature of coolant	-	-9,5	°C

Energy calculations	m_{solution}	493	840	g
	$m_{\text{water}}^{++++}, m_{\text{ice}}^{+++}$	342	73	g
	$m_{\text{boric acid}}$	8.2	1,65	g
	$C_{p(\text{water})}$		4,187	kJ/kg.K
	$C_{p(\text{boric acid})}$		1,31*	kJ/kg.K
	$C_{p(\text{solution})}$		4,115	kJ/kg.K
	$\Delta H_{\text{water, evaporation enthalpy}}$		2283,2**	kJ/kg
	$\Delta H_{\text{ice, cryst. enthalpy}}$		359**	kJ/kg
	$\Delta H_{\text{ice, cryst. enthalpy}}$		333,55***	kJ/kg
	Energy requirement**/ $m_{\text{boric acid}}$	76	42	kJ/g

I. Accepted amount according to experiment data

II. For both systems, the heat loss is neglected.

* (Allison, 1998)

** (Perry and Green, 2008)

*** (Kim et al., 2019)

As seen, the processing with eutectic freeze crystallization method with an energy requirement of 42 kJ/g has more advantageous than vacuum evaporation with the requirement of 76kJ/g. In this study, although EFC process consumes three times less than the evaporation process, EFC process consumes much less energy than the evaporation method theoretically. This might be referred to as the formation of an ice layer on the bottom of the crystallizer. Since the ice layer decreases the thermal conductivity of the bottom of the crystallizer. Moreover, the formation of an ice layer increases the thickness of the surface area which has a negative effect on the overall heat transfer coefficient of process.

2.4 Conclusion

In this investigation, Eutectic Freeze Crystallization was applied for the recovery of water and boric acid salts from an aqueous synthetic boric acid solution. Eventually, this method is targeted to be used for boron waste streams. The growth rate, nucleation rate, production rate and molecular structure of boric acid salts on different supersaturations were investigated in order to increase the separation efficiency of boric acid crystals from ice crystals. Moreover, in the last part, an evaporation experiment was designed to be compared with the Eutectic Freeze Crystallization method for evaluating the performance of EFC process as a separation method.

As mentioned in the introduction section, the eutectic freeze crystallization process is an economical method to extract ice and salt from an aqueous solution. However, in this study, the other characters such as production rate were determined for having general evaluation of this method.

These experiments show that using eutectic freeze crystallization method for the recycle of boric acid-water system from boric acid solution wastes generated in the boron mines processes can potentially be used.

In EFC process, in addition to the salt crystallization, ice particles are crystallized. However, in order to consider EFC process for ice crystals, the experiment should be carried out in a cold room. Therefore, due to the experiment of this study were done at ambient temperature, the characterization of EFC process for ice was not possible. In the experiments, scraping the walls of the crystallizer and mixing the system was not sufficient enough to create a homogenous system. Different types of mixers can provide more efficient mixing.

Despite this investigation was accomplished in a laboratory scale batch system, it was assumed as a continuous system. Therefore, by scaling up this system, the results of this study can be useful for a large scale set up. However, in an industrial scale, the initial solution is a waste stream with the various compound. Therefore, the first step to apply EFC process for industrial streams is an accurate analysis of solution component and then design a proper process for it.

According to the result of this study, in EFC process, the relation between growth rate and supersaturation is linear. Since the order of supersaturation is almost 1. Also, the metastable zone width has a remarkable effect on the nucleation rate and is directly proportional to it. Moreover, the production rate of a component is highly dependent on initial concentration.

According to the result of this study, The EFC process in comparison with evaporation is energetically more favorable and with higher production rate. However, the growth rate of boric acid crystals in EFC process is significantly less than the crystal growth rate in the evaporation method.

3. MODELING OF HEAT TRANSFER IN EFC PROCESS FOR AQUEOUS SODIUM CHLORIDE SOLUTION

3.1 Introduction

3.1.1 Fundamentals of the melt crystallization process

One of the oldest unit operation in the chemical industries is the crystallization process. For instance, this process has been one of the conventional production methods of sodium chloride (NaCl) since the dawn of civilization. Nowadays, the crystallization process, which is the non-removable process of most of the chemical industry, can be used as a method of production, purification, and recovery of solid material. Although crystallization process has been known as one of the best and the cheapest method for the production of pure solids from an impure solution, it has more advantages of giving a product with many desirable properties (Mullin, 1993).

One of the most common crystallization methods in recent years is melt crystallization. Melt crystallization can be applied in the separation of organics, isomers, heat sensible material, etc. (Kim and Mersmann, 1997). The main advantages of melt crystallization are a less energy consumption and a very high efficiency in comparison with other separation methods (Gerard F.Arkenbout, 1997). There are two main kinds of melt crystallization method: One of these can be characterized by the production of a crystal layer on a cold surface which can be on the wall of the heat exchanger. The other type, the growth of crystals are in suspension. In latter process, there are two steps: the formation of a crystal in the crystallizer and the recovery of crystals in a separation device. The conventional methods for the recovery of the formed crystals are solid-liquid separation equipment such as filters and centrifuges (Gerard F.Arkenbout; Kim and Mersmann, 1997). The operational temperature range of melt crystallization stays within the crystallization temperature of the solution and melting temperature of the pure compound. The eutectic temperature is the lowest temperature of the solution. For instance, the eutectic temperature of sodium chloride is -21.1°C , whereas the melting point of the pure compound is 801°C (Gerard F.Arkenbout).

3.1.1.1 Supersaturation

The driving force for the crystallization process to appear solid phase in a saturated solution is supersaturation (Peter Crafts, 2007). Supersaturation is created mainly by cooling, evaporation of the solvent or by adding an extra substance (Kramer and van Rosmalen, 2000; Mullin, 1993). Based on the thermodynamic, the driving force for crystallization process can be represented by the chemical potential difference of solute in the liquid and solid phase at temperature T and pressure P (Kramer and van Rosmalen 2000):

$$\Delta\mu = \mu_{Li} - \mu_{Sl} \quad 3.1$$

For cooling crystallization from the melt or solution, Van't Hoff equation can be applied and Equation 3.1 reads (Gerard F.Arkenbout,1997):

$$\Delta\mu = -\Delta H (T-T_m)/T_m \quad 3.2$$

In Equation 3.2, ΔH represents the formation enthalpy and T_m the melting temperature of the pure component.

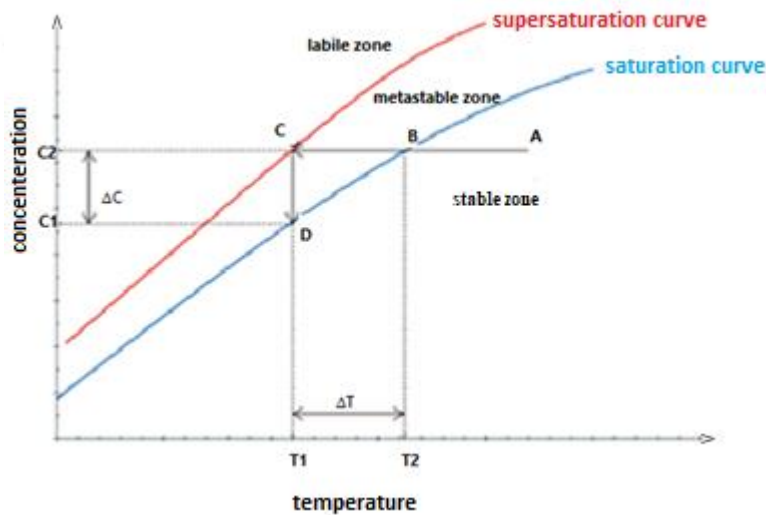


Figure 3.1: Solubility diagram showing stable, labile and metastable zones (Wojciech and Januez, 2014).

As shown in Figure 3.1, there are two main curves in the solubility diagram for a cooling crystallization, namely supersaturation and saturation curve which divide the diagram into three reigns, including labile (saturated), metastable and stable (unsaturated) zones (Wojciech and Januez, 2014). The labile or unstable zone is the saturated region where nuclei grow spontaneously. The most significant region among

these three regions is the metastable zone which is a supersaturated region that first crystal nuclei appear, because in this region there is a thermodynamic equilibrium between solid and liquid phases. The region below the saturation curve is the stable zone where is an unsaturated region that the crystals dissolve (Ulrich and Jones; Wojciech and Januez, 2014). In Figure 3.1, a solution of known concentration C_2 at the saturation temperature above T_2 at point A which is below the solubility curve is cooled at a constant rate. Therefore, if the solution becomes saturated at point B, and is cooled until T_2 at point C, the first crystals are formed spontaneously and appeared in the solution.

3.1.1.2 Nucleation

The process of the birth of the new nucleus from a thermodynamic phase with high free energy to an arranged structure with a low free energy is the nucleation which plays remarkable in the various aspects of the science like from the crystallization to the volcanic eruptions, the clouds, the snow, the rainfall and so on (Karthika et al., 2016). There are two types of nucleation to produce a new crystal: primary and secondary nucleation. The primary nuclei are formed in the absence of the crystals, while the secondary nucleation occurs when there are a sufficient number of crystals and supersaturation drops within the metastable zone (Agrawal and Paterson, 2015; Gerard F.Arkenbout,1997). The primary nucleation is classified into homogenous and heterogeneous. The homogenous primary nucleation is considered when a system which is in a stable state, becomes metastable by the thermal fluctuations and the foreign particles and the surfaces do not have any effect on this phenomenon (Karthika et al., 2016).

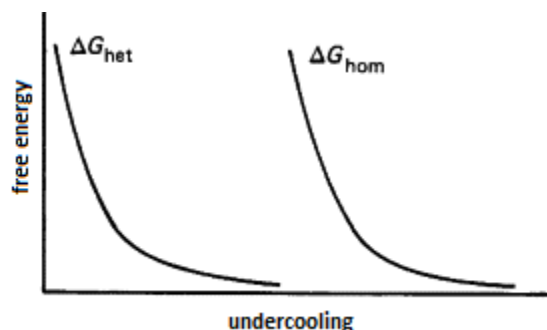


Figure 3.2: The relationship between free energy with undercooling (Elliott, 1988).

In contrast to the homogenous nucleation, the heterogeneous nucleation occurs at the interface of the vessel walls, a foreign particle like a dust particle and impurities. In the heterogeneous nucleation, there are three interfaces which can be considered: the liquid catalyzer, the nuclei catalyzer and the nuclei liquid interfaces. (A.Ananthanarayanan et al., 2017). In comparison to the homogenous nucleation, the heterogeneous nucleation can occur at a lower supersaturation (Karthika et al., 2016). As shown in Figure 3.2, the heterogeneous nucleation occurs at lower undercooling as a supersaturation that it is achieved by highly reducing free energy (Elliott, 1988). In Figure 3.2, ΔG_{hom} and ΔG_{het} represents the change in free energy accompanying the formation of nuclei in a solution.

According to various studies, there are several different mechanisms which can cause secondary nucleation. For example, initial breeding, Needle breeding, fluid shear forces, and contact nucleation are the different types of the secondary nucleation mechanisms (Garside and Davey, 1980). The process conditions and the solution compound play a leading role in the contribution of the secondary nucleation mechanisms (Agrawal and Paterson, 2015).

3.1.1.3 Crystal growth

In the crystallization process, after the formation of stable nuclei, it can grow into visible size. This process is known as crystal growth (Makoto Tachibana, 2017). The crystal growth is a two-step mechanism: in the first step, the solute molecules diffuse from the solution onto the surface of growing crystal. Then, these molecules adsorb onto the surface, diffuse along the surface and attached to the step surface. The growth rate at velocity G can be calculated by (Gerard F.Arkenbout, 1997):

$$G = \frac{dL}{dt} \tag{3.3}$$

In Equation 3.3, L and t represent the characteristic lengths and time.

The required supersaturation to start the crystal growth is generally lower than the secondary nucleation and the supersaturation to start the secondary nucleation is less than the primary nucleation (Gerard F.Arkenbout, 1997).

3.1.2 Eutectic freeze crystallization (EFC)

3.1.2.1 Definition and separation principle

The conventional methods to separate highly soluble salts from their aqueous solution are either the cooling or the evaporative crystallization. In the evaporative crystallization energy consumption is high and frequently is not economical, and due to the residual solubility at a low temperature, the cooling crystallization is not a high-efficiency process. (Zijlema et al., 2000; van der Ham et al., 1998). Eutectic Freeze Crystallization (EFC) which is novel technology can be a proper alternative. EFC process which advances based on density difference between ice and salt separates these solids by the gravity force (Randall et al., 2011; van der Ham et al., 1999).

The solubility for a binary phase diagram for a eutectic system is shown in Figure 3.3. The temperature and the concentration of a solid which is in equilibrium with the solution can be determined by the solubility lines. The intersection of the ice and the salt equilibrium lines is the eutectic point (point C). (Genceli et al., 2005)

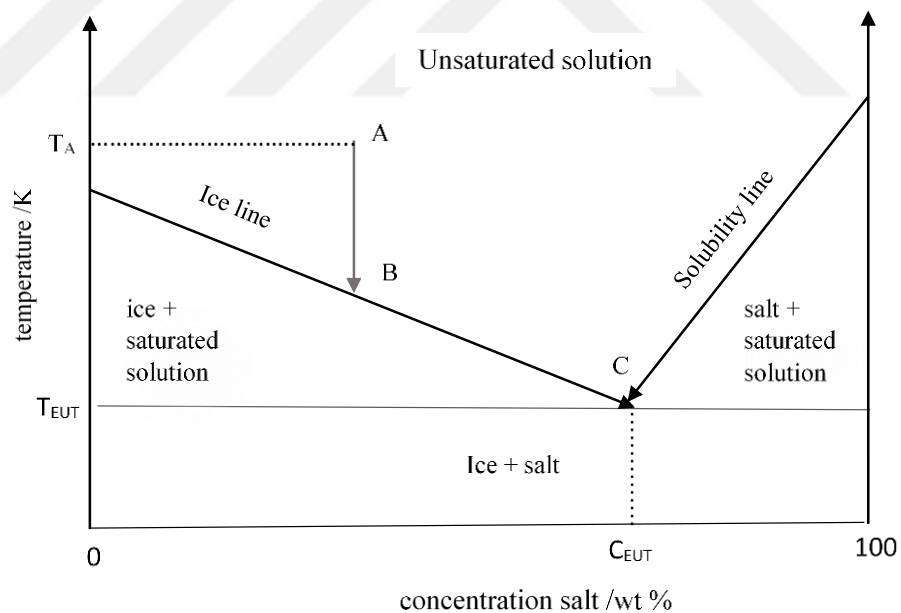


Figure 3.3: General phase diagram for binary aqueous solutions.

A solution with the temperature and the concentration of point A is cooled until point B where is on the ice line. At point B, the ice is formed, and the concentration of the solution increases. In the continuation of cooling, the temperature of the solution decreases and its concentration increases until the point C which is the eutectic point

(EP). At EP, the ice line intersects the solubility line of the salt. The temperature and concentration of solution at EP are called eutectic temperature (T_{EUT}) and eutectic concentration (C_{EUT}). When the concentration of solution is higher than the eutectic concentration, the salt is formed and then the ice begins to crystallize (van der Ham et al. 1999).

3.1.2.2 EFC process and its advantages

The EFC process is shown in Figure 3.4 and main units are introduced.

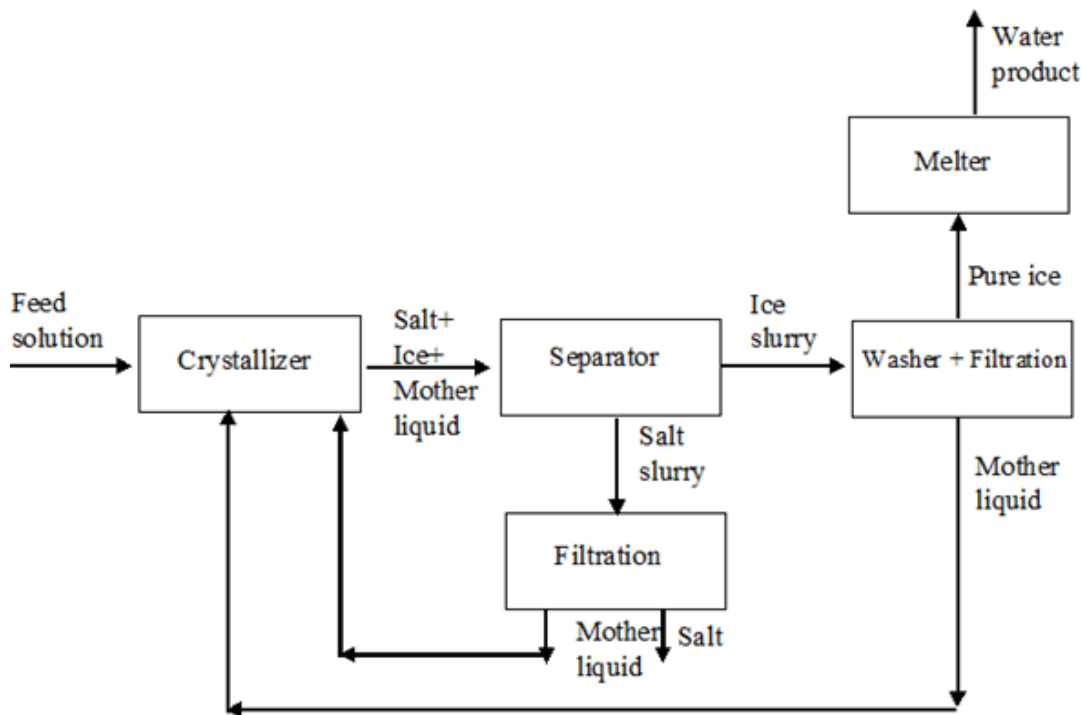


Figure 3.4: Schematic representation of EFC process

In Figure 3.4, the ice and salt crystals are sent to a separator column and separated due to their density difference, then the ice washed in a wash column and melted to yield a nearly pure water stream. Theoretically, the efficiency of the EFC process in the production of pure ice and solid salt is 100%, which is one of the advantages of this system (Williams et al., 2015).

In addition to the high efficiency of the EFC process, there are several other advantages for this process:

- Due to the separation of ice and salt from the solution by density difference, in this process, there is no need for separation unit like filtration (Hasan et al. 2017).

- The energy consumption in EFC process is less than the evaporative process. Because the heat of the evaporation is six times higher than the heat of the fusion (Randall et al. 2011).
- In the EFC process, the low operating temperature decreases the corrosion potential. Thus, cheaper construction materials can be used (Randall et al. 2011).
- Due to no chemical compound are not added, the EFC process is not so complicated (Lorain et al. 2001).

3.1.3 Sodium chloride solution

One of the most abundant kinds of salts is sodium chloride (NaCl) which plays a remarkable role in some industries such as food industry (Aragones et al. 2012). Generally, sodium chloride exists in two forms: anhydrous and dihydrate. The anhydrous form is the most common form of NaCl which occurs at the temperatures above 0.1 °C. On the other hand, the dehydrate form occurs at low temperatures. Despite the anhydrous form, dehydrate form is almost temperature independent. The solubility-temperature curves for the NaCl·2H₂O and NaCl are given in Figure 3.5.

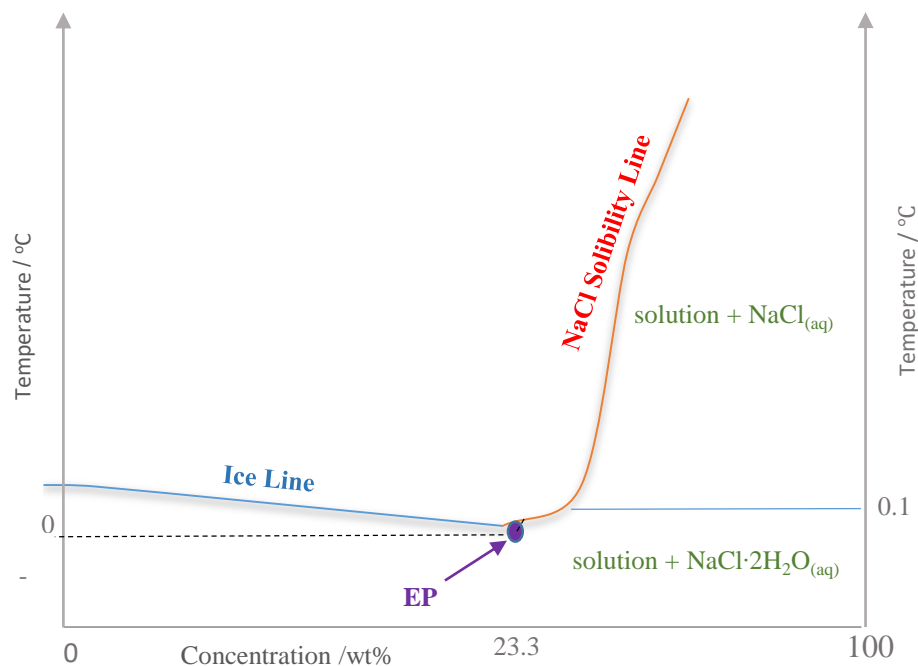


Figure 3.5: Phase diagram of NaCl solution according to Taschenbuch für Chemiker und PhysikernBand

In Figure 3.5 the phase diagram of NaCl and water is shown. As shown in Figure 3.5, at the eutectic point, the sodium chloride dihydrate solution is in the dihydrate form

($\text{NaCl}\cdot 2\text{H}_2\text{O}$). In this point, the temperature and the concentration of the solution are -21.1°C and 23.3 %, respectively. The eutectic temperature of $\text{NaCl}\cdot 2\text{H}_2\text{O}$ system in comparison with other salt and water systems like $\text{Na}_2\text{SO}_4/\text{H}_2\text{O}$, $\text{KCl}/\text{H}_2\text{O}$ and $\text{MgSO}_4/\text{H}_2\text{O}$ is low and more energy is needed to achieve the eutectic point (Li et al. 2013).

3.1.4 Ice layer formation

In the cooled surfaces like the bottom of the crystallizer at EFC, there is a significant tendency in ice to stick a chilled surface. Due to thermal conductivity of ice is almost 10-20 times lower than the thermal conductivity of stainless steel, it has a notable effect the on the solution heat transfer. Furthermore, the ice layer increases the thickness of crystallizer bottom that it decreases heat transfer coefficient of crystallizer bottom.

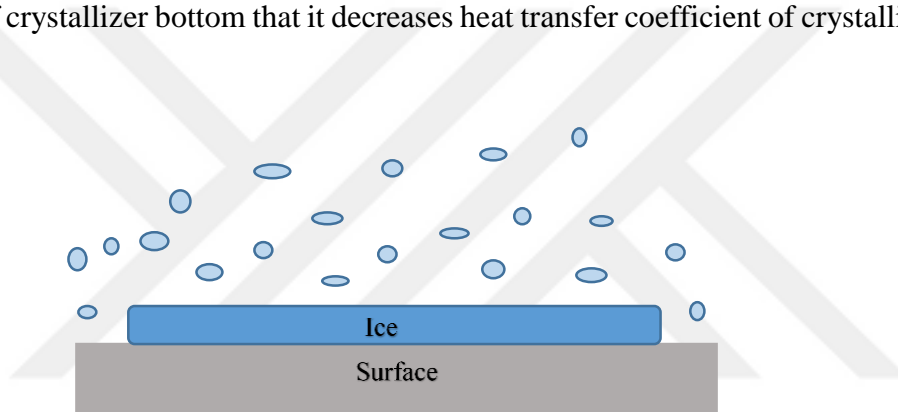


Figure 3.6: Scale formation during the EFC process.

One of the biggest problems which decrease the heat transfer in EFC process is the formation of an ice scale on a cooled surface that it is shown in Figure 3.6 (Hubbe et al., 2018; Vaessen et al., 2003a; Vaessen et al., 2003b). The rate of the ice formation on the cooled surface often needs several times to a detectable level on the chilled surface of the EFC system (Hubbe et al. 2018). Furthermore, the temperature has a remarkable effect on the onset of ice accumulation (Vaessen et al. 2003a; Hubbe et al. 2018).

3.1.5 Usage of a scraper in EFC processes

One of the most common ways to prevent ice layer formation on the chilled surface of a crystallizer is using of moving devices such as scrapers or wipers which remove the ice layer continuously (Stamatiou et al., 2005). Thus heat transfer is increased. Typically, a higher rotational speed causes higher turbulence of the system, and it

causes a higher process heat transfer coefficient from coolant to the solution. Furthermore, the penetration theory can describe the effect of the scrapping rate on the heat transfer coefficient (Hubbe et al., 2018; P. Pronk, M. Rodriguez Pascual, Geert-Jan Witkamp, 2005).

The heat transfer coefficient increases by increasing of scrapping rate. However, higher rotational speed consumes more power. Therefore, it needs an optimum amount for the scripting rate because a low amount of the scraping rate cannot remove the ice scale which is formed on the cooled surface, and also a high increases the scraper power consumption (Vaessen et al., 2003b; Hubbe et al., 2018).

3.1.6 The state of art

EFC is a branch of freeze crystallization which is referred the late 1600s when neither the freezers nor refrigerators were not invented, and the process was performed in the winter or cold conditions (Williams et al., 2015; Hasan et al., 2017). In 1968, Swenne and Theones applied EFC process for the sodium chloride solution (Swenne, 1983). The solution was cooled down by injecting coolant to crystallizer directly that was recommended by Stepakoff et al (Stepakoff et al., 1974). According to that studies, although direct injection was economical, but, it may contain contaminants in the product (Swenne, 1983; Verbeek, 2011). In 1998, Witkamp et al proposed a novel method to cool down the solution by indirect cooling where the coolant was not combined with the solution to purify wastewater stream which contained sodium nitrate and copper sulfate. In that research, the recommended crystallizer was a cooled disk column crystallizer (CDCC) (van der Ham et al., 1998). In that kinds of crystallizer, heat was eliminated through the cooled disks which perform as rotating disks in the extraction. Furthermore, in CDCC, to avoid formation of ice layer on the disks, they were installed with the scrapers which wipe the disks (van der Ham et al., 1998). Then, in 2003, Vaessen considered EFC process in a 100 liter CDCC for an Aqueous $\text{KNO}_3 \cdot \text{HNO}_3$ solution (Vaessen et al., 2003b). This new pilot scale CDCC could separate ice and salt acceptably that it was remarkable evolution in EFC process for large scales (Vaessen et al., 2003b). In the following, Vaesen introduced the scraped cooled wall crystallizer (SCWC) for aqueous $\text{KNO}_3 \cdot \text{HNO}_3$ (Vaessen et al., 2003a). In SCWC, the scraper enhanced the overall heat transfer coefficient and prevented ice layer formation on the cooled surface. Besides mentioned studies,

Vaessen considered CO₂ clathrates as a direct cooling method (VAESSEN et al., 2000). In this way, instead of ice, CO₂ clathrates were crystallized. In 2008, Genceli studied on scaling up of EFC process and considered this system for MgSO₄ solution (Genceli, 2008). The feasibility of sodium bicarbonate production by EFC process is shown by Witkamp and Van Spronsen was shown as research patent in 2010 (Witkamp and van Spronsen, 2010). In recent studies, Leyland et al studies on the process conditions such as the scraper rotational speed to decrease potential of ice layer formation on the cooled surface of crystallizer that it is concluded that the potential of ice layer decreases during a multicomponent brine crystallization in comparison to a binary solution (Leyland et al., 2019).

3.2 Qualitative Analysis of EFC Process

3.2.1 Qualitative analysis of EFC process in non-crystallizing condition

In this section, the crystal formation in the solution is neglected. Firstly, it is assumed that the solution is in the steady state and temperature of the solution is constant at the eutectic temperature. In this condition, heat transfer of crystallizer is represented by the heat of coolant ($\dot{Q}_{coolant}$), the heat of loss to the environment (\dot{Q}_{loss}) and the scraper power consumption (P_s).

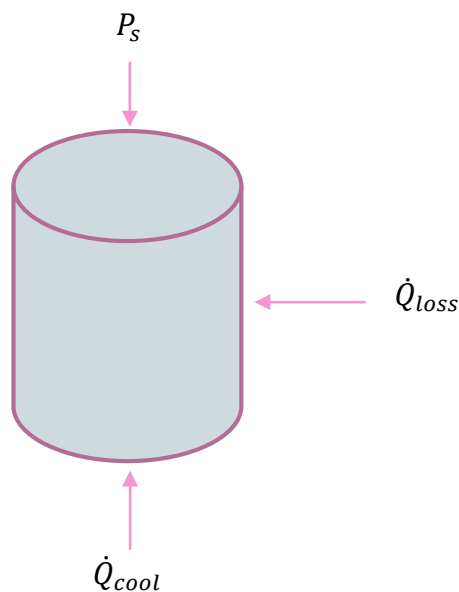


Figure 3.7: Scheme of heat transfer in a crystallizer in non-crystallizing condition

According to the Figure 3.7, the total heat balance of the crystallizer can be determined by:

$$0 = \dot{Q}_{cool} - P_s - \dot{Q}_{loss} \quad 3.4$$

The \dot{Q}_{cool} represents the heat transfer from the coolant to the solution, \dot{Q}_{loss} the heat loss from the solution and through the wall of crystallizer to the environment and P_s the scrapper power consumption. It should be noted that, if the temperature difference between the solution and the environment becomes zero, the lost heat from the wall can be neglected. Therefore, according to Equation 3.4:

$$0 = \dot{Q}_{cool} - P_s \quad 3.5$$

The heat transfer of the coolant and the scraper power consumption play a remarkable role in Equation 3.5. In the following, these parameters will be discussed in detail.

3.2.1.1 Scraper Power Consumption (P_s)

The power consumption of a scraper to disturb a solution in a crystallizer can be approximated from Newton number. The Newton number is a function of the Reynolds number (Re) and the Froude number (Fr) (VDI Heat Atlas, 2010). The power consumption of the scraper can be calculated by Equation 3.6. In these equations, ρ_s represents the density of the solution, N the rotational speed of the scraper and d_r the diameter of the scraper.

$$Ne = \frac{P_s}{\rho_s N^3 d_r^5} \quad 3.6$$

$$Re = \frac{\rho_s N d_r^2}{\mu_s} \quad 3.7$$

$$Fr = \frac{N^2 d_r}{g} \quad 3.8$$

These dimensionless numbers can be calculated by Equation 3.7 and Equation 3.8. In these equations, μ_s represents the viscosity of the solution and g the gravity acceleration. The Froude number can be determined when there are fluid dynamic effects such as vortex formation. Therefore, it depends on the system whether the baffle is used in the crystallizer or not. If the vortex formation is suppressed, the Froude number in Equation 3.8 can be neglected. Also if it is assumed that the crystallizer will be baffled, for the systems having the same geometrical ratios but different sizes, the

Newton number will be just a function of the Reynolds number. In this study, in order to prevent the ice layer formation on the bottom of the crystallizer, the blade type of the stirrer is so essential.

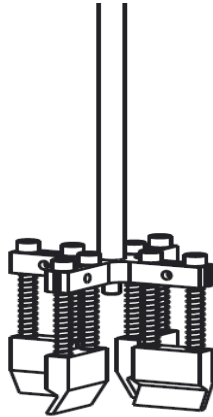


Figure 3.8: Scheme of the selected impeller

In Figure 3.8, the selected stirrer for this study is shown. However, the scrapers and their equations in the VDI heat atlas are different from the selected impeller. Therefore, three types of the stirrer which are in the VDI heat atlas are considered, and the Newton number is calculated for a baffled system.

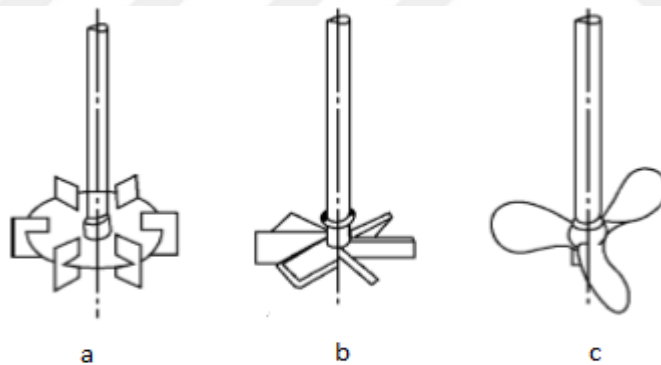


Figure 3.9: (a) flat-blade turbine, (b) pitched-blade impeller, (c) marine-type propeller (VDI Heat Atlas, 2010)

For a baffled system with a flat-blade turbine (Figure 3.9.(a)), Hirschberg have recommended the following equations in the various amounts of the Reynolds number to determine the Newton number (VDI Heat Atlas, 2010):

$$Ne = \frac{80}{Re} \quad \text{for} \quad 1 < Re < 16, \quad 3.9$$

$$Ne = 5 \quad \text{for} \quad 16 < Re < 10^5, \quad 3.10$$

The Newton number of a Pitched-blade impeller (Figure 3.9 (b)) in a baffled crystallizer can be calculated by (VDI Heat Atlas, 2010):

$$Ne = \frac{80}{Re} \quad \text{for} \quad 1 < Re < 40, \quad 3.11$$

$$Ne = 2 \quad \text{for} \quad 40 < Re < 10^5, \quad 3.12$$

Hirschberg's recommendation to compute the Newton number of a marine-type propeller is (VDI Heat Atlas 2010) :

$$Ne = 50 \quad \text{for} \quad 1 < Re < 3.1, \quad 3.13$$

$$Ne = \frac{4}{(\log Re)^2} \quad \text{for} \quad 3.1 < Re < 635, \quad 3.14$$

$$Ne = 0.8Re^{-0.07} \quad \text{for} \quad 635 < Re < 2 \times 10^5 \quad 3.15$$

3.2.1.2 Heat transfer through a scraped surface

In this section, the heat transfer through the scraped surface will be considered. In this regard, it contains the heat transfer from the solution to the scraped surface, the heat transfer through the scraped bottom of the crystallizer and also from the bottom of crystallizer to the coolant is considered (Figure 3.10). The heat transfer between the coolant and the solution is defined by:

$$\dot{Q}_{cool} = U_{overall} A_{cryst} \Delta T_{LN}, \quad 3.16$$

In Equation 3.16 to calculate the heat transfer through the scraped surface \dot{Q}_{cool} are the overall heat transfer coefficient $U_{overall}$, the heat transfer area A_{cryst} and also the logarithmic mean temperature difference between the coolant and the solution ΔT_{LN} . In the steady state, the temperature of solution (T_{EUT}) is constant. But, due to the temperature of the coolant varies between inlet (T_{in}) and outlet (T_{out}) temperatures, to calculate the temperature difference between the coolant and the solution, it is necessary to use the logarithmic mean temperature difference (Equation 3.17)

$$\Delta T_{LN} = \frac{(T_{in}) - (T_{out})}{\ln\left(\frac{T_{EUT} - T_{in}}{T_{EUT} - T_{out}}\right)} \quad 3.17$$

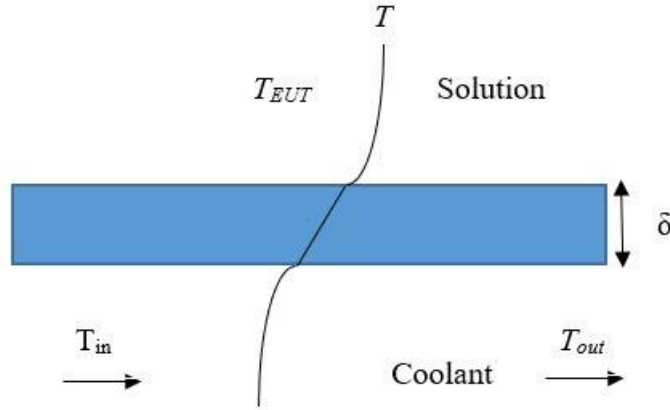


Figure 3.10: Schematic representation of heat transfer in coolant surface.

The heat transfer in the coolant and the solution is convective, and the heat transfer through the bottom of the crystallizer is conductive. The relation between the overall heat transfer coefficient $U_{overall}$ and the individual heat transfer coefficients of the solution α_S , through the bottom of the crystallizer α_{bottom} and the coolant α_{cool} , if it is assumed that the surface area is the same at each surface is given by (Vaessen et al. 2003a) :

$$\frac{1}{U_{overall}} = \frac{1}{\alpha_S} + \frac{1}{\alpha_{bottom}} + \frac{1}{\alpha_{cool}} \quad 3.18$$

Coolant heat transfer coefficient

In this section, the heat transfer coefficient for the heat transfer from the coolant to the surface area is considered. The first step to consider this term is to determine whether the boundary layer is laminar or turbulent. Therefore, the Reynolds and Prandtl numbers must be calculated. The Reynolds number can be calculated by (Bergman and Incropera 2011):

$$Re = \frac{\rho_c u d_t}{\mu_c} \quad 3.19$$

In Equation 3.19, ρ_c represents the coolant density, μ_c the coolant viscosity, d_t the tube diameter and u the coolant velocity through the tube, which can be define as (Vaessen et al., 2003a);

$$u = \frac{\dot{V}}{A_t} \quad 3.20$$

The volumetric flow rate \dot{V} can be calculated by the coolant velocity. The surface area of the tube A_t is computed by:

$$A_t = \frac{\pi d_t^2}{4} \quad 3.21$$

The other parameter to characterize the flow regime is the Prandtl number, which can be defined as (Bergman and Incropera, 2011):

$$Pr = \frac{\mu_c \cdot c_{pc}}{\lambda_c} \quad 3.22$$

In Equation 3.22, c_p represents the heat capacity of the coolant and λ_c the thermal conductivity of the coolant. According to the value of the Prandtl and the Reynolds numbers, the flow regime can be determined, and consequently, the Nusselt number can be calculated. By knowing the value of Nu , the coolant heat transfer coefficient can be computed. The Nusselt number for turbulent flow in circular tubes can be computed by (Bergman and Incropera, 2011):

$$Nu = 0.023Re^{0.8}Pr^{0.3} \quad 3.23$$

Equation 3.23 is valid if the Prandtl number is between 0.6-160 and the Reynolds number is higher than 10000. If the boundary layer is laminar, Nu can be calculated by (M. A. Mehrabian):

$$Nu = \left(3.65 + \frac{0.0668\left(\frac{RePrd_t}{L_t}\right)}{1+0.04\left(\frac{RePrd_t}{L_t}\right)^{2/3}}\right) \quad 3.24$$

Equation 3.24 could be valid if the Prandtl number is higher than five and also the Reynolds number should be less than 2300. As mentioned above, for the Reynolds numbers less than 2300, the flow regime will be the laminar, and above 10000 will be the fully developed turbulent. In Equation 3.24, L_t represents the length of the tube. In between, the flow will be in the transition. The equation for the transition region can be determined according to (Yu-ting et al., 2009):

$$Nu = 0.037(Re^{0.75} - 180)Pr^{0.42} \times \left[1 + \left(\frac{d_t}{L_t}\right)^{\frac{2}{3}}\right] \left(\frac{\mu_{cm}}{\mu_{cw}}\right)^{0.14} \quad 3.25$$

The equation above covers between the Reynolds numbers of 2300 and 10^6 . Also, the Prandtl numbers from 0.6 to 1000. In Equation 3.25, μ_{cm} is the viscosity of the coolant at T_{cool} (average of inlet and outlet temperature of coolant) and μ_{cw} is the viscosity of the coolant at T_b (bottom temperature of the crystallizer). The coolant heat transfer coefficient is a function of the Nusselt number. In this regard, the coolant heat transfer coefficient can be calculated by (Bergman and Incropera, 2011):

$$\alpha_{cool} = \frac{\lambda_c \cdot Nu}{d_t} \quad 3.26$$

Solution heat transfer coefficient

In order to consider the impact of the number of scraper blades on the heat transfer coefficient of the scraped surface, the penetration theory is used (Vaessen et al., 2003a). This theory describes the temperature distribution around a non-scraped semi-infinite body that the temperature changes may happen in a region that is thin in comparison to the overall dimensions of the body (VDI Heat Atlas, 2010). In this case, it is assumed that the scraper removes the formed layer on the surface and a new layer which has the temperature of the bulk settles on the scraped surface. In this case, the solution with a constant initial temperature T_{bulk} is considered. In the beginning, the surface temperature of the scraped surface is reduced to a temperature below the temperature of the crystallizer T_{EUT} and then remains constant (VDI Heat Atlas, 2010). In Figure 3.5, the development of the thermal boundary layer after each scraper blade pass is shown.

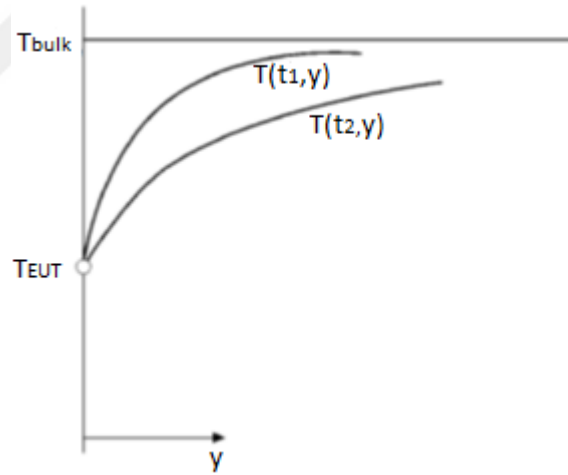


Figure 3.11: Development of the temperature profile after each scraper blade pass (VDI Heat Atlas, 2010).

In this case, the temperature profile at different times t_1 , t_2 and etc. can be derived by the Fourier equation which is shown in Equation 3.27 (VDI Heat Atlas, 2010). In this equation, the heat transfer by a temperature in axial direction is neglected.

$$\frac{\partial T}{\partial t} = a \cdot \frac{\partial^2 T}{\partial y^2} \quad 3.27$$

$$a = \frac{\lambda}{\rho \cdot c_p} \quad 3.28$$

In Equation 3.28, a is a material property and can be described as the thermal diffusivity and also it is assumed that the temperature of the bulk is T_{bulk} , the temperature of the layer on the scraped surface is T_{EUT} and as mentioned above, at the time $t=0$, the temperature of the solution is T_{bulk} . By solving Equation 3.27 at the boundary conditions and substituting into relation for heat transfer, the heat flux on the bottom of the crystallizer can be computed by (VDI Heat Atlas, 2010; Vaessen et al., 2004):

$$\dot{q} = -\lambda \left(\frac{\partial T}{\partial y} \right)_{x=0} = \sqrt{\frac{\lambda \rho C_p}{\pi t_s}} (T_{Bulk} - T_w) \quad 3.29$$

According to Equation 3.29, the heat transfer coefficient at the surface can be calculated as a function of time by:

$$\alpha_s(t) = \sqrt{\frac{\lambda_s \rho_s C_p}{\pi t_s}} \quad 3.30$$

In Equation 3.30, the heat transfer coefficient at the scraped surface α_s can be calculated by the thermal conductivity of the solution λ_s , the density of the solution ρ_s , the specific heat of the solution c_p and the time between two scraper actions t_s . If the heat transfer coefficient can be described by the penetration theory, the time mean value of the heat transfer coefficient will be determined by (Vaessen et al., 2004):

$$\alpha_{s,avg} = \frac{1}{t_s} \int_0^{t_s} \alpha_s(t) dt = 2 \sqrt{\frac{\lambda_s \rho_s C_p}{\pi t_s}} \quad 3.31$$

Due to the scraper blade affects the flow pattern and the bulk mixing intensity, Equation 3.31 must be changed to be as a function of the number of the blades and the scraper rotational speed. Each time step is the period between the scraper blade passes. Therefore, the time between two scraper actions in terms of the number of blades m and rotational speed N can be described as (Vaessen et al. 2004):

$$t_s = \frac{1}{mN} \quad 3.32$$

Combination of Equation 3.31 and Equation 3.32 results in the heat transfer coefficient of the solution as a function of the rotational speed and the number of the scrapers which is calculated by:

$$\alpha_s = 2 \sqrt{\frac{\lambda_s \rho_s C_p m N}{\pi}} \quad 3.33$$

Heat transfer through the bottom of the crystallizer

The third term to calculate the overall heat transfer coefficient is the conductive heat transfer through the bottom of the crystallizer. The heat conduction through the bottom of the crystallizer under steady state can be considered from Fourier's law and can be calculated by (VDI Heat Atlas, 2010);

$$\alpha_{bottom} = \frac{\lambda_{bottom}}{\delta} \quad 3.34$$

In Equation 3.34, the conductive heat transfer coefficient of the bottom of the crystallizer α_{bottom} is calculated from the thermal conductivity of the bottom of the crystallizer λ_{bottom} and the thickness of the bottom δ .

By calculating the three terms of the heat transfer coefficients, the overall heat transfer and consequently the heat transfer from the coolant to the solution can be computed by Equation 3.18 and Equation 3.16 respectively. The heat transfer from the coolant to the solution can also be calculated from the heat uptake equation. By equalizing Equation 3.16 and Equation 3.18, the unknown parameters like the coolant outlet temperature, the bottom of the crystallizer temperature and the heat flux from the coolant to the solution can be determined and optimized by adjusting the independent parameters like coolant volumetric flow rate, the coolant inlet temperature and scraper rotational speed (Vaessen et al. 2003a).

$$Q_{cool} = \dot{V}_{cool} \rho_{cool} C_p (T_{out} - T_{in}) \quad 3.35$$

3.2.1.3 Heat balance under unsteady state

In the previous part, it was assumed that the initial temperature of the solution is the eutectic temperature and no energy was consumed to decrease the temperature of the solution to eutectic temperature. In this section, it is assumed that the solution is at the environment temperature and some part of the energy which is transferred from coolant to the solution will be consumed to decrease the temperature of solution until the eutectic temperature. Therefore, the heat balance in part 3.1 which is under steady state, will be changed. In Figure 3.12, the heat transfer under unsteady state is shown. In this figure, \dot{Q}_{Feed} represents consumed energy to cool down the solution to the eutectic temperature and as steady state, it is assumed that the heat of loss is zero. Therefore, the heat balance equation can be shown as Equation 3.36.

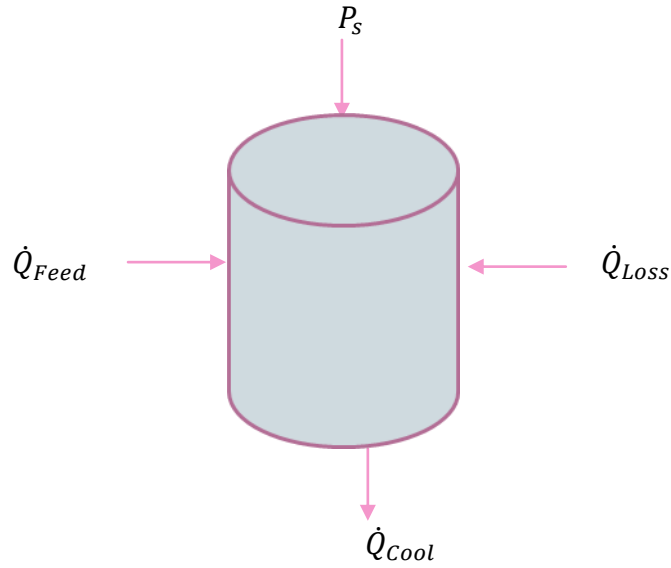


Figure 3.12: The heat balance in the EFC process under unsteady state and in non-crystallizing condition.

$$0 = \dot{Q}_{cool} - \dot{Q}_{Feed} - P_S \quad 3.36$$

In Equation 3.36, \dot{Q}_{Feed} is a function of solution the temperature which is changed over the cool down time and can be calculated by (Hasan et al, 2017) :

$$\dot{Q}_{Feed} = m \cdot c_{ps} \cdot \frac{dT}{dt} \quad 3.37$$

In Equation 3.37, m and t represent the mass of solution and time, respectively. Furthermore, due to the coolant temperature difference over the heat transfer surface area is negligible, coolant temperature can be assumed constant and Equation 3.13 is changed to:

$$\dot{Q}_{cool} = U_{overall} A_{cryst} (T_{sol} - T_{cool}) \quad 3.38$$

In Equation 3.38, T_{sol} and T_{cool} represent solution temperature which is a function of time and coolant temperature, respectively. By combining Equation 3.37 and Equation 3.38 in Equation 3.36, the heat balance equation under unsteady state condition can be written as:

$$U_{overall} A_{cryst} (T_{sol} - T_{cool}) = m \cdot c_{ps} \cdot \frac{dT}{dt} + P_S \quad 3.39$$

In Equation 3.39 by integrating the temperature as a function of time, the time required to cool down the solution from the environmental temperature to the eutectic temperature can be calculated. Therefore, under unsteady state condition, the relationship between the solution temperature and time can be shown as:

$$\ln \frac{U_{overall} A_{cryst} (T_{EUT} - T_{cool}) - P_s}{U_{overall} A_{cryst} (T_{sol} - T_{cool}) - P_s} = \frac{U_{overall} A_{cryst}}{m c_{ps}} t \quad 3.40$$

In Equation 3.40, only T_{sol} is changed during the time and other parameters are constant. Although, the higher scraper rotational speed and volumetric flow rate increase the overall heat transfer coefficient, and the scraper power consumption increases with increasing the rotational speed, but, according to Equation 3.40, each of these independent variables may have different effect on solution cooling rate that which will be considered in the next chapter with details.

3.2.2 Qualitative analysis of EFC process in the crystallizing condition

In the previous section, it was assumed that there is not any crystal in the system and process was considered in the non-crystallizing condition for both steady and unsteady states. In this part, it will be assumed that there is the crystal formation in the system at the eutectic point. In Figure 3.13, the heat balance in the crystallizing condition is shown. In this figure, in addition to P_s , \dot{Q}_{cool} and \dot{Q}_{loss} which are the same as the non-crystallizing condition and \dot{Q}_{ice} and \dot{Q}_{salt} are other energy terms which are related to the crystallization process and represent heat of the ice crystallization and the heat of salt crystallization, respectively (Vaessen et al. 2003a).

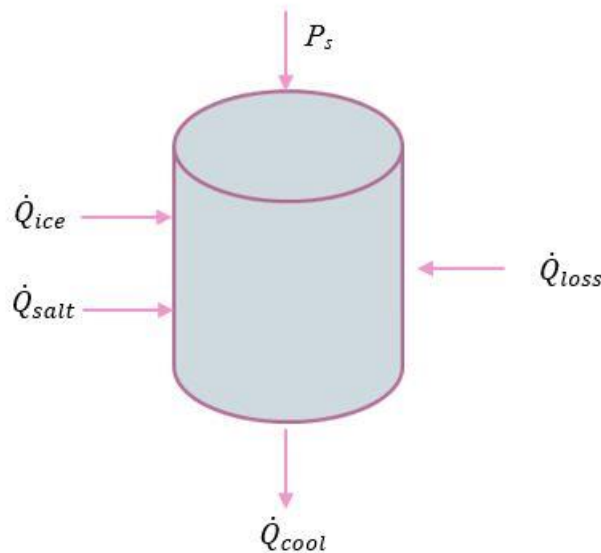


Figure 3.13: The heat balance in the crystallizing condition.

According to Figure 3.13, if it is assumed that heat of loss is zero the relationship between heat flux from the coolant to the solution, stirrer power consumption and the

heats of crystallization can be shown by Equation 3.41 which will be considered with detail in the following.

$$0 = \dot{Q}_{cool} - \dot{Q}_{ice} - \dot{Q}_{salt} - P_s \quad 3.41$$

3.2.2.1 Effect of crystal formation on the solution physical properties

One of the main difference between non-crystalizing and the crystalizing condition is the physical properties of the solution, because, crystal particles based on their volume fraction in the solution can change the λ_s , ρ_s , μ_s and c_{ps} (Vaessen et al., 2004).

According to the phase diagram of sodium chloride solution, at the EP, more than 75% of the solid particles are ice (Lax et al). Therefore, in this study, the properties of ice will be applied as the properties of whole formed crystals. The first step to consider the effect of the crystals on the solution is to determine their mass fraction in the solution which can be calculated by mass fraction of solid particles in the slurry. In this study, due to the process is occurred at the eutectic point the concentration of solute which is dehydrate sodium chloride, is constant. However, after achieving EP mass fraction of crystal particles changes over time. The mass fraction of the crystals in the solution φ_m can be calculated by:

$$\varphi_m = \frac{m_c}{m_t} \quad 3.42$$

m_c and m_t represent the mass of the crystals particles in the solution at a specified time after achieving EP and the total mass of slurry, respectively. The mass of crystal particles at a specific time can be calculated by the heat of crystallization which can be calculated by Equation 3.42 and total mass of slurry is constant and is related to the initial condition of the process.

The slurry density is a function of crystal density and the solution density and can be calculated as (Meewisse and Infante Ferreira 2003) :

$$\frac{1}{\rho_{sl}} = \frac{\varphi_m}{\rho_i} + \frac{1-\varphi_m}{\rho_s} \quad 3.43$$

In Equation 3.43, ρ_{sl} represents the density of slurry and ρ_i represents the ice density which is assumed to use as crystal density in this study. ρ_i can be calculated as a function of the temperature T_i (Melinder, 2010):

$$\rho_i = 917 - 0.13T_i \quad 3.44$$

According to Equation 3.42 and Equation 3.43, the volume fraction of the solid particle in the slurry φ_v which is an important parameter to obtain other properties of slurry, can be calculated by Equation 3.45.

$$\varphi_v = \varphi_m \frac{\rho}{\rho_i} \quad 3.45$$

The other physical property of the solution which can be influenced by the solid particles is thermal conductivity. The thermal conductivity of dilute solid/liquid suspension can be calculated by the Maxwell relation (Martínez et al., 2014):

$$\lambda_{sl} = \lambda_s \left[\frac{2\lambda_s + \lambda_i - 2\varphi_v(\lambda_s - \lambda_i)}{2\lambda_s + \lambda_i + \varphi_v(\lambda_s - \lambda_i)} \right] \quad 3.46$$

Where λ_{sl} represents the thermal conductivity of slurry. Due to the lack of a valid way to measure the thermal conductivity of ice slurry, the reliability of Equation 3.46 cannot be proven experimentally (Meewisse and Infante Ferreira, 2003). In this study, the thermal conductivity of ice crystals are obtained from Bonales data who considered this matter under different conditions (Bonales et al., 2017). According to Equation 3.46, the ice crystals increase the thermal conductivity of the slurry which will be considered in the next chapter with detail.

The Enthalpy and heat capacity are other properties of a solution. The enthalpy of ice slurries at EP can be calculated by (Melinder, 2010):

$$H_{fsl}(T_{EUT}) = \varphi_m H_{fi}(T_{EUT}) + [1 - \varphi_m] H_{fs}(T_{EUT}, C_{EUT}) \quad 3.47$$

Where H_{fsl} represents the enthalpy of the ice slurry at the eutectic temperature, H_{fi} the enthalpy of the ice at the eutectic temperature and H_{fs} the enthalpy of solution at the eutectic temperature and concentration. In Equation 3.47, H_{fs} and H_{fi} can be obtained by Figure 3.14.

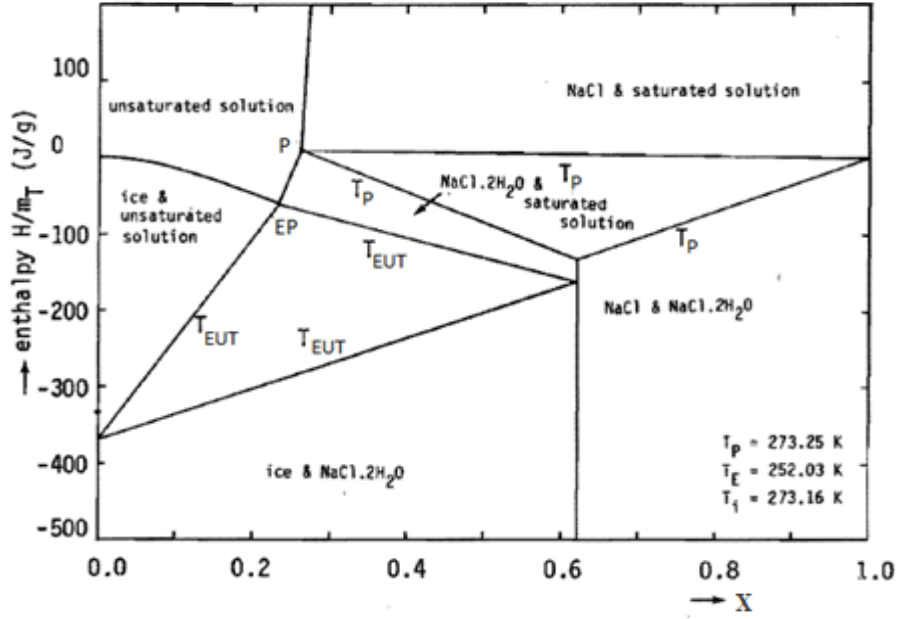


Figure 3.14: The enthalpy of solution as a function of sodium chloride concentration.

In Figure 3.14, the enthalpy of sodium chloride solution at the temperature between -21.1 and 0 °C is shown. In this diagram, it is assumed that $H = 0$ for liquid water and solid sodium chloride at $T = 0^\circ\text{C}$ (Swenne, 1983).

The heat capacity is obtained by differentiation of the enthalpy with respect to the temperature. In this study, process temperature is constant at the eutectic temperature. Therefore, if it is assumed that $H = 0$ for liquid water at $T = 0^\circ\text{C}$, the specific enthalpy of the ice slurry can be calculated by (Martínez et al., 2014):

$$c_{psl} = \varphi_m c_{pi} + (1 - \varphi_m) c_{ps} \quad 3.48$$

In Equation 3.48, c_{psl} represents the specific heat capacity of the ice slurry, c_{pi} the specific heat capacity of the ice and c_{ps} the specific heat capacity of the solution. c_{ps} is obtained by Archer's data (Archer and Carter, 2000b). Furthermore, c_{pi} can be calculated as a function of temperature. Due to the temperature of the process is constant at EP , the specific heat capacity of ice will be constant (Melinder, 2010).

$$c_{pi} = 2.12 + 0.008 T_{EUT} \quad 3.49$$

The dynamic viscosity of ice slurry μ_{sl} is calculated by the dynamic viscosity of the solution μ_s and volume fraction of ice. The proposed equation by Thomas for solid/liquid suspension can be used to obtain μ_{sl} . However, according to this equation,

if the ice fraction is zero, the viscosity of the slurry will not be equal to the viscosity of solution. Therefore, a correlation which is recommended by Melinder can be used (Melinder 2010). The experimental researches on this equation are shown that there are remarkable errors in the higher ice fraction included slurries (Meewisse and Infante Ferreira, 2003).

$$\mu_{sl} = \mu_s(1 + 2.5\varphi_v + 10.05\varphi_v^2 + 0.00273 \cdot (e^{16.6\varphi_v} - 1)) \quad 3.50$$

In Equation 3.50, μ_s can be calculated by the recommended equation of Ozbek (Ozbek 1977). In Equation 3.51, the dynamic viscosity is a function of temperature and concentration of the solution. Although this equation is derived for a temperature range between 10 °C and 150 °C, it can be interpreted to a standard deviation of 1.5% over the entire temperature, pressure, and concentration range.

$$\mu_s = 0.1256735 + 1.265347e^{-0.04296718T} - 1.105369e^{0.3710073M} + 0.2044679e^{0.4230889(0.01T+M)} + 1.308779e^{-0.3259828(0.01T-M)} \quad 3.51$$

Where M represents the molality of the solution.

3.2.2.2 The scraper power consumption

As mentioned in the previous section, the power consumption of a stirrer in a solution can be calculated by Equation 3.7. In this equation, the only parameter which is influenced by the solid particles in the solution is the density of solution. The density of the ice slurry is computed by Equation 3.43. By combining Equation 3.7 and Equation 3.43, the power consumption of stirrer in an ice slurry can be obtained (Equation 3.49).

$$Ne = \frac{P_{sl}}{\rho_{sl}N^3d_r^5} \quad 3.52$$

Due to the Reynolds number is a function of the solution density and dynamic viscosity, the crystal particles also impact on the Reynolds number of the solution. As mentioned above, the ice slurry density and dynamic viscosity are calculated by Equation 3.43 and Equation 3.50, respectively. Therefore, the Reynolds number of ice slurry can be calculated by Equation 3.53 which is derived by combining Equation 3.7, Equation 3.43 and Equation 3.50.

$$Re = \frac{\rho_{sl}Nd_r^2}{\mu_{sl}} \quad 3.53$$

3.2.2.3 Heat transfer through a scraped surface

The crystal particles impact on heat flux from the coolant to the solution by influencing on thermophysical properties of the solution and consequently on solution heat transfer coefficient. ρ_s , λ_s and c_{ps} of ice slurry are calculated by Equation 3.43, Equation 3.46 and Equation 3.48 and by substituting these equations into Equation 3.33, the heat transfer coefficient of ice slurry can be calculated (Equation 3.54).

$$\alpha_{sl} = 2 \sqrt{\frac{\lambda_{sl} \rho_{sl} c_{psl} n N}{\pi}} \quad 3.54$$

In Equation 3.54, the heat transfer of solution is independent of viscosity. However, in the higher amounts of ice mass fraction, the effect of viscosity is not negligible (Rao and Hartel, 2006). Therefore, it is necessary to derive an equation which contains the effect of viscosity on the heat transfer coefficient. In Equation 3.55, Nu is calculated as a function of Re_{sl} and Pr_{sl} and it is assumed that scarper has four blades and the effect of rotational speed on the heat transfer coefficient is neglected (Vaessen et al., 2003a).

$$Nu_{sl} = 0.83 Re_{sl}^{0.57} Pr_{sl}^{0.3} \quad 3.55$$

$$\alpha_{sl} = \frac{\lambda_{sl} Nu_{sl}}{d_r} \quad 3.56$$

The overall heat transfer coefficient is a function of solution heat transfer coefficient. Therefore, the ice particles will influence the overall heat transfer coefficient which is obtained by Equation 3.18. The overall heat transfer coefficient of the process will be derived by combining Equation 3.18 and 3.54 if the crystal particles are contained in the solution (Equation 3.55).

$$\frac{1}{A_{cryst} U'_{overall}} = \frac{1}{A_{cryst} \alpha_{sl}} + \frac{1}{A_{cryst} \alpha_{bottom}} + \frac{1}{A_{cryst} \alpha_{cool}} \quad 3.57$$

Where $U'_{overall}$ represents the overall heat transfer coefficient in crystallizing condition. According to Equation 3.57, the heat flux from the coolant to solution based on the mass fraction of crystals will be changed in the crystallizing condition which will be considered in the next chapter with detail.

3.2.2.4 Heat of crystallization

The heat release from the crystallization process is the heat of crystallization. The heat of crystallization is a function of the heat of fusion and crystallization production rate. The heat of crystallization can be obtained from solubility and activation data. \dot{Q}_{cryst} can be formulated as (Sonmez and Hahn 1997; Vacek and König, 1983):

$$\dot{Q}_{cryst} = H_f \frac{dm_c}{dt} \quad 3.58$$

In Equation 3.58, H_f represents enthalpy of. According to Figure 3.13, the heat of crystallization is divided into ice crystallization and salt crystallization. As mentioned previously, according to the solubility data at EP, more than 75% of the solid particle is ice. Furthermore, due to the lack of sufficient data about sodium chloride dehydrate at EP, in this study, it was assumed that all thermophysical properties of the crystal particles are related to ice. Therefore, in this study, the heat of crystallization will be assumed equal ice heat of fusion in different ice mass fraction and will be derived as:

$$\dot{Q}_{cryst} = \dot{Q}_{sl} \quad 3.59$$

$$\dot{Q}_{sl} = (\varphi_m H_{fi} + (1 - \varphi_m) H_{fs}) \frac{dm_c}{dt} \quad 3.60$$

\dot{Q}_{sl} , H_{fi} and H_{fs} represent heat of crystallization in the assumed condition, the fusion heat of ice and solution, respectively. Therefore, to consider the effect of ice and salt concentration proportion on the heat of crystallization, in Equation 3.60, the factors of the heat of fusion for H_{fi} and H_{fs} are considered based on the ice and solution mass fraction, respectively. By substituting Equation 3.59 into Equation 3.40, the production rate of crystals for sodium chloride solution at EP can be obtained.

$$\frac{dm_c}{dt} = \frac{\dot{Q}_{cool} - P_s}{(\varphi_m H_{fi} + (1 - \varphi_m) H_{fs})} \quad 3.61$$

In Equation 3.61, due to the temperature of solution is constant at EP, the production rate of the ice and salt crystals is linear. However, the heat of crystallization is a function of the ice mass fraction. Furthermore, the effect of slurry properties on \dot{Q}_{cool} and P_s is less and only the heat of fusion over the ice mass increase is changed. Thus, if it is assumed that until the eutectic temperature, no crystal is formed and the time required to produce m_c is t , Equation 3.61 can be derived as:

$$\int_0^{m_c} (m_c (H_{fi} - H_{fs}) + m_t H_{fs}) dm_c = \int_0^{t_2} m_t (\dot{Q}_{cool} - P_s) dt \quad 3.62$$

$$m_c^2 = \frac{m_t (2(\dot{Q}_{cool} - P_s)t - H_{fi} m_c)}{H_{fi} - H_{fs}} \quad 3.63$$

In Equation 3.63, m_c is a square root function of t , that, in the next chapter, the time require to produce various amounts of ice mass and also the effects of the process conditions on it also will be considered.

3.3. Results And Discussion

In Section 3.2, qualitative analysis for a batch EFC system was considered, and the parameters and the equations to model heat transfer in the crystallizer were introduced. In this section, by using equations and parameters of Section 3.2, the heat transfer for a batch EFC system which contains the sodium chloride solution will be considered numerically. Firstly, the crystal formation will be neglected in the system. Also, heat transfer and the effective parameters will be considered for this case. In the following, it will be assumed that there will be crystal formation in the system and heat transfer will be determined for this case. Furthermore, the effect of crystal formation on the heat transfer will be discussed.

3.3.1 Crystallizer specifications and process conditions

In this study, the diameters of the crystallizer and the scraper blades are 10.4 cm and 2 cm respectively. The number of scraper blades is constant with four blades, and the rotational speed is varied between 50 rpm and 250 rpm. The crystallizer is filled with sodium chloride solution whose properties at the eutectic point are shown in Table 3.1.

Table3.1: Properties of sodium chloride solution at the eutectic point (Archer and Carter 2000a; Martínez et al., 2014).

Parameter	Amount	Unit
λ_s	0.48	$W \cdot m^{-1} \cdot K^{-1}$
ρ_s	1089.42	$kg \cdot m^{-3}$
μ_s	4.34	cp
c_{ps}	3.10	$J \cdot K^{-1} \cdot g^{-1}$

In this process, the heat transfer occurs between a coolant and the sodium chloride solution through the stainless steel bottom whose thermal conductivity is $1 W \cdot m^{-1} \cdot K^{-1}$.

The coolant, containing 50% ethylene glycol and 50% water, is used as circulating refrigerant to cool the bottom of the crystallizer. The coolant flows from the cooling machine to the bottom of the crystallizer through a tube. The diameter and length of the tube are 1 cm and 200 cm, respectively. The volumetric flow rates of coolant are applied between $10^{-5} \text{ m}^3\cdot\text{s}^{-1}$ and $10^{-2} \text{ m}^3\cdot\text{s}^{-1}$ and the inlet temperature is changed independently between $-30 \text{ }^\circ\text{C}$ and $-22 \text{ }^\circ\text{C}$.

Table 3.2: Physical properties of coolant at different inlet temperature (Engineering and Operating Guide 2008).

T(°C)	ρ_s (kg·m ⁻³)	μ_s (cp)	λ_s (W·m ⁻¹ ·K ⁻¹)	c_{ps} (J·K ⁻¹ ·g ⁻¹)
-30	1090.3	43.98	0.328	3.0888
-28	1089.86	37.982	0.3296	3.0966
-26	1089.42	32.792	0.3312	3.1044
-24	1088.98	28.41	0.3328	3.1122
-22	1088.54	24.836	0.3344	3.12
-20	1088.1	22.07	0.336	3.1278

In this case, the coolant outlet temperature, the crystallizer bottom surface temperature, and heat flux are dependent on other parameters such as the scraper rotational speed. The properties of coolant at a temperature between $-30 \text{ }^\circ\text{C}$ and -20°C are shown in Table 3.2.

3.3.2 Heat transfer modeling of sodium chloride solution system in the non-crystallizing condition

3.3.2.1 Scraper power consumption

The first step to compute power consumption is calculating the Newton number. In section 3, three kinds of scrapers were introduced that they are similar to the scraper of this study. In these equations, the amount of the Newton number can be changed based on the Reynolds number. On the other hand, the amount of Re can be varied by changing the rotational speed (Table 3.3).

Table 3.3: Variation of Re based on the rotational speed changes.

$N(\text{rpm})$	Re
50	5018.06
100	10036.11
150	15054.17
200	20072.22
250	25090.28

As shown in Table 3.3, if the rotational speed is applied between 50 rpm and 250 rpm, the Reynolds number will be varied between 5018.06 and 25090.28. Therefore, Equation 3.10, Equation 3.12, and Equation 3.15 can be used to calculate Ne for the flat-blade turbine, pitched-blade impeller, and marine-type propeller scrapers, respectively.

In Figure 3.15, the relations between the power consumption of the three mentioned scrapers and rotational speed are shown.

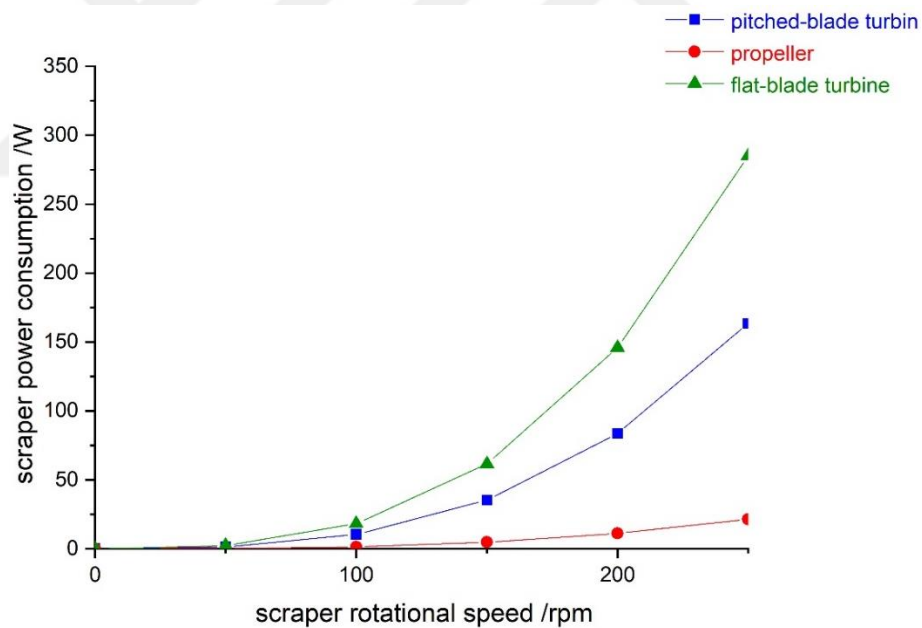


Figure 3.15: The scraper power consumption in non-crystallizing conditions as a function of rotational speed for (square) flat-blade turbine, (circle) pitched-blade impeller, (triangle) marine-type propeller.

According to Figure 3.15, the power consumption of flat-blade turbine and pitched-blade impeller are highly dependent on rotational speed and it is remarkably increased with increasing of the rotational speed. Even though in all three scrapers, the power consumption is calculated by Equation 3.7, despite the flat-blade turbine and pitched-

blade impeller the Newton number is constant, in the propeller, the Newton number is in inverse proportion to the Reynolds number which is a function of the scraper rotational speed. Therefore, in the propeller, the effect of rotational speed on power consumption is different from two others. The scraper of this is similar to the flat blade turbine stirrer and calculations will be based on this type of stirrer. In Figure 3.15, all operation conditions such as rotational speeds are the same except Ne . It can be concluded that P_s of a scraper is highly dependent on Ne . In other words, Ne is the only parameter to calculate P_s which is related to the scraper and independent of process. Therefore, the main parameter to determine efficiency of a scraper is Ne .

3.3.2.2 Heat transfer through a scraped surface

As mentioned in section 3.1, the overall heat transfer coefficient is a function of the coolant, the glass bottom, and the solution heat transfer coefficients. In the following, the numerical analysis of all three coefficient and also, the overall heat transfer coefficient will be considered.

Heat transfer through the bottom of the crystallizer

In this study, it is assumed that the wall of crystallizer is glass and its bottom is stainless steel whose thermal conductivity and thickness are $13.9\text{W}\cdot\text{m}^{-1}\cdot\text{K}^{-1}$ and 1mm, respectively. By using Equation 3.34, the conductive heat transfer will be:

$$\alpha_{bottom} = \frac{13.9}{0.003} = 4633.33 \text{ W}\cdot\text{m}^{-2}\cdot\text{K}^{-1}$$

Coolant heat transfer coefficient

The coolant heat transfer coefficient can be calculated by using Equation 3.26. In this equation, the Nusselt number is highly dependent on the flow regime. Therefore, at first, it is necessary to calculate Re and Pr . The Reynolds number and the Prandtl number can be calculated according to Equation 3.19 and Equation 3.22. Despite the Prandtl number which is the independent of the process conditions at the constant temperature, the Reynolds number is a function of the coolant velocity which can be defined as volumetric flow rate per the tube surface (Equation 3.20). Re changes in the various volumetric flow rates of the coolant. In Table 3.4 the relationship between \dot{V} , Re and Nu is shown.

Table 3.4: The relationship between the volumetric flow rate of coolant and the Reynolds number and Nusselt number.

$\dot{V}(\text{m}^3 \cdot \text{s}^{-1})$	Re	Nu
0	0	3.65
10^{-4}	1,157.49	14.53
$2 \cdot 10^{-4}$	2,314.98	18.75
$3 \cdot 10^{-4}$	3,472.47	82.20
$4 \cdot 10^{-4}$	4629.96	115.08
$8.5 \cdot 10^{-4}$	9,838.67	148.57
10^{-3}	11,574.9	169.20
10^{-2}	115,749	1067.57
1	11,574,905	42,500.90

In Table 3.4, Re is in the direct proportion to volumetric flow rate. According to Table 3.4, if volumetric flow rates are less than $2 \times 10^{-4} \text{ m}^3 \cdot \text{s}^{-1}$, the flow will be laminar and the Nusselt number can be calculated by using Equation 3.24. Also, if the volumetric flow rates range is between $2 \times 10^{-4} \text{ m}^3 \cdot \text{s}^{-1}$ and $8.5 \times 10^{-4} \text{ m}^3 \cdot \text{s}^{-1}$, the flow will be in the transition region, and the Nusselt number must be computed according to Equation 3.25. Furthermore, if the volumetric flow rates are higher than $8.5 \times 10^{-4} \text{ m}^3 \cdot \text{s}^{-1}$, the flow will be turbulent and the Nusselt number should be calculated by using Equation 3.23. As shown in Table 3.4, with increasing the volumetric flow rate, Reynolds number and consequently, the Nusselt number increases.

In Figure 3.16, the relation between the volumetric flow rate and coolant heat transfer coefficient is shown.

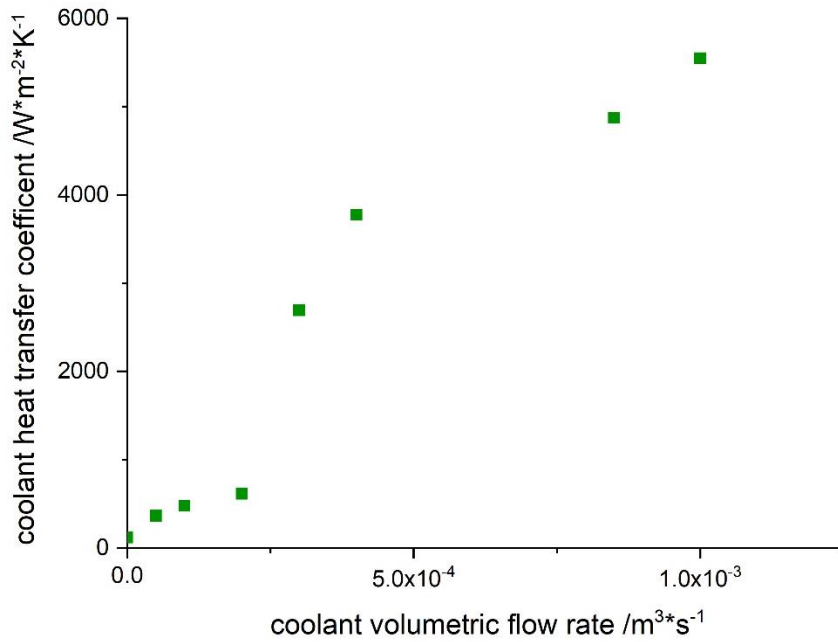


Figure 3.16: Relation between the volumetric flow rate and coolant heat transfer coefficient

The volumetric flow rate can affect remarkably on the heat transfer coefficient. Experimental researches in this field demonstrated that an increase of volumetric flow rate can be an effective way to enhance the convective heat transfer coefficient (Ahmad et al. 2017; Osueke et al., 2015). As shown in Figure 3.16, the results of this study can be proved by previous experimental studies. Also, the heat transfer coefficient increases with increasing volumetric flow rate. In Figure 3.16, in \dot{V} less than $2 \times 10^{-4} \text{ m}^3 \cdot \text{s}^{-1}$, the coolant flow is laminar and α_{cool} is maximum $1500 \text{ W} \cdot \text{m}^{-2} \cdot \text{K}^{-1}$. In \dot{V} ranges between $2 \times 10^{-4} \text{ m}^3 \cdot \text{s}^{-1}$ and $8.5 \times 10^{-4} \text{ m}^3 \cdot \text{s}^{-1}$, the flow is in the transition region. In the transition region, α_{cool} is remarkably higher than the laminar region and is about $3000 \text{ W} \cdot \text{m}^{-2} \cdot \text{K}^{-1}$. In \dot{V} higher than $8.5 \times 10^{-4} \text{ m}^3 \cdot \text{s}^{-1}$, the coolant flow is the turbulent and α_{cool} is minimum $4500 \text{ W} \cdot \text{m}^{-2} \cdot \text{K}^{-1}$ which is at least three times higher than laminar flow. According to Figure 3.16, in the higher volumetric flow rates, the turbulence of coolant is intenseness and α_{cool} is higher. As a result, in the turbulent region, heat transfer from the coolant to the crystallizer surface is significantly higher than laminar. Therefore, in this study, the minimum amount of \dot{V} to have proper heat transfer from the coolant is $8.5 \times 10^{-4} \text{ m}^3 \cdot \text{s}^{-1}$.

Solution heat transfer coefficient

In Figure 3.17, the relationship between rotational speed and solution heat transfer coefficient is shown.

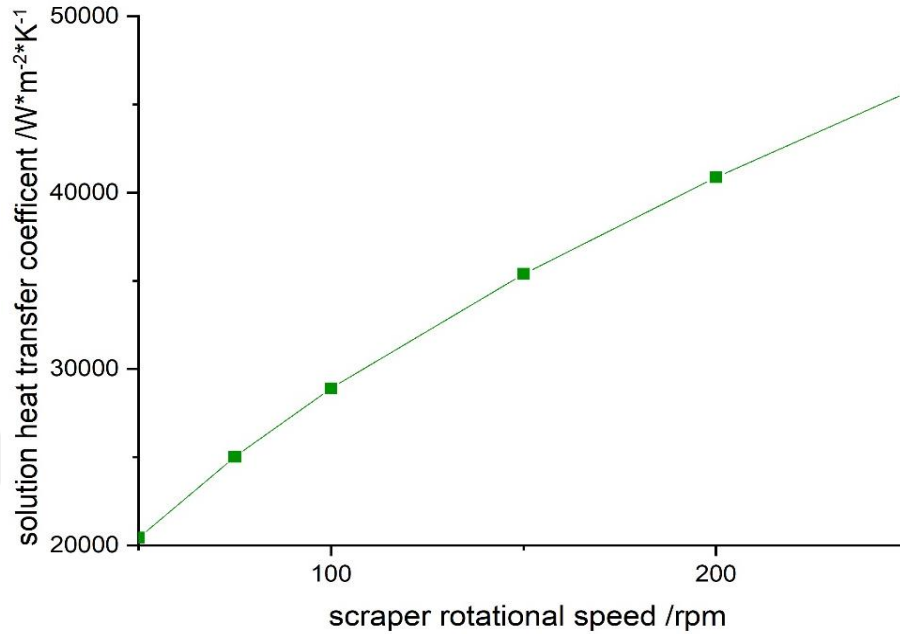


Figure 3.17: The relationship between rotational speed and solution heat transfer coefficient.

One of the main roles of the scraper in the crystallization process is the increase in the solution turbulence, because in the turbulent condition, the solution is mixed well and becomes more homogenous. Therefore, the high rotational speed can enhance the heat transfer coefficient. Furthermore, the scraper can prevent from ice layer formation on the cooled surface of crystallizer. The solution heat transfer coefficient as a function of rotational speed can be calculated by Equation 3.33. In Figure 3.17, the relation between the scraper rotational speed and the solution heat transfer coefficient is shown. According to this figure, with increasing the rotational speed, solution heat transfer coefficient will increase. As expected, the rotational speed has a positive effect on the solution heat transfer coefficient in the non-crystallizing condition. Figure 3.17 is drawn according to the penetration theory that the effect of solution viscosity is neglected. Therefore, it is expected that in the actual system, the solution heat transfer coefficient is affected by viscosity and it lower than theatrical amount which is shown in Figure 3.17.

Overall heat transfer coefficient

The overall heat transfer from the coolant to the solution can be calculated by Equation 3.18. The main terms in this equation are individual heat transfer coefficients which were considered numerically.

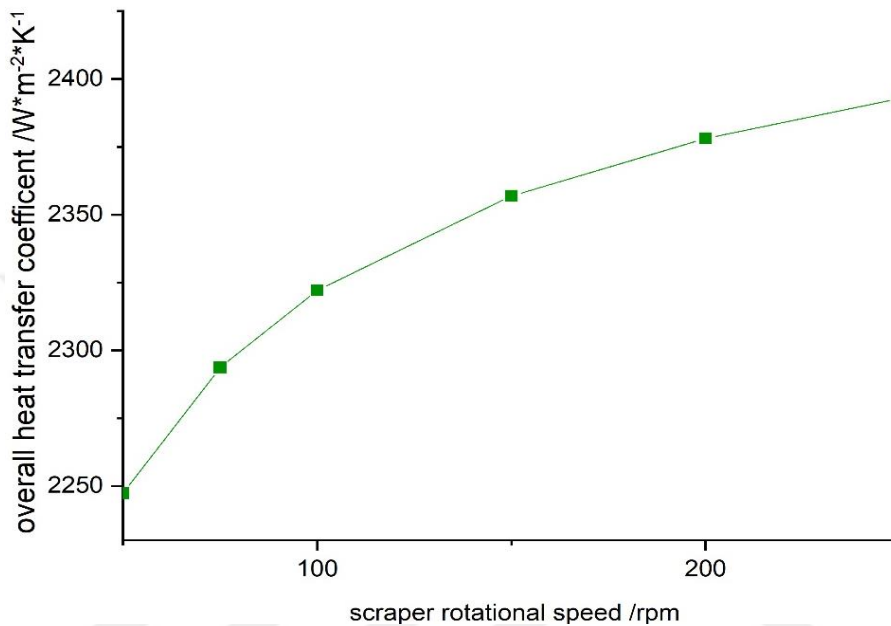


Figure 3.18: The effect of rotational speed on the overall heat transfer coefficient

Firstly, it is assumed that the coolant volumetric flow is constant at $10^{-3} \text{ m}^3\cdot\text{s}^{-1}$ and the scraper rotational speed is the only parameter to control the overall heat transfer coefficient. The scraper rotational speed affects the overall heat transfer coefficient by the solution heat transfer coefficient. In Figure 3.18, the relationship between the overall heat transfer coefficient and scraper rotational speed is shown. According to this figure, with increasing the rotational speed, the overall heat transfer coefficient is increased. However, the slope of the curve at higher rotational speeds is less. With increasing rotational speed, the solution is mixed well and its heat transfer coefficient increases. According to Equation 3.18, at higher amounts of the solution heat transfer coefficient, the coolant heat transfer and conductive heat transfer through the crystallizer bottom coefficients will dominate on the equation and the effect of solution heat transfer coefficient and the rotational speed will decrease. On the other hand, at the rotational speed between 50 rpm and 250 rpm, the overall heat transfer coefficient increases about 6% which is negligible. Therefore, although the scraper must mix the

solution homogeneously and make it turbulent, the effect of the higher scraper rotational speed on the overall heat transfer coefficient is negligible. As a result, according to the slope of curve in Figure 3.18, in the non-crystallizing condition, the optimum amounts of N is between 50 rpm and 150 rpm.

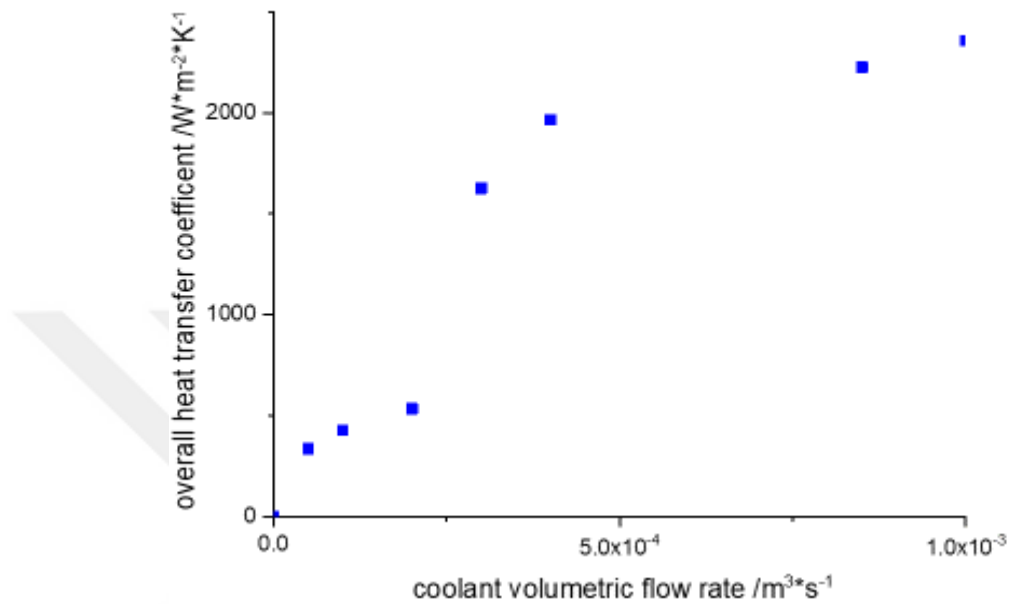


Figure 3.19: The overall heat transfer coefficient as a function of coolant volumetric flow rate

If it is assumed that the amount of the scraper rotational speed and is constant at 150 rpm the only parameter to control heat transfer coefficient will volumetric flow rate. In Figure 3.19, the overall heat transfer coefficient as a function of the coolant volumetric flow rate is shown. The coolant flow rate affects the overall heat transfer coefficient. According Figure 3.19, with increasing the coolant volumetric flow rate, the overall heat transfer coefficient increases. However, the rates of increase are not the same in different flow regimes. The overall heat transfer coefficient in the turbulent coolant flow is by approximately four times higher than laminar flow, because in turbulent flow in addition to the conductive heat transfer, there is convective heat transfer which is not in laminar flow. On the other hand, in turbulent region, the increase of the coolant flow rate does not have significant effect on the overall heat transfer coefficient. According to Equation 3.18, if the coolant heat transfer coefficient is a high amount, other terms will dominate the equation and have more effect on the overall heat transfer coefficient. Therefore, in this study, the optimum range for the

coolant volumetric flow rate is $8.5 \cdot 10^{-4} \text{ m}^3 \cdot \text{s}^{-1}$ and $10^{-3} \text{ m}^3 \cdot \text{s}^{-1}$, because, this range is in turbulent region and also is not too much that can not impact on the overall heat transfer coefficient.

The coolant outlet temperature, the heat flux, and the crystallizer inner bottom temperature

The outlet temperature of coolant, the heat flux from the coolant to the solution and the temperature of crystallizer inner bottom surface are dependent variables which can be controlled by the scraper rotational speed, the coolant volumetric flow rate and the inlet temperature of coolant which can be applied as independent parameters.

The heat flux can be calculated by Equation 3.16 and Equation 3.34. According to the heat balance on the cooled surface of crystallizer, the relationship between independent parameters and outlet temperature can be described by a combination of Equation 3.17 and Equation 3.34:

$$\ln \frac{T_{out} - T_{EUT}}{T_{in} - T_{EUT}} = \frac{U_{overall} A_{cryst}}{\dot{V} \rho_c c_{pc}} \quad 3.64$$

Under steady state conditions, the heat flow rate is the same. As a result, the heat flux from the crystallizer inner bottom surface at T_b to the solution at T_{EUT} is equal to \dot{Q}_{cool} . In Equation 3.65, by inserting \dot{Q}_{cool} which is calculated according to Equation 3.16, T_b can be computed.

$$\dot{Q}_{cool} = \alpha_s A_{cryst} (T_{EUT} - T_b) \quad 3.65$$

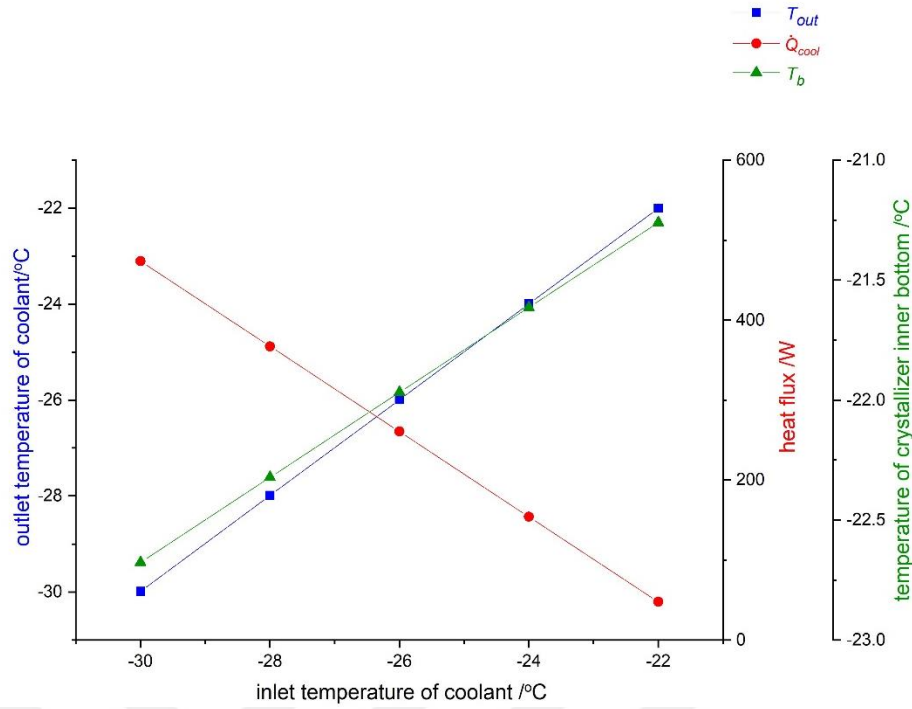


Figure 3.20: The coolant outlet temperature (square), the heat flux from the coolant to the solution (circle) and the temperature of crystallizer inner surface (triangle) as a function of coolant inlet temperature.

At first, it is assumed that scraper rotational speed and coolant volumetric flow rate are constant and their amounts are 200 rpm and $10^{-4} \text{ m}^3 \cdot \text{s}^{-1}$. Therefore, the coolant inlet temperature can be considered as a variable parameter in the process. In this condition, due to the physical properties of coolant are dependent on the temperature, by changing coolant inlet temperature, they will be changed. In Table 3.2, The physical properties of coolant at the different average temperature are shown. The effect of T_{in} on T_{out} , \dot{Q}_{cool} and T_b can be considered by Equation 3.64, Equation 3.65 and Equation 3.16.

In Figure 3.20, the outlet temperature is shown as a function of inlet temperature by square points. According Figure 3.20, the relationship between inlet and outlet temperature of the coolant is linear. This result can be demonstrated by Equation 3.64 if it is rewritten as:

$$T_{out} = mT_{in} + (1 - m)T_{EUT} \quad 3.66$$

$$b = e \frac{U_{overall} A_{cryst}}{V \rho_c c_{pc}} \quad 3.67$$

In Equation 3.66, b which represents ratio of the difference between coolant outlet temperature and the eutectic temperature to the difference between coolant inlet

temperature and the eutectic temperature, will be constant if it is assumed that the physical properties changes in the different inlet and outlet average temperature are negligible. Also, due to the solution temperature is constant at the eutectic temperature, the outlet temperature will be a function of only the coolant inlet temperature and the relationship between them will be linear.

In Figure 3.20, the heat flux from the coolant to the solution is shown as a function of inlet temperature by circle points. According to this figure, the heat flux and the coolant inlet temperature are in an inverse proportion, and their relation is linear. In Figure 3.20, the coolant volumetric flow rate and the scraper rotational speed are constant and the physical properties changes in different inlet and outlet average temperature are negligible. To consider the relationship between the heat flux and coolant inlet temperature can be explained according to Equation 3.35. In this equation, the difference between the outlet and the inlet temperature of coolant can control the heat flux from the coolant to the solution. In this study, to illustrate the effect of coolant inlet temperature, Equation 3.66 can be written as:

$$\Delta T = (b - 1)(T_{in} - T_{EUT}) \quad 3.68$$

In Equation 3.68, ΔT is the difference between the inlet and outlet temperature of the coolant. According to Equation 3.68, with increasing the difference between the inlet temperature of the coolant and the solution temperature which is eutectic temperature, the difference between inlet and outlet temperature of the coolant will be increased. As a result, if the inlet temperature increases, the heat flux from the solution to the coolant will decrease. According to Figure 3.20, due to the difference between T_{in} and T_{out} decreases about 80% at T_{in} between -30°C and -22°C , according to eq Equation 3.35, \dot{Q}_{cool} also decreases by approximately 80%.

In Figure3.20, the crystallizer bottom inner surface temperature is shown as a function of coolant inlet temperature by triangle points. According to Figure 3.20 the relation between T_{in} and T_b is linear. In T_{in} between -22 and -30 $^{\circ}\text{C}$, T_b is changed by approximately 6% which is a few amount. This result can be demonstrated by Equation 3.65. In Equation 3.65, the only variable which can control T_b is \dot{Q}_{cool} and other parameters such as solution heat transfer coefficient are constant. As a result, the temperature difference between solution and the inner bottom surface of the crystallizer decreases at T_{in} between -30°C and -22°C about 80% . As a result, with

increasing T_{in} , the difference between T_{EUT} and T_b gets low and T_b is approached to the eutectic temperature.

The second parameter which can be considered as an independent variable is \dot{V} . Therefore, if it is assumed that N and T_{in} are constant and their amounts are 150 rpm and -30°C , respectively, T_{out} , \dot{Q} and T_b can be shown as a function of \dot{V} .

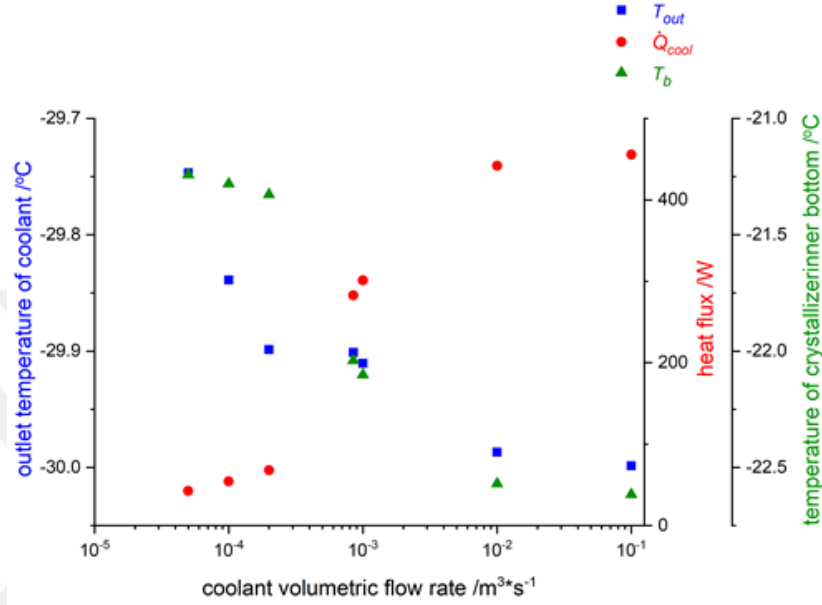


Figure 3.21: The coolant outlet temperature, the heat flux from coolant to the solution and temperature of crystallizer inner surface as a function of coolant volumetric flow rate

In Figure 3.21, T_{out} is displayed as a function of \dot{V} by square points. To demonstrate the relationship between \dot{V} and T_{out} , Equation 3.64 can be written as:

$$T_{out} = (T_{in} - T_{EUT})e^{\frac{U_{overall} A_{cryst}}{\dot{V} \rho_c c_{pc}}} + T_{EUT} \quad 3.69$$

According to Equation 3.69, T_{out} is an exponential function of \dot{V} . In Equation 3.69, T_{out} can be varied by different amounts of \dot{V} and also $U_{overall}$ which is a function of \dot{V} . However, based on Figure 3.21, T_{out} is not changed exponentially as a function of \dot{V} . This result is referred to different behavior of overall heat transfer coefficient in the turbulent and laminar coolant flow regimes. In the laminar region, although with increasing \dot{V} , $U_{overall}$ increases, however, the changes of $U_{overall}$ is more than \dot{V} and $U_{overall}$ dominates on the power of e . Thus, due to difference between T_{in} and T_{EUT} is negative, in the laminar region with increasing of \dot{V} , T_{out} decreases exponentially. In the higher amounts of \dot{V} that flow is turbulent, $U_{overall}$ is constant and independent

of \dot{V} . Therefore, according to Equation 3.69, at higher amounts of \dot{V} , the power of constant e tends to zero and T_{out} is approached to T_{in} .

In Figure 3.21, \dot{Q} is shown as a function of \dot{V} by circle points. \dot{V} is inversely proportional to the difference between T_{in} and T_{out} . On the other hand, according to Equation 3.35, \dot{Q}_{cool} is a function of ΔT and \dot{V} . The relation between \dot{Q}_{cool} and \dot{V} is nonlinear, because, in Equation 3.35, T_{out} is an exponential function of \dot{V} which is an independent variable. Therefore, the relation between \dot{Q}_{cool} and \dot{V} is neither linear nor exponential. As a result, in the laminar region where amounts of \dot{V} is less, T_{out} dominates on Equation 3.16 and \dot{Q}_{cool} will be an exponential function of \dot{V} and in the higher amounts of \dot{V} in the turbulent region, the difference between T_{out} and T_{in} is a very low amount and \dot{V} dominates on this equation and the relation between \dot{Q}_{cool} and \dot{V} is linear.

In Figure 3.21, T_b is shown as a function of \dot{V} by triangle points. In Figure 3.21, \dot{V} is the reverse proportion of T_b and their relation is nonlinear. This result can be demonstrated by Equation 3.65 and due to T_b is a function of \dot{Q}_{cool} , its behavior in a less and higher amount of \dot{V} is similar to \dot{Q}_{cool} . Thus, in the laminar coolant flow T_b is an exponential function of \dot{V} and in the turbulent region, the relation between them is linear. Furthermore, due to the sign of T_b is negative in Equation 3.65, T_b and \dot{V} are inversely proportional.

The rotational speed is another parameter which can be considered as an independent variable. In this regard, if it is assumed that T_{in} and \dot{V} are constant, and their amounts are -30°C and $10^{-2} \text{ m}^3 \cdot \text{s}^{-1}$, respectively, the effect of N in the ranges between 50 and 200 rpm on the dependent variables such as T_{out} can be considered.

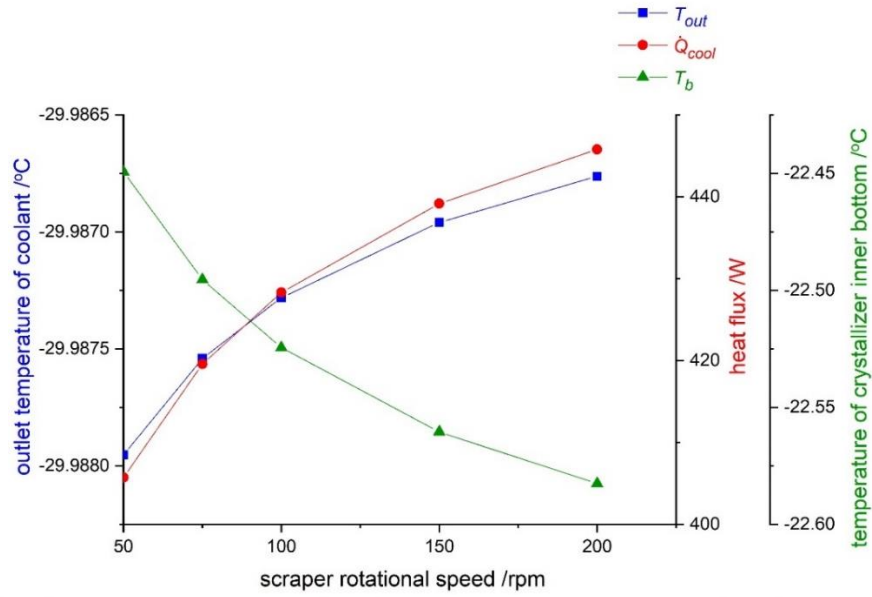


Figure 3.22: The coolant outlet temperature, the heat flux from coolant to the solution and temperature of crystallizer inner surface as a function of the scraper rotational speed.

In Figure 3.22, T_{out} is shown as a function of N by square points. The effect of N on T_{out} is very low, and changes of T_{out} over N between 50 and 200 rpm is by approximately 0.004%. According to Equation 3.64, the only independent variable to control T_{out} as a function of N is $U_{overall}$. According to Figure 3.67, N has more effect on $U_{overall}$ only in the less rotational speeds of scraper and due to T_{out} is an exponential function of $U_{overall}$, N affects T_{out} very low.

The other controllable parameter which can be considered as a function of N is \dot{Q}_{cool} . Due to \dot{Q}_{cool} is a function of T_{out} , if T_{in} and \dot{V} are constant, the effect of N on \dot{Q}_{cool} is similar to the effect of N on T_{out} . In Figure 3.22, \dot{Q}_{cool} is shown as a function of N by triangle points. In Figure 3.22, due to N affects T_{out} in the lower rotational speeds like 50 to 100 rpm is higher, the slope of the figure in this range is steep.

In Figure 3.22, T_b is shown as a function of N . this relation can be demonstrated by Equation 3.65. In this equation, \dot{Q}_{cool} and $\alpha_{solution}$ which are a function of N , can control T_b . N is directly proportional to both of \dot{Q}_{cool} and α_s . However, at N between 50 rpm and 200 rpm, α_s is changed by approximately 100%, while \dot{Q}_{cool} is changed about 9% which can be neglected. Therefore, α_s dominates on Equation 3.65 and can control T_b . As a result, with increasing N , α_s increases and T_b increases and approached to T_{EUT} .

As mentioned above, in this chapter, the dependent variables were considered as a function of independent variables in steady state conditions. Therefore, according to the heat balance, the difference between \dot{Q}_{cool} and P_s must be zero. In Table 3.5, process conditions which obeyed heat balance, are chose. According Table 3.5, if it is assumed that the scraper of study is similar to the flat blade turbine, the power consumption and heat flux from the coolant to the solution will be corresponded with each other and in other conditions which heat balance is ignored results are not acceptable. Even though, in these two conditions \dot{Q}_{cool} and P_s are similar to each other, their difference are not zero that it can be referred to the errors which are related to the assumptions for simplifying calculations.

Table 3.5: Process conditions which obey heat balance in the steady state.

T_{in} (°C)	\dot{V} (m ³ ·s ⁻¹)	N (rpm)	P_s (W)	\dot{Q} (W)	<i>Error</i> %
-30	0.0002	150	61.55	68	8.8

3.3.3 Heat balance under unsteady state condition

In this section, heat transfer at the unsteady state of solution temperature will be considered. Therefore, according to Equation 3.36, the initial temperature of the solution as the previous part is not on the eutectic temperature and the difference between \dot{Q}_{cool} and P_s which is known as \dot{Q}_{Feed} will be consumed to cool down the temperature of the solution to the eutectic temperature which is -21.1°C. Based on Equation 3.40, the cooling rate of solution can be varied by different amounts of $U_{overall}$ and P_s . In this section, the time required to cool down the 1 kg solution with an initial temperature of 20 °C in different process conditions will be considered. Furthermore, it is assumed that the changes of solution physical properties over the cooling process are neglected.

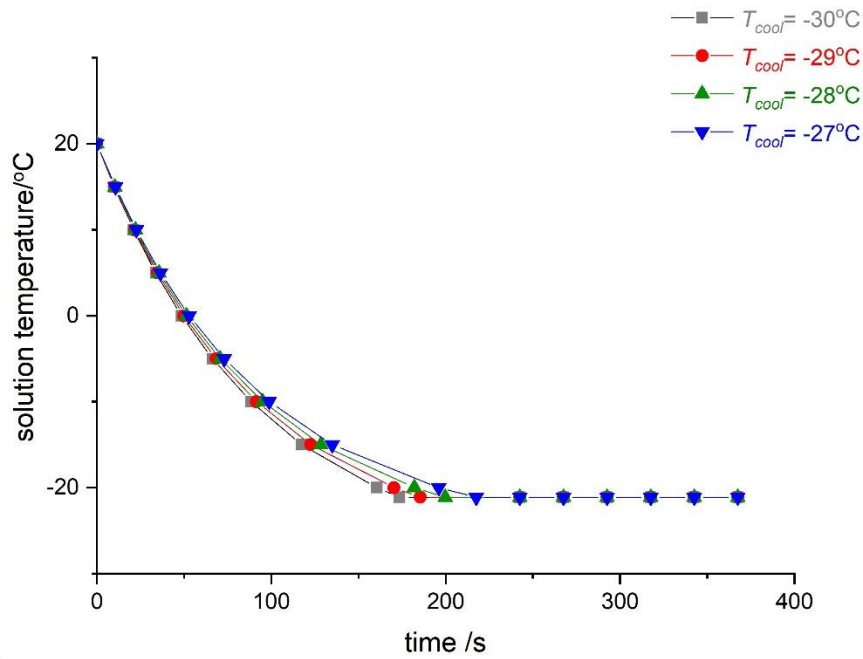


Figure 3.23: The solution temperature as a function of time at the various coolant temperature.

At first, it is assumed that \dot{V} and N are constant and their amounts are $10^{-2} \text{ m}^3 \cdot \text{s}^{-1}$ and 150 rpm, respectively. Thus, $U_{overall}$ and P_s are constant and T_{cool} is the only independent variable which can control the cooling rate of the solution. In Figure 3.23, T_{cool} is shown as a function of time in various amounts of T_{cool} . In this figure, the solution temperature decreases exponentially as a function of T_{cool} over the time, at the coolant temperature between -30°C and -27°C . The times required to cool down the solution from 20°C to -21.1°C , at the coolant temperature of -30°C , -29°C , -28°C and -27°C are 160s, 170s, 182s and 196s, respectively. As a result, with increasing the coolant temperature, the time require to cool down the solution increases. This result can be referred to the effect of coolant temperature on the heat flux from the coolant to the solution. At the less solution temperature, the temperature difference between coolant and solution and consequently heat flux are higher and the solution needs less time to cool until the eutectic temperature. Furthermore, this result can be demonstrated by Equation 3.39. According to this equation, due to $U_{overall}$ and P_s are constant, with decreasing T_{cool} , the difference between coolant and solution temperature becomes higher and cooling rate increases and the solution needs less time to achieve the eutectic point.

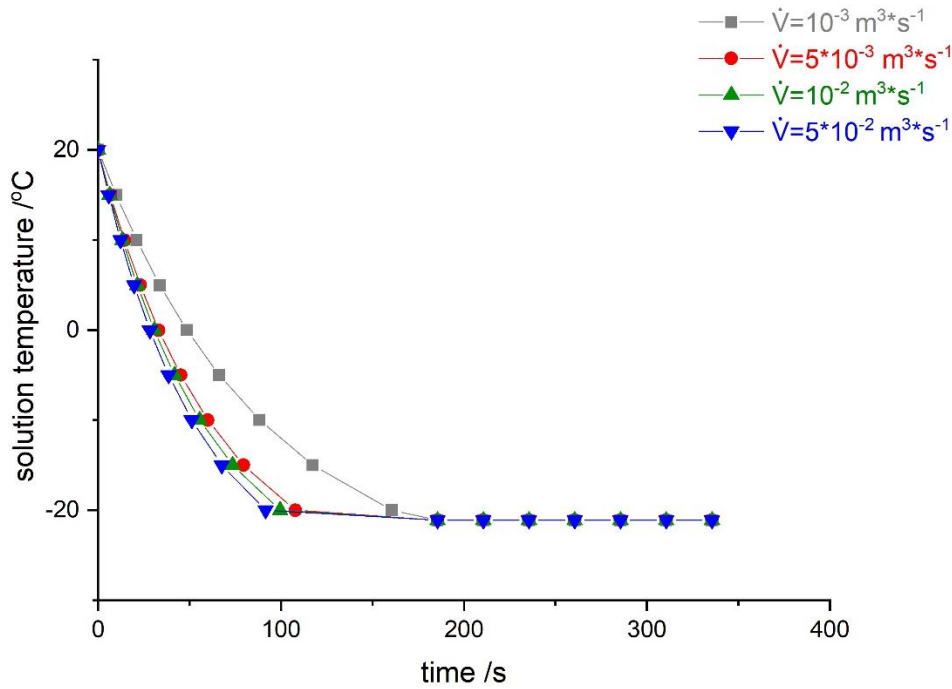


Figure 3.24: The solution temperature as a function of coolant volumetric flow rates over time.

The other independent parameter which can impact on the cooling rate of the solution is \dot{V} . According to Equation 3.40, $U_{overall}$ is the only parameter which is a function of \dot{V} . $U_{overall}$ is directly proportional to \dot{V} . Therefore, according to Equation 3.39, due to P_s is constant, with increasing \dot{V} , $U_{overall}$ and consequently the cooling rate of solution increases. In Figure 3.24, the solution temperature is shown as a function of \dot{V} over time. Also, N and T_{cool} are constant and their amounts are 150 rpm and -30°C , respectively. The times required to decrease T_{sol} until T_{EUT} with the volumetric flow rates of $10^{-3} \text{ m}^3\cdot\text{s}^{-1}$, $5 \times 10^{-3} \text{ m}^3\cdot\text{s}^{-1}$, $10^{-2} \text{ m}^3\cdot\text{s}^{-1}$ and $5 \times 10^{-2} \text{ m}^3\cdot\text{s}^{-1}$ are 160s, 108s, 99s and 91s, respectively. According to Figure 3.24, with increasing \dot{V} , the cooling rate is increased. However, in the higher amounts of \dot{V} , the cooling rates are similar and their difference are not remarkable. This result can be demonstrated by the relation between \dot{V} and $U_{overall}$. As mentioned above, in the higher amounts of \dot{V} , changes of $U_{overall}$ as a function of \dot{V} is less. As a result, the higher amounts of \dot{V} has less effect on the solution cooling rate.

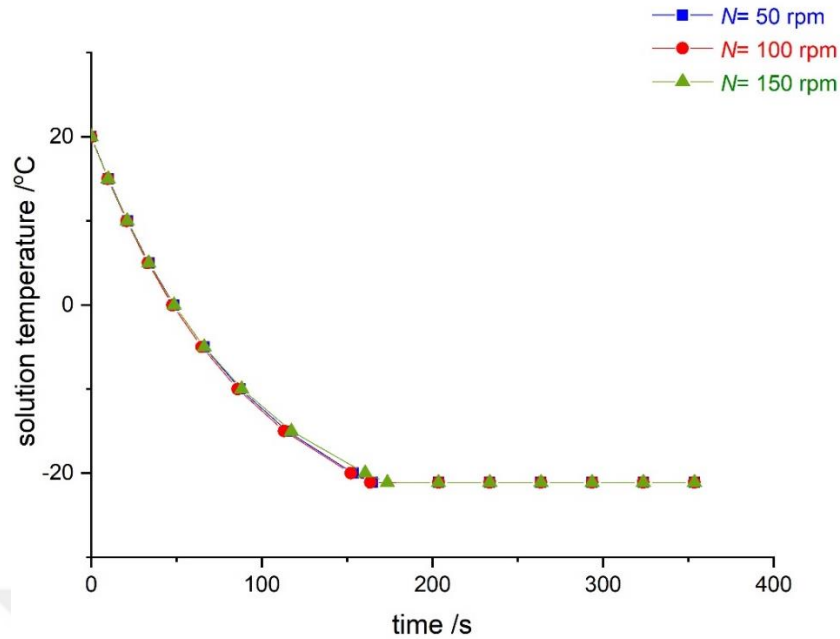


Figure 3.25: The solution temperature as a function of time in different amounts of stirrer rotational speed.

Another independent parameter which can impact on the cooling rate by controlling both $U_{overall}$ and P_s is N . Even though $U_{overall}$ and P_s are in direct proportion with N , the relation between N and the cooling rate is complicated and must be considered. In Figure 3.25, the solution temperature versus required time to cool down the solution is shown. In Figure 3.25, it is assumed that T_{cool} and \dot{V} are constant and their amounts are $-30\text{ }^\circ\text{C}$ and $10^{-2}\text{ m}^3\cdot\text{s}^{-1}$, respectively, and N is the only independent variable and changes between 50 rpm and 150 rpm. The required t to cool down the solution until T_{EUT} with the scraper rotational speed of 50 rpm, 100 rpm and 150 rpm are calculated 153 s, 152 s and 161 s, respectively. According to these results, with increasing N between 50 rpm and 100 rpm the cooling rate of solution increases and the solution needs less time to cool until the eutectic temperature and at N between 100 rpm and 150 rpm, the cooling rate of the solution decreases. According to Equation 3.40, the cooling rate is in a direct relation with $U_{overall}$ and an inverse relationship with P_s . Therefore, at N ranges between 50 rpm and 100 rpm, $U_{overall}$ dominates Equation 3.10 and increase of rotational speed increases the cooling rate. On the other hand, at N between 100 rpm and 150 rpm P_s dominates on Equation 3.40 and is inversely proportional to cooling rate of the solution and the time required to cool down the solution increases. As a result, the optimum amounts of N to cool down the solution is 100 rpm.

3.3.4 Heat transfer modeling of sodium chloride solution system in the crystallizing condition

In the previous section, the EFC process was considered in non-crystallizing condition for both steady and unsteady state of the solution. In this section, it is assumed that the solution is at EP and the crystallization process occurs and according to the qualitative analysis of Section 3.2, the heat transfer in a batch crystallizer for EFC process will be considered numerically.

3.3.4.1 Effect of crystal formation on the solution physical properties

As mentioned in the previous section, the crystal particles impact on the physical properties of the solution and consequently on the overall heat transfer coefficient and heat flux from the coolant to the solution and the related equations are stated. In this section, the effect of the ice mass fraction on the mentioned parameters in the previous section will be considered.

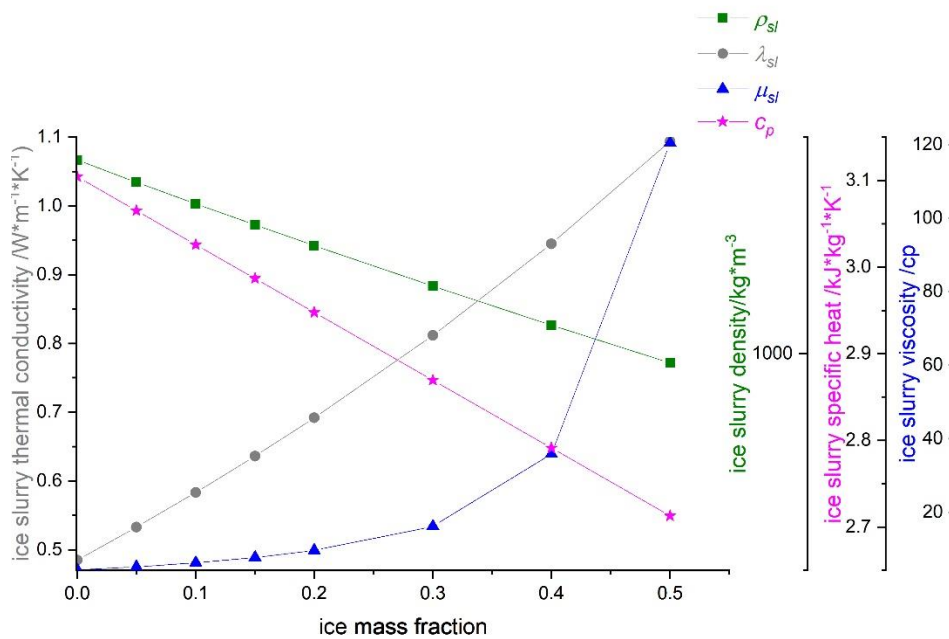


Figure 3.26: Density, thermal conductivity, specific heat and viscosity of slurry as a function of ice mass fraction.

In Figure 3.26, the density of ice slurry as a function of the ice mass fraction is shown by square points. According Figure 3.26, with increasing the mass fraction of ice crystals, the density of the slurry is decreased linearly. This result can be demonstrated by Equation 3.43. In the right side of this equation, the first term is related to the ice

properties and the second term is related to the solution. In the fewer amounts of ice mass fraction, the second term dominates, and the slurry density is approached to the solution density which is higher than the ice crystal density, and in the higher amounts of the mass fraction the first term dominates and density of slurry tends to the density of the ice crystal and decreases. According to Figure 3.26, the density of slurry decreases by approximately 8% in the ice mass fraction between 0 and 0.5. Furthermore, this result corresponds with a similar study which approves the reverse proportion relationship between ice mass fraction and slurry density (Kauffeld et al., 2010).

The other properties of the solution which are influenced by the crystal particles are thermal conductivity. According to several studies, the thermal conductivity is highly dependent on the mass fraction of ice crystal in the slurry and the directly proportional to ice particles. Furthermore, according to Maxwell's model which is shown by Equation 3.463, the effective thermal conductivity of slurries which contain solid particle increases with the volume fraction of these particles (Shin and Lee, 2000; Choi and Eastman, 1995). As shown in Figure 3.26, with increasing mass fraction of ice crystals in the solution, the thermal conductivity of the slurry increases by approximately 125% in the non-crystallizing and crystallizing condition with ice mass fraction of 0.5. Thermal conductivity of solids higher than liquids, because, despite the molecular structure of solids has high degree of crystallinity which has significant effect on the thermal conductivity, the molecular structure of liquid is disordered (Ross et al., 1984). According to Equation 3.46, in the fewer amounts of ice fraction, the thermal conductivity of ice slurry is approached to the solution thermal conductivity which is lower than ice. On the other hand with increasing the ice fraction the solid particle fraction increases and thermal conductivity of slurry is tended to ice thermal conductivity and highly increases.

The specific heat is a strongly temperature-dependent parameter. However, in this study, due to the temperature of the solution is constant at the eutectic temperature, the only effect of crystal mass fraction is considered (Zeng et al., 2009). According to the several studies, the mass fraction of ice crystals and specific heat of the solution are in reverse proportion, and with increasing the ice mass fraction in the slurry the specific heat of slurry decreases (Inaba et al., 2004; Yamagishi et al., 1999; Meewisse and Infante Ferreira, 2003). In Figure 3.22, based on the Equation 3.48, the specific heat

of slurry as a function of ice mass fraction is shown. According to this figure, in the ice mass fraction between 0 and 0.5, the specific heat of the solution decreases by approximately 12% which corresponds with the result of Meewisse and Ferreira (Meewisse and Infante Ferreira, 2003). This result can be explained based on molecular heat transfer. The structure of solids is ordered and molecules are closer than molecule of liquids. Therefore, solids conduct heat better than liquids. In this study, with increasing ice mass fraction, the liquid solution tends to be solid and the specific of slurry decreases.

The viscosity highly depends on the ice mass fraction, and with increasing the mass fraction of ice in the solution, the viscosity remarkably increases (Senapati et al. 2010; Aktaş and Woodburn 2000). According to Equation 3.51, in Figure 3.26, the viscosity of the slurry is shown versus the ice mass fraction in the slurry. According to Figure 3.26, with increasing of ice mass fraction between 0 and 0.5, the viscosity of the slurry is changed by approximately 2673% which is the remarkable amount that it corresponds with the study of Meewisse and Ferreira (Meewisse and Infante Ferreira, 2003). This result can also be explained by Equation 3.50. In this equation, the slurry density is an exponential function of ice mass fraction, and in the high amounts of ice mass fraction the viscosity of the solution is increased remarkably and approached to the viscosity of ice which is a high amount.

3.3.4.2 Effect of crystal formation on Re , α_{sl} and $U'_{overall}$

Re for an ice slurry can be calculated by Equation 3.53. In this equation, the variables which are a function of ice mass fraction, are ρ_{sl} and μ_{sl} . The ice mass fraction is inversely proportional to ρ_{sl} and directly proportional to μ_{sl} . Therefore, it is expected that with increasing the ice mass fraction, Re is sharply decreases.

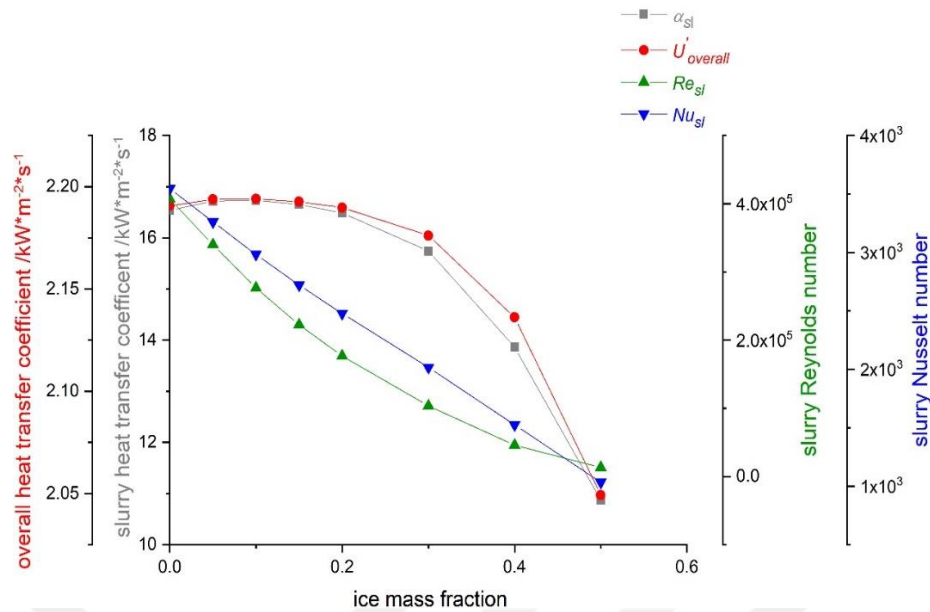


Figure 3.27: Reynolds number, Nusselt number, heat transfer coefficient of slurry and overall heat transfer coefficient as a function of ice mass fraction.

In the Figure 3.27, Re is shown as a function of the ice mass fraction in the slurry by triangle points. With increasing the ice mass fraction between 0 and 0.5, Re of the solution decreases by approximately 96% which is a notable amount. The reduction of Re is mainly referred to the exponential increase of the viscosity of the ice slurry as the highly increase of the ice fraction (Bellas et al., 2002). A proper agreement is observed between this result and Senapati's study. In both studies, Re highly decreases with increasing the slurry ice mass fraction (Senapati et al., 2010).

In Figure 3.27, Nu is shown versus the ice mass fraction of slurry by inverse triangle points. According to Figure 3.27, in the ice fraction between 0 and 0.5, Nu decreases by approximately about 70%. The results of this study correspond with Petukhov correlation and experimental researches which deduced increase of solid particles mass fraction decreases Nu remarkably (Knodel et al., 2000). Nu is calculated by Equation 3.55. In Equation 3.55, due to Re is much higher than Pr and dominates on the equation, Re determine the behavior of Nu as a function of the ice mass fraction. According to Equation 3.55, Nu is almost square root function of Re . On the other hand, Re decreases exponentially as a function of the ice mass fraction. As a result, Nu decreases almost linearly as a function of the ice mass fraction.

In Figure 3.27, α_{sl} is shown as a function of slurry ice mass fraction by square points. According to Equation 3.56, due to the diameter of the crystallizer is constant, α_{sl} is a

function of the Nu and λ_{sl} . The ice mass fraction is in direct relation to λ_{sl} and inversely proportional to Nu_{sl} . According to Figure 3.27, the slurry heat transfer coefficient increases by approximately 1.2% in the mass fraction range between 0 and 0.1 and then it decreases about 36% in the mass fraction range between 0.1 and 0.5. This result can be demonstrated by Equation 3.56, in the mass fraction range 0 and 0.1, the equation is dominated by λ_{sl} and with increasing the ice mass fraction, α_{sl} is increased. However, in the mass fraction range between 0.1 and 0.5, the effect of Nu on α_{sl} is more than λ_{sl} and with increasing ice mass fraction α_{sl} decreases as Nu decreases remarkably. However, according to other studies, if α_{sl} is calculated by Equation 3.54 which is considered based on penetration theory and effect of viscosity changes over the mass production in the slurry is neglected, α_{sl} will be in direct relationship with the ice mass fraction and with increasing the ice mass fraction, α_{sl} will increase (Qin et al. 2006). On the other hand, this result corresponds to the experimental research of Mouneer to who deduced the overall heat transfer coefficient slightly increases then decreases with increasing of ice production (Mouneer et al., 2010)

If it is assumed that the coolant and crystallizer bottom properties are constant, the effect of ice particles on the overall heat transfer coefficient can be considered. According to Equation 3.57, $U'_{overall}$ is directly proportional to α_{sl} . Therefore, it is expected that $U'_{overall}$ will change as a function of ice mass fraction like α_{sl} . In Figure 3.27, $U'_{overall}$ is shown versus the ice mass fraction by circle points. In Figure 3.27, $U'_{overall}$ increases in the ice mass fraction range between 0 and 0.1 by approximately 0.068% and then, it decreases in the ice mass fraction range between 0.1 and 0.5 about 2.9% which is not a remarkable amount. This result corresponds to an experimental studies which shows the overall heat transfer coefficient is independent of ice mass fraction and production of ice cannot have a notable effect on it (Fernández-Seara and Diz, 2014).

3.3.4.3 Effect of crystal formation on \dot{Q} , P_s and H_f

In Figure 4.20, \dot{Q} is shown versus the ice mass fraction by square points.

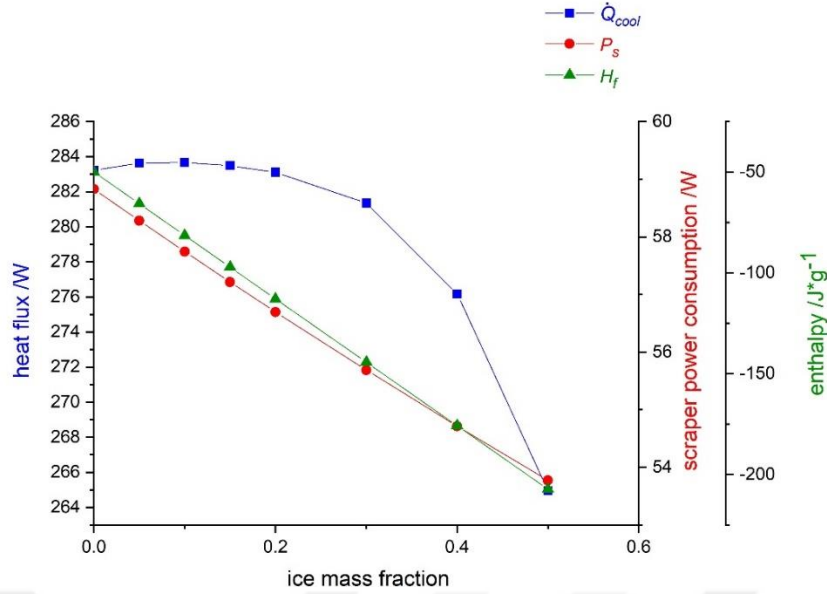


Figure 3.28: The heat flux, scraper power consumption and enthalpy of slurry as a function the ice mass fraction.

According to Figure 3.28 in the ice mass fraction between 0 and 0.1, \dot{Q} increases slightly and it decreases by approximately 2.9% in the ice mass fraction between 0.1 and 0.5 that it is not a remarkable amount and can be neglected. Based on Equation 3.16, if the surface area and temperature difference between solution and coolant is constant, \dot{Q} will be changed as a function of the overall heat transfer coefficient. $U'_{overall}$ is almost independent of the ice mass fraction. Therefore, ice generation cannot affect remarkably \dot{Q} .

According to Equation 3.52, with appearing ice crystal on a solution, the only variable to calculate scraper power consumption which is influenced by the ice mass fraction is the solution density. Although, Ne can be changed by Re which is a function of the viscosity of the solution plus to the density ,however, in this study, according to the type of scraper, Ne is constant and independence of Re (Rao and Hartel, 2006). In Figure 3.28, the scraper power consumption is shown as a function of the ice mass fraction in the slurry. In Figure 3.28, with increasing the ice mass fraction between 0 and 0.5, P_{sl} decreases about 8%. This result can be demonstrated by the effect of ice mass fraction on the slurry density. In ice mass fraction between 0 and 0.5 the density of slurry decreases about 8%. Due to the density and power consumption are directly proportional and N , d_r and Ne are constant, the scraper power consumption decreases by approximately 8% in ice mass fraction between 0 and 0.5. This amount is not a remarkable and can be neglected.

The heat of crystallization is a function of crystal production rate, fusion enthalpy of the ice and solution. There is a good agreement in the several studies that slurry enthalpy and the ice mass fraction are inversely proportional (Guilpart et al., 2006; Melinder, 2010). In Figure 3.28, the slurry enthalpy is shown as a function of the ice mass fraction by gray plot. In Figure 3.28, the amount of slurry enthalpy decreases remarkably about 300% in the ice mass fraction range between 0 and 0.5. According to Equation 3.60 the slurry enthalpy and the ice mass fraction are inversely related. Due to the disordered structure of liquids in comparison to the solids, the enthalpy of liquid is higher than enthalpy of solid. Therefore, with increasing the ice mass fraction, the liquid solution tends to be solid and its enthalpy decreases.

3.3.4.4 Effect of coolant temperature, coolant volumetric flow rate and scraper rotational speed on ice production

The effect of ice mass fraction in the slurry on the heat flux and scraper power consumption is a few amount. Therefore, it is assumed that the heat flux and the scraper power consumption are constant over the ice mass fraction increase in the slurry.

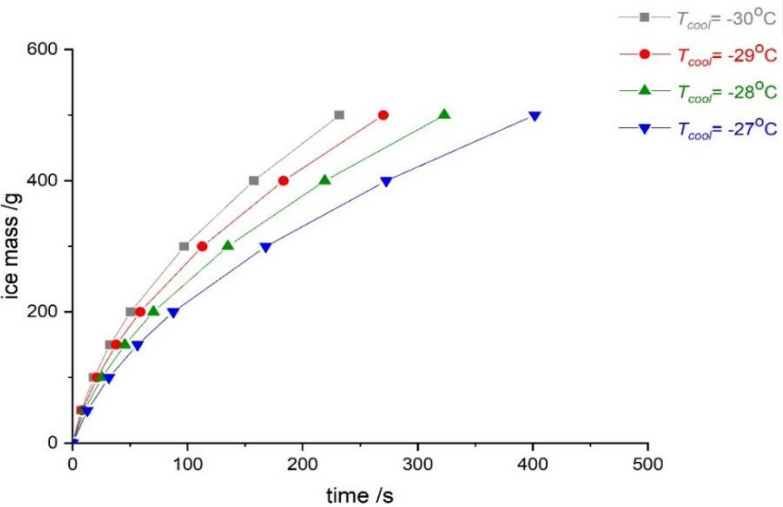


Figure 3.29: The ice mass as a function of time at various amount of coolant temperature.

The heat flux from the coolant to the solution is a function of coolant temperature. Therefore, one of the primary parameters to control the ice production rate is the coolant temperature. According to a similar study, in the fewer coolant temperatures, the production rates of ice are higher (Shi and Zhang, 2014). In Figure 3.29, the produced ice crystals as a function of T_{cool} over time at the constant amounts of N and

\dot{V} are shown. According to Figure 3.29, with decreasing the coolant temperature, the production rates of ice increases and less time is required to produce specific amounts of ice. If it is assumed that amounts of N and \dot{V} are 150 rpm and $10^{-3}\text{m}^3\cdot\text{s}^{-1}$, respectively, the required time to produce 500g ice, at the coolant temperature between -30 and -27°C can be considered. According to Figure 3.29, with increasing the coolant temperature between -30°C and -27°C , the time required to produce 500 g ice increases about 73% which is a remarkable amount. This result can be demonstrated by the effect of coolant temperature on the heat flux. Based on Equation 3.16, if the coolant temperature difference between the inlet and outlet is neglected and solution temperature is constant at the eutectic temperature, the coolant temperature and heat flux will be directly related and with decreasing the coolant temperature, the temperature difference between the solution and coolant and consequently the heat flux increases. According to Equation 3.61, due to \dot{Q}_{cool} and crystal production rate are directly related, with increasing \dot{Q}_{cool} , production rate increases.

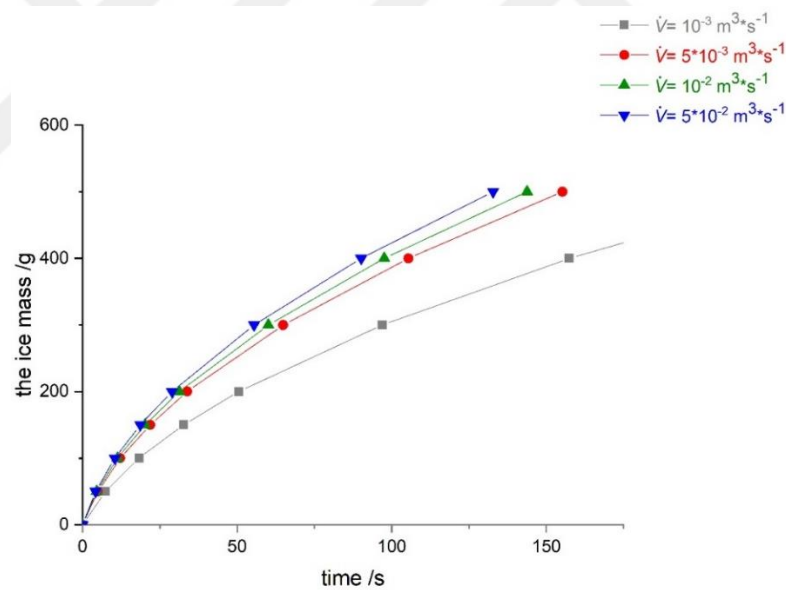


Figure 3.30: Ice mass production versus time at different coolant volumetric flow rate.

According to the experimental study of Hawlader and Wahed, with increasing the coolant volumetric flow rate, the crystal production rate increases (Hawlader and Wahed, 2009). In Figure 3.30, the produced ice crystals versus time in the various amounts of the coolant volumetric flow rate are shown. In Figure 3.30, it is assumed that N and T_{cool} are constant and their amounts are 150 rpm and -30°C , respectively. Based on Figure 3.30, the time required to produce 500g in the coolant volumetric

flow rate between 0.005 and $0.1 \text{ m}^3\cdot\text{s}^{-1}$ decreases by approximately 42%. However, the changes in the required time in the coolant volumetric flow rate between $10^{-3}\text{m}^3\cdot\text{s}^{-1}$ and $5 \times 10^{-3} \text{ m}^3\cdot\text{s}^{-1}$ is about 33% and between $10^{-3} \text{ m}^3\cdot\text{s}^{-1}$ and $5 \times 10^{-2} \text{ m}^3\cdot\text{s}^{-1}$, it decreases by approximately 14% . This result can be demonstrated by the effect of \dot{V} on \dot{Q} . According to Figure 3.21, the effect of coolant volumetric flow rate on the heat flux in the higher rates is few. Therefore, due to the heat flux and crystal production are directly proportional, the coolant flow rate cannot have a remarkable effect on ice production rate at higher amounts.

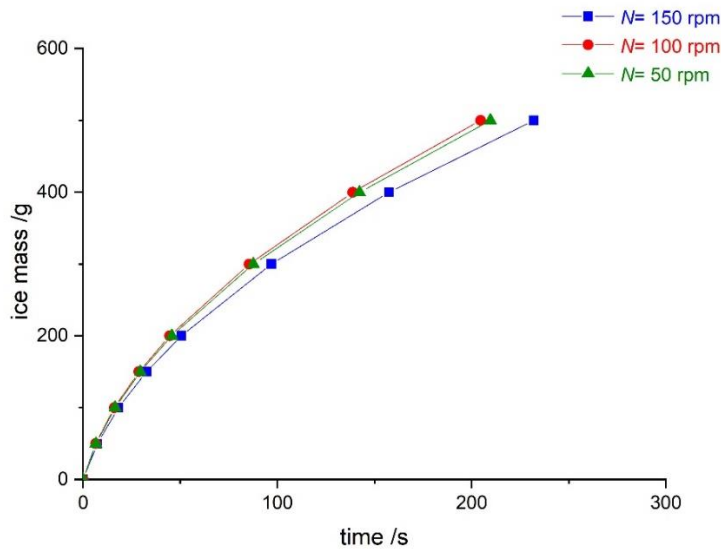


Figure 3.31: The ice mass as a function of time at different scraper rotational speed.

The scraper rotational speed is one of the main parameters which can affect the ice production rate (Vaessen et al., 2003a). N can control ice production rate by affecting both \dot{Q} and P_s . N can enhance the solution heat transfer coefficient and consequently the heat flux. In the crystallizing condition, N can control the crystal production rate by affecting on the scraper power consumption and the Reynolds number. According to Equation 3.61, the scraper power consumption and ice production are reversely proportional and directly proportional to Re and consequently overall heat transfer coefficient. In Figure 3.31, the produced ice mass is shown as a function of time at different scraper rotational speed and constant the coolant volumetric flow rate and temperature. In this figure, N is varied between 50 and 150 rpm and \dot{V} and T_{cool} are constant at $0.1 \text{ m}^3\cdot\text{s}^{-1}$ and -30°C , respectively. According to Figure 3.31, the required time to produce 500 g ice, if N is varied between 50 and 150 rpm increases by

approximately 10%. Although, according to an experimental study, with increasing the scraper rotational speed, the ice production rate decreases as the same as the result of this study. As a result, it can be concluded that in the crystallizing condition, the penetration theory is not proper to calculate solution heat transfer coefficient and Equation 3.56 must be preferred. Furthermore according to Figure 3.31, the efficiency of the system to produce ice in the fewer scraper rotational speeds is higher (Liu et al., 2019).

3.4 Conclusion

In this study, the heat transfer in a batch eutectic freeze crystallizer which contains sodium chloride solution was modeled for non-crystallizing and crystallizing at different process conditions.

The following conclusions were derived from modeling of the heat transfer in the EFC process for the non-crystallizing condition at the eutectic temperature:

- T_{in} as an independent parameter is directly related to T_{out} and T_b , and is inversely related to \dot{Q}_{cool} .
- T_{out} , \dot{Q}_{cool} and T_b are changed as a function of \dot{V} differently based on the coolant flow regime. Even though the effect of \dot{V} in the turbulent region is high, in the higher flow rates, T_{out} , \dot{Q}_{cool} and T_b are not changed significantly as a function of \dot{V} .
- Although N is directly proportional to T_{out} , \dot{Q}_{cool} and T_b , it does not have a significant effect on T_{out} , \dot{Q}_{cool} and T_b . However, N influences P_s remarkably.

After the steady state condition of the solution temperature, it was assumed that the solution temperature was cooled down from the environment temperature to the eutectic temperature. In this condition, it is concluded that:

- Due to the difference between inlet and outlet temperature was negligible, the time required to cool down the solution as a function of T_{cool} was considered and t is related to T_{cool} directly. Therefore, with approaching T_{cool} to T_{EUT} , the time required to cool down the solution increases.

- Time required to cool down the solution is inversely proportional to \dot{V} . However, in the turbulent region where cooling rate is higher than laminar region, changes of t as a function of \dot{V} at the less flow rate is higher.
- Between $N=50$ rpm, 100 rpm and 150 rpm, the optimum amount of the rotational speed is $N=100$ rpm.

In the last part of the study, the heat transfer in the EFC process for sodium chloride solution was considered in the crystalizing condition. According to the result of this part, it can be conclude that:

- Since more than 75% of produced crystals were ice, ice properties were used as the produced crystal property. According to calculation results, the ice particles only remarkably affect the viscosity of the solution. However, the heat flux from the coolant to the solution and the scraper power consumption were not influenced significantly by the ice crystals.
- The ice production rate is profoundly affected by T_{cool} and the time required to produce the specific amount of ice crystals is increased notably with increasing T_{cool} .
- The effect of \dot{V} on the production rate of ice at higher flow rate is less. At volumetric flow rate above $10^{-2} \text{ m}^3 \cdot \text{s}^{-1}$ value, the production rate of ice crystals is almost constant.
- In this part, due to the remarkable dependency of solution viscosity to the ice mass fraction, the solution heat transfer coefficient was not calculated via penetration theory. In this condition, between $N=50$ rpm, 100 rpm and 150 rpm, the production at $N=100$ rpm is higher than others.

The aim of this study was to consider the EFC process for sodium chloride solution at various process conditions. Although some interesting conclusions were derived, there are some recommendations which can be considered in further studies:

- Due to considering the effect of crystal particle on the solution viscosity, the effect of scraper rotational speed was neglected that it can be applied in future studies.
- EFC process for sodium chloride must be carried out experimentally at the optimum process conditions of this study.

REFERENCES

- A.Ananthanarayanan; M.Goswami; G.P.Kothiyal (Eds.)** (2017): *Materials Under Extreme Conditions*: Elsevier.
- Abràmoff, Michael D.; Magalhães, Paulo J.; Ram, Sunanda J.** (2004): Image processing with ImageJ. In *Biophotonics international* 11 (7), pp. 36–42.
- Agrawal, S. G.; Paterson, A. H. J.** (2015): Secondary Nucleation: Mechanisms and Models. In *Chemical Engineering Communications* 202 (5), pp. 698–706. DOI: 10.1080/00986445.2014.969369.
- Ahmad, Shahrokh; Oishe, Sadia Noon; Rahman, Lutfor** (2017): The augmentation of heat transfer in a pipe flow using a swirling perforated twisted (SPT) tape insert. In *Proceedings Of The 1ST International Conference On Mechanical Engineering And Applied Science (ICMEAS 2017)*. Dhaka, Bangladesh, 22–23 February 2017: Author(s) (AIP Conference Proceedings), p. 20013, checked on 2/7/2019.
- Aktaş, Zeki; Woodburn, E.Ted** (2000): Effect of addition of surface active agent on the viscosity of a high concentration slurry of a low-rank British coal in water. In *Fuel Processing Technology* 62 (1), pp. 1–15. DOI: 10.1016/S0378-3820(99)00059-4.
- Allison, Tom** (1998): JANAF Thermochemical Tables, NIST Standard Reference Database 13.
- Andrei S.Batsanov (Ed.)** (1999): *Encyclopedia of Spectroscopy and Spectrometry. Small Molecule Applications of X-Ray Diffraction*: Elsevier.
- Aragones, J. L.; Sanz, E.; Vega, C.** (2012): Solubility of NaCl in water by molecular simulation revisited. In *The Journal of chemical physics* 136 (24), p. 244508. DOI: 10.1063/1.4728163.

- Archer, Donald G.; Carter, Richard W.** (2000a): Thermodynamic Properties of the NaCl + H₂O System. 4. Heat Capacities of H₂O and NaCl(aq) in Cold-Stable and Supercooled States †. In *J. Phys. Chem. B* 104 (35), pp. 8563–8584. DOI: 10.1021/jp0003914.
- Barrett, P.; Glennon, B.** (2002): Characterizing the metastable zone width and solubility curve using Lasentec FBRM and PVM. In *Chemical Engineering Research and Design* 80 (7), pp. 799–805.
- Bethell, D. E.; Sheppard, N.** (1955): The infra-red spectrum and structure of boric acid. In *Transactions of the Faraday Society* 51, pp. 9–15.
- Bellas, J.; Chaer, I.; Tassou, S. A.** (2002): Heat transfer and pressure drop of ice slurries in plate heat exchangers. In *Applied Thermal Engineering* 22 (7), pp. 721–732. DOI: 10.1016/S1359-4311(01)00126-0.
- Bergman, T. L.; Incropera, Frank P.** (2011): Fundamentals of heat and mass transfer. 7th ed. Hoboken NJ: Wiley, checked on 1/11/2019.
- Bonales, L. J.; Rodriguez, A. C.; Sanz, P. D.** (2017): Thermal conductivity of ice prepared under different conditions. In *International Journal of Food Properties* 20 (sup1), pp. 610–619. DOI: 10.1080/10942912.2017.1306551.
- Camacho Corzo, Diana M.; Borissova, Antonia; Hammond, Robert B.; Kashchiev, Dimo; Roberts, Kevin J.; Lewtas, Ken; More, Iain** (2014): Nucleation mechanism and kinetics from the analysis of polythermal crystallisation data: methyl stearate from kerosene solutions. In *CrystEngComm* 16 (6), pp. 974–991. DOI: 10.1039/C3CE41098F.
- Choi, S.U.S.; Eastman, J. A. (Eds.)** (1995): Enhancing thermal conductivity of fluids with nanoparticles. Conference: 1995 International mechanical engineering congress and exhibition,, Oct 1995. San Francisco, CA (United States).
- Christen, P.; Hofmann, E. (Eds.)** (1991): EJB Reviews 1990. Berlin, Heidelberg: Springer Berlin Heidelberg.
- Civan, Faruk** (2007): Crystal Growth And Scale Formation In Porous Media 11Parts reprinted by permission of the Society of Petroleum Engineers from Civan, ©1996a SPE, SPE 31101 paper. In Faruk Civan (Ed.): Reservoir Formation

Damage. *Crystal Growth And Scale Formation In Porous Media*: Elsevier, pp. 235–255.

Collins, Tony J. (2007): ImageJ for microscopy. In *BioTechniques* 43 (1 Suppl), pp. 25–30. DOI: 10.2144/000112517.

Dolomanov, Oleg V.; Bourhis, Luc J.; Gildea, Richard J.; Howard, Judith A. K.; Puschmann, Horst (2009): OLEX2 : a complete structure solution, refinement and analysis program. In *J Appl Crystallogr* 42 (2), pp. 339–341. DOI: 10.1107/S0021889808042726.

Dydo, P.; Turek, M. (2013): Boron transport and removal using ion-exchange membranes: A critical review. In *Desalination* 310, pp. 2–8. DOI: 10.1016/j.desal.2012.08.024.

E. House, James; E. House, Kathleen (2016): *Descriptive Inorganic Chemistry*: Elsevier.

Elif Genceli Güner, F.; Wåhlin, Johan; Hinge, Mogens; Kjelstrup, Signe (2015): The temperature jump at a growing ice–water interface. In *Chemical Physics Letters* 622, pp. 15–19. DOI: 10.1016/j.cplett.2015.01.013.

Elliott, Roy (1988): Solidification of cast irons. In : *Cast Iron Technology*: Elsevier, pp. 91–125.

Engineering and Operating Guide (2008), checked on 1/30/2019.

Farhat, Ali; Ahmad, Farrukh; Arafat, Hassan (2013): Analytical techniques for boron quantification supporting desalination processes: A review. In *Desalination* 310, pp. 9–17. DOI: 10.1016/j.desal.2011.12.020.

Fernández-Seara, José; Diz, Rubén (2014): Thermo-hydraulic behavior of ice slurry in an offset strip-fin plate heat exchanger. In *International Journal of Refrigeration* 41, pp. 171–180. DOI: 10.1016/j.ijrefrig.2013.12.011.

Fort, Douglas J.; Fort, Troy D.; Mathis, Michael B.; Ball, R. Wayne (2016): Boric Acid Is Reproductively Toxic to Adult *Xenopus laevis*, but Not Endocrine Active. In *Toxicological sciences : an official journal of the Society of Toxicology* 154 (1), pp. 16–26. DOI: 10.1093/toxsci/kfw138.

- Garside, John; Davey, Roger J.** (1980): Invited Review Secondary Contact Nucleation: Kinetics, Growth And Scale-Up. In *Chemical Engineering Communications* 4 (4-5), pp. 393–424. DOI: 10.1080/00986448008935918.
- Genceli, F. E.; Gärtner, R.; Witkamp, G. J.** (2005): Eutectic freeze crystallization in a 2nd generation generationcooled disk column crystallizer for MgSO₄·H₂O system 275 (1-2), pp. 1369–1372.
- Genceli, Fatma Elif** (2008): Scaling-up eutectic freeze crystallization. [S.l.]: [s.n.].
- Gerard F.Arkenbout**: Melt Crystallization Technology.
- Gilmer, G. H.; Bennema, P.** (1972): Simulation of Crystal Growth with Surface Diffusion. In *Journal of Applied Physics* 43 (4), pp. 1347–1360. DOI: 10.1063/1.1661325.
- Goldbloom, Richard B.; Goldbloom, Alton** (1953): Boric acid poisoning. In *The Journal of Pediatrics* 43 (6), pp. 631–643. DOI: 10.1016/S0022-3476(53)80304-5.
- Griesser, Hans J.** (2016): Thin film coatings for biomaterials and biomedical applications [electronic resource]. Duxford, UK: Woodhead Publishing (Woodhead Publishing series in biomaterials, number 110).
- Gros, Håkan; Kilpiö, Teuvo; Nurmi, Juha** (2001): Continuous cooling crystallization from solution. In *Powder Technology* 121 (1), pp. 106–115. DOI: 10.1016/S0032-5910(01)00382-5.
- Guan, Zhimin; Lv, Jiafei; Bai, Peng; Guo, Xianghai** (2016): Boron removal from aqueous solutions by adsorption — A review. In *Desalination* 383, pp. 29–37. DOI: 10.1016/j.desal.2015.12.026.
- Guilpart, Jacques; Stamatiou, Evangelos; Delahaye, Anthony; Fournaison, Laurence** (2006): Comparison of the performance of different ice slurry types depending on the application temperature. In *International Journal of Refrigeration* 29 (5), pp. 781–788. DOI: 10.1016/j.ijrefrig.2005.11.009.
- Hasan, Mehdi; Filimonov, Roman; Chivavava, Jemitias; Sorvari, Joonas; Louhi-Kultanen, Marjatta; Lewis, Alison Emslie** (2017): Ice growth on the cooling surface in a jacketed and stirred eutectic freeze crystallizer of aqueous Na₂SO₄.

4 solutions. In *Separation and Purification Technology* 175, pp. 512–526. DOI: 10.1016/j.seppur.2016.10.014.

Hawladar, M.N.A.; Wahed, M. A. (2009): Analyses of ice slurry formation using direct contact heat transfer. In *Applied Energy* 86 (7-8), pp. 1170–1178. DOI: 10.1016/j.apenergy.2008.11.003.

He, Guangwen; Wong, Annie B.H.; Chow, Pui Shan; Tan, Reginald B.H. (2011): Effects of the rate of supersaturation generation on polymorphic crystallization of m-hydroxybenzoic acid and o-aminobenzoic acid. In *Journal of Crystal Growth* 314 (1), pp. 220–226. DOI: 10.1016/j.jcrysgro.2010.11.105.

Hoornweg, Daniel; Bhada-Tata, Perinaz (2012): WHAT A WASTE ;A Global Review of Solid Waste Management.

Horrocks, A. Richard; Price, Dennis (2008): Advances in fire retardant materials. Cambridge: Woodhead (Woodhead Publishing in materials).

Hosmane, Narayan S. (2012): Boron science. New technologies and applications / edited by Narayan S. Hosmane. Boca Raton, FL: CRC Press.

Howe, Paul D. (1998): A review of boron effects in the environment. In *Biological Trace Element Research* 66 (1), pp. 153–166. DOI: 10.1007/BF02783135.

Hubbe, Martin A.; Becheleni, Emily M. A.; Lewis, Alison E.; Peters, Edward M.; Gan, Weixing; Nong, Guanzai et al. (2018): Recovery of Inorganic Compounds from Spent Alkaline Pulping Liquor by Eutectic Freeze Crystallization and Supporting Unit Operations: A Review. In *BioResources* 13 (4). DOI: 10.15376/biores.13.4.Hubbe.

Inaba, Hideo; Kim, Myoung-Jun; Horibe, Akihiko (2004): Melting Heat Transfer Characteristics of Microencapsulated Phase Change Material Slurries With Plural Microcapsules Having Different Diameters. In *J. Heat Transfer* 126 (4), p. 558. DOI: 10.1115/1.1773584.

Kabay, Nalan; Güler, Enver; Bryjak, Marek (2010): Boron in seawater and methods for its separation — A review. In *Desalination* 261 (3), pp. 212–217. DOI: 10.1016/j.desal.2010.05.033.

Kadam, Somnath S.; Kulkarni, Samir A.; Coloma Ribera, Roger; Stankiewicz, Andrzej I.; ter Horst, Joop H.; Kramer, Herman J.M. (2012): A new view

- on the metastable zone width during cooling crystallization. In *Chemical Engineering Science* 72, pp. 10–19. DOI: 10.1016/j.ces.2012.01.002.
- Karthika, S.; Radhakrishnan, T. K.; Kalaichelvi, P.** (2016): A Review of Classical and Nonclassical Nucleation Theories. In *Crystal Growth & Design* 16 (11), pp. 6663–6681. DOI: 10.1021/acs.cgd.6b00794.
- Kauffeld, M.; Wang, M. J.; Goldstein, V.; Kasza, K. E.** (2010): Ice Slurry Applications. In *Revue internationale du froid* 33 (8), pp. 1491–1505. DOI: 10.1016/j.ijrefrig.2010.07.018.
- Kestin, Joseph; Sokolov, Mordechai; Wakeham, William A.** (1978): Viscosity of liquid water in the range– 8 C to 150 C. In *Journal of Physical and Chemical Reference Data* 7 (3), pp. 941–948.
- Kim, Dae Hyun** (2011): A review of desalting process techniques and economic analysis of the recovery of salts from retentates. In *Desalination* 270 (1-3), pp. 1–8. DOI: 10.1016/j.desal.2010.12.041.
- Kim, Kwang-Joo; Mersmann, A.** (1997): Melt Crystallization with Direct Contact Cooling Techniques. In *Chemical Engineering Research and Design* 75 (2), pp. 176–182. DOI: 10.1205/026387697523426.
- Kim, Sunghwan; Chen, Jie; Cheng, Tiejun; Gindulyte, Asta; He, Jia; He, Siqian et al.** (2019): PubChem 2019 update: improved access to chemical data. In *Nucleic acids research* 47 (D1), D1102-D1109. DOI: 10.1093/nar/gky1033.
- Kitahama, K.; Kiriya, R.; Baba, Y.** (2005): C Helvacı, Dokuz Eylül Üniversitesi, İzmir, Turkey. In *Geochemistry* 18, pp. 1733–1750.
- Kondaiah, G.C.M.; Reddy, L. Amarnath; Babu, K. Srihari; Gurav, V. M.; Huge, K. G.; Bandichhor, R. et al.** (2008): Boric acid: an efficient and environmentally benign catalyst for transesterification of ethyl acetoacetate. In *Tetrahedron Letters* 49 (1), pp. 106–109. DOI: 10.1016/j.tetlet.2007.11.008.
- Knodel, B. D.; France, D. M.; Choi, U. S.; Wambsganss, M. W.** (2000): Heat transfer and pressure drop in ice-water slurries. In *Applied Thermal Engineering* 20 (7), pp. 671–685. DOI: 10.1016/S1359-4311(99)00046-0.
- Kramer, H.J.M.; van Rosmalen, G. M.** (2000): Encyclopedia of Separation Science.

- Ku, Warren W.; Chapin, Robert E.; Wine, Robert N.; Gladen, Beth C.** (1993): Testicular toxicity of boric acid (BA): Relationship of dose to lesion development and recovery in the F344 rat. In *Reproductive Toxicology* 7 (4), pp. 305–319. DOI: 10.1016/0890-6238(93)90020-8.
- Kubota, Noriaki** (2008): A new interpretation of metastable zone widths measured for unseeded solutions. In *Journal of Crystal Growth* 310 (3), pp. 629–634. DOI: 10.1016/j.jcrysgro.2007.11.123.
- L.YuS.M.Reutzl-Edens (Ed.)** (2003): *Encyclopedia of Food Sciences and Nutrition*: Elsevier.
- Lax, Ellen; Synowietz, Claudia; Schäfer, Klaus** (1964-70 v 1, 1967): *Taschenbuch für Chemiker und Physiker*. 3., völlig neu bearb. Aufl. Edited by D'Ans. Berlin, New York: Springer.
- Lenka, Maheswata; Sarkar, Debasis** (2014): Determination of metastable zone width, induction period and primary nucleation kinetics for cooling crystallization of L-asparaginohydrate. In *Journal of Crystal Growth* 408, pp. 85–90. DOI: 10.1016/j.jcrysgro.2014.09.027.
- Leyland, Debbie; Chivavava, Jemittias; Lewis, Alison E.** (2019): Investigations into ice scaling during Eutectic Freeze Crystallization of brine streams at low scraper speeds and high supersaturation. In *Separation and Purification Technology*. DOI: 10.1016/j.seppur.2019.03.025.
- Li, Gang; Hwang, Yunho; Radermacher, Reinhard; Chun, Ho-Hwan** (2013): Review of cold storage materials for subzero applications. In *Energy* 51, pp. 1–17. DOI: 10.1016/j.energy.2012.12.002.
- Liu, Xi; Li, Yueling; Zhuang, Kunyu; Fu, Ruansong; Lin, Shi; Li, Xuelai** (2019): Performance Study and Efficiency Improvement of Ice Slurry Production by Scraped-Surface Method. In *Applied Sciences* 9 (1), p. 74. DOI: 10.3390/app9010074.
- Lorain, Olivier; Thiebaud, Pascal; Badorc, Eugenie; Aurelle, Yves** (2001): Potential of freezing in wastewater treatment: soluble pollutant applications. In *Water Research* 35 (2), pp. 541–547. DOI: 10.1016/S0043-1354(00)00287-6.

- M. A. Mehrabian:** The overall heat transfer characteristics of a double pipe heat exchanger.
- M. Shaaban, Mahmoud** (2010): Role of Boron in Plant Nutrition and Human Health. In *American J. of Plant Physiology* 5 (5), pp. 224–240. DOI: 10.3923/ajpp.2010.224.240.
- Mahdi; M, Davood; V, Mohsen; S, Behzad** (2017): Boric Acid Production from a Low-Grade Boron Ore with Kinetic Considerations. In *Mod Chem Appl* 05 (02). DOI: 10.4172/2329-6798.1000218.
- Makoto Tachibana** (2017): Beginner's Guide to Flux Crystal Growth. Mechanisms of Crystal Growth from Fluxed Solutions: Springer, Tokyo.
- Malato, S.; Fernández-Ibáñez, P.; Maldonado, M. I.; Blanco, J.; Gernjak, W.** (2009): Decontamination and disinfection of water by solar photocatalysis: Recent overview and trends. In *Catalysis Today* 147 (1), pp. 1–59. DOI: 10.1016/j.cattod.2009.06.018.
- Martínez, D. S.; Solano, J. P.; Illán, F.; Viedma, A.** (2014): Analysis of heat transfer phenomena during ice slurry production in scraped surface plate heat exchangers. In *International Journal of Refrigeration* 48, pp. 221–232. DOI: 10.1016/j.ijrefrig.2014.07.020.
- Matsumoto, Michiaki; Kondo, Kazuo; Hirata, Makoto; Kokubu, Shuzo; Hano, Tadashi; Takada, Tokio** (1997): Recovery of Boric Acid from Wastewater by Solvent Extraction. In *Separation Science and Technology* 32 (5), pp. 983–991. DOI: 10.1080/01496399708000940.
- McCann, J.; Bryson, D.** (2015): Textile-led design for the active ageing population. Oxford: Woodhead Publishing (Woodhead Publishing series in textiles, 142).
- Meewisse, J. W.; Infante Ferreira, C. A.** (2003): Validation of the use of heat transfer models in liquid/solid fluidized beds for ice slurry generation. In *International Journal of Heat and Mass Transfer* 46 (19), pp. 3683–3695. DOI: 10.1016/S0017-9310(03)00171-6.
- Melinder, Å.** (2010): Properties and other aspects of aqueous solutions used for single phase and ice slurry applications. In *International Journal of Refrigeration* 33 (8), pp. 1506–1512. DOI: 10.1016/j.ijrefrig.2010.07.014.

- Mersmann, A.** (1999): Crystallization and precipitation. In *Chemical Engineering and Processing: Process Intensification* 38 (4-6), pp. 345–353. DOI: 10.1016/S0255-2701(99)00025-2.
- Moore, John A.; Committee, Expert Scientific** (1997): An assessment of boric acid and borax using the IEHR Evaluative process for assessing human developmental and reproductive toxicity of agents. In *Reproductive Toxicology* 11 (1), pp. 123–160. DOI: 10.1016/S0890-6238(96)00204-3.
- Mouneer, T. A.; El-Morsi, M. S.; Nosier, M. A.; Mahmoud, N. A.** (2010): Heat transfer performance of a newly developed ice slurry generator: A comparative study. In *Ain Shams Engineering Journal* 1 (2), pp. 147–157. DOI: 10.1016/j.asej.2011.05.004.
- Mullin, J. W.** (1976): Industrial Crystallization. Boston, MA: Springer US.
- Mullin, J. W.** (1993): Crystallization. 3rd.
- Mullin, J. W.** (2001): Crystallization. Nucleation. 4th ed. Oxford: Butterworth-Heinemann. Available online at <http://www.loc.gov/catdir/description/els031/2001276303.html>.
- N.Ye; J.-Y.Wang; R.I.Boughton; M.-C.Hong** (Eds.) (2017): Modern Inorganic Synthetic Chemistry. Functional Crystals. 2nd ed.: Elsevier.
- Nasef, Mohamed Mahmoud; Nallappan, Madana; Ujang, Zaini** (2014): Polymer-based chelating adsorbents for the selective removal of boron from water and wastewater: A review. In *Reactive and Functional Polymers* 85, pp. 54–68. DOI: 10.1016/j.reactfunctpolym.2014.10.007.
- Nývlt, Jaroslav** (1984): Nucleation and growth rate in mass crystallization. In *Progress in Crystal Growth and Characterization* 9 (3-4), pp. 335–370.
- Omar, Waid; Ulrich, Joachim** (2006): Solid Liquid Equilibrium, Metastable Zone, and Nucleation Parameters of the Oxalic Acid–Water System. In *Crystal Growth & Design* 6 (8), pp. 1927–1930. DOI: 10.1021/cg060112n.
- Osueke, Christian O.; Onokwai, Anthony O.; Adeoye, Adeyinka O.** (2015): Experimental Investigation on the Effect of Fluid Flow Rate on the Performance of a Parallel Flow Heat Exchanger (2349-2163), checked on 2/7/2019.

- Ozbek, H.** (1977): Viscosity Of Aqueous Sodium Chloride Solutions From 0 - 150oC. Lawrence Berkeley National Laboratory.
- P. Pronk, M. Rodriguez Pascual, Geert-Jan Witkamp** (2005): Maximum temperature difference without ice-scaling in scraped surface crystallizers during eutectic freeze crystallization.
- Parks, Jeffrey L.; Edwards, Marc** (2005): Boron in the Environment. In *Critical Reviews in Environmental Science and Technology* 35 (2), pp. 81–114. DOI: 10.1080/10643380590900200.
- Perry, Robert H.; Green, Don W.** (2008): Perry's chemical engineers' handbook. 8th ed. / prepared by a staff of specialists under the editorial direction of editor-in-chief, Don W. Green, late editor, Robert H. Perry. New York: McGraw-Hill Professional; London: McGraw-Hill [distributor]. Available online at <http://www.loc.gov/catdir/enhancements/fy0729/2007026072-d.html>.
- Peter Crafts** (2007): Chemical product design. The Role of Solubility Modeling and Crystallization in the Design of Active Pharmaceutical Ingredients. 23 volumes: Elsevier.
- Pohanish, Richard P.** (2017): Sittig's handbook of toxic and hazardous chemicals and carcinogens. Seventh edition. Norwich: William Andrew.
- Pramanik, Biplob Kumar; Thangavadivel, Kandasamy; Shu, Li; Jegatheesan, Veeriah** (2016): A critical review of membrane crystallization for the purification of water and recovery of minerals. In *Rev Environ Sci Biotechnol* 15 (3), pp. 411–439. DOI: 10.1007/s11157-016-9403-0.
- Prutting, S. M.; Cervený, J. D.** (1998): Boric acid vaginal suppositories: a brief review. In *Infectious diseases in obstetrics and gynecology* 6 (4), pp. 191–194.
- Qin, Frank; Chen, Xiao Dong; Ramachandra, Shashini; Free, Kevin** (2006): Heat transfer and power consumption in a scraped-surface heat exchanger while freezing aqueous solutions. In *Separation and Purification Technology* 48 (2), pp. 150–158. DOI: 10.1016/j.seppur.2005.07.018.
- Radleys company** (2018): Intillgent evaporation. Hei-VAP Rotary Evaporator. United Kingdom. Available online at <https://heidolph-instruments.com/en/service/downloads/operation>.

- Randall, D. G.; Nathoo, J.; Lewis, A. E.** (2011): A case study for treating a reverse osmosis brine using Eutectic Freeze Crystallization—Approaching a zero waste process. In *Desalination* 266 (1-3), pp. 256–262. DOI: 10.1016/j.desal.2010.08.034.
- Rao, Chetan S.; Hartel, Richard W.** (2006): Scraped surface heat exchangers. In *Critical reviews in food science and nutrition* 46 (3), pp. 207–219. DOI: 10.1080/10408390500315561.
- Rao, M. Narayana; Sultana, Razia; Kota, Sri Harsha** (2017): Solid and hazardous waste management. Science and engineering. Oxford England, India: Butterworth-Heinemann; distributed by BS Publications.
- Restuccio, Anthony; Mortensen, Mary Ellen; Kelley, Michael T.** (1992): Fatal ingestion of boric acid in an adult. In *The American Journal of Emergency Medicine* 10 (6), pp. 545–547. DOI: 10.1016/0735-6757(92)90180-6.
- Ross, R. G.; Andersson, P.; Sundqvist, B.; Backstrom, G.** (1984): Thermal conductivity of solids and liquids under pressure. In *Rep. Prog. Phys.* 47 (10), pp. 1347–1402. DOI: 10.1088/0034-4885/47/10/002.
- Şahin, Ö.** (1999): Yüzey Yükünün Kristalizasyon Kinetiğine Etkisi. Dissertation. Istanbul Technical University, Istanbul.
- Şahin, Ömer; Özdemir, Mustafa; Kendirci, Hasan; Nusret Bulutcu, A.** (2000): Determination of growth and dissolution mass rate of boric acid crystals by a simple computer program. In *Journal of Crystal Growth* 219 (1-2), pp. 75–82. DOI: 10.1016/S0022-0248(00)00532-7.
- Şahin, Sami** (2002): A mathematical relationship for the explanation of ion exchange for boron adsorption. In *Desalination* 143 (1), pp. 35–43. DOI: 10.1016/S0011-9164(02)00219-9.
- Schlesinger, William H.; Vengosh, Avner** (2016): Global boron cycle in the Anthropocene. In *Global Biogeochem. Cycles* 30 (2), pp. 219–230. DOI: 10.1002/2015GB005266.
- Seidell, A.; Linke, W. F.** (1965): Solubilities Inorganic and Metal-organic Compounds: A Compilation of Solubility Data from the Periodical Literature.

K-Z: American Chemical Society (v. 2). Available online at <https://books.google.com.tr/books?id=hOHZvQAACAAJ>.

Senapati, P. K.; Mishra, B. K.; Parida, A. (2010): Modeling of viscosity for power plant ash slurry at higher concentrations: Effect of solids volume fraction, particle size and hydrodynamic interactions. In *Powder Technology* 197 (1-2), pp. 1–8. DOI: 10.1016/j.powtec.2009.07.005.

Sheldrick, G. Mu (1997): SHELXS-97, Program for crystal structure solution: University of Göttingen, Germany Göttingen.

Sheldrick, George M. (2008): A short history of SHELX. In *Acta crystallographica. Section A, Foundations of crystallography* 64 (Pt 1), pp. 112–122. DOI: 10.1107/S0108767307043930.

Shi, X. J.; Zhang, P. (2014): Crystallization of tetra-n-butyl ammonium bromide clathrate hydrate slurry and the related heat transfer characteristics. In *Energy Conversion and Management* 77, pp. 89–97. DOI: 10.1016/j.enconman.2013.09.010.

Shiau, Lie-Ding; Lu, Tsan-Sheng (2014): A model for determination of the interfacial energy from the induction time or metastable zone width data based on turbidity measurements. In *CrystEngComm* 16 (41), pp. 9743–9752. DOI: 10.1039/C4CE01245C.

Shin, Sehyun; Lee, Sung-Hyuk (2000): Thermal conductivity of suspensions in shear flow fields. In *International Journal of Heat and Mass Transfer* 43 (23), pp. 4275–4284. DOI: 10.1016/S0017-9310(00)00050-8.

Shuvalov, R. R.; Burns, P. C. (2003a): CCDC 214361: Experimental Crystal Structure Determination.

Shuvalov, Robert R.; Burns, Peter C. (2003b): A new polytype of orthoboric acid, H(3)BO(3)-3T. In *Acta crystallographica. Section C, Crystal structure communications* 59 (Pt 6), i47-9. DOI: 10.1107/S0108270103009685.

Sokmen, Nihal; Buyukakinci, Banu Yeşim (2018): The Usage Of Boron/ Boron Compounds In The Textile Industry And Its Situation In Turkey. In *CBUP* 6, p. 1158. DOI: 10.12955/cbup.v6.1309.

- Sonmez, Fazil O.; Hahn, H. Thomas** (1997): Modeling of Heat Transfer and Crystallization in Thermoplastic Composite Tape Placement Process. In *Journal of Thermoplastic Composite Materials* 10 (3), pp. 198–240. DOI: 10.1177/089270579701000301.
- Stamatiou, E.; Meewisse, J. W.; Kawaji, M.** (2005): Ice slurry generation involving moving parts. In *International Journal of Refrigeration* 28 (1), pp. 60–72. DOI: 10.1016/j.ijrefrig.2004.07.016.
- Stankiewicz, Andrzej I.; Moulijn, Jacob A.** (2000): Process intensification: transforming chemical engineering. In *Chemical engineering progress* 96 (1), pp. 22–34.
- Stepakoff, G. L.; Siegelman, D.; Johnson, R.; Gibson, W.** (1974): Development of a eutectic freezing process for brine disposal. In *Desalination* 15 (1), pp. 25–38. DOI: 10.1016/S0011-9164(00)82061-5.
- Stewart, B. A.** (1985): *Advances in Soil Science. Boron in Water, Soils, and Plants.* With assistance of Keren. R, Bingham F. T. New York, NY: Springer New York (1).
- Swenne, Dirk A.** (1983): *The eutectic crystallization of NaCl.2H₂O and ice.* Dissertation.
- Taschenbuch für Chemiker und Physiker Band 3** (1970). Dritte Auflage. Berlin, Heidelberg: Springer- Verlag Berlin Heidelberg GmbH.
- Tonkovich, A.; Kuhlmann, D.; Rogers, A.; McDaniel, J.; Fitzgerald, S.; Arora, R.; Yuschak, T.** (2005): Microchannel Technology Scale-up to Commercial Capacity. In *Chemical Engineering Research and Design* 83 (6), pp. 634–639. DOI: 10.1205/cherd.04354.
- Ulrich, J.; Jones, M. J.:** *Chemical engineering and chemical process technology (EOLESS. Heat and mass transfer operations- crystallization.* Germany.
- Vacek, Václav; König, Axel** (1983): Heats of crystallization of potassium chloride and magnesium chloride hexahydrate from aqueous solutions at 298.15 K. A critical review. In *Thermochimica Acta* 70 (1-3), pp. 225–235. DOI: 10.1016/0040-6031(83)80197-X.

- Vaessen, R.J.C.; Janse, B.J.H.; Seckler, M. M.; Witkamp, G. J.** (2003a): Evaluation of the Performance of a Newly Developed Eutectic Freeze Crystallizer. In *Chemical Engineering Research and Design* 81 (10), pp. 1363–1372. DOI: 10.1205/026387603771339573.
- Vaessen, R.J.C.; Seckler, M. M.; Witkamp, G. J.** (2004): Heat transfer in scraped eutectic crystallizers. In *International Journal of Heat and Mass Transfer* 47 (4), pp. 717–728. DOI: 10.1016/j.ijheatmasstransfer.2003.07.028.
- Vaessen, Raymond; Seckler, Marcelo; Witkamp, Geert Jan** (2003b): Eutectic Freeze Crystallization with an Aqueous KNO_3 – HNO_3 Solution in a 100-L Cooled-Disk Column Crystallizer. In *Ind. Eng. Chem. Res.* 42 (20), pp. 4874–4880. DOI: 10.1021/ie020946c.
- Vaessen, R. C.J.; Ham, F.; Witkamp, G. J.** (2000): Eutectic Freeze Crystallization Using CO_2 Clathrates. In *Annals of the New York Academy of Sciences* 912 (1), pp. 483–495. DOI: 10.1111/j.1749-6632.2000.tb06803.x.
- Van der Ham, F.; Witkamp, G. J.; Graauw, J. de; van Rosmalen, G. M.** (1998): Eutectic freeze crystallization: Application to process streams and waste water purification. In *Chemical Engineering and Processing: Process Intensification* 37 (2), pp. 207–213. DOI: 10.1016/S0255-2701(97)00055-X.
- Van der Ham, F.; Witkamp, G.J; Graauw, J. de; van Rosmalen, G.M** (1999): Eutectic freeze crystallization simultaneous formation and separation of two solid phases. In *Journal of Crystal Growth* 198-199, pp. 744–748. DOI: 10.1016/S0022-0248(98)01003-3.
- VDI Heat Atlas** (2010). Berlin, Heidelberg: Springer Berlin Heidelberg, checked on 1/11/2019.
- Verbeek, J. J.** (2011): Eutectic freeze crystallization on sodium chloride. Analysis of a full experimental cycle, delft. TU Delft.
- Ward, Jeffrey D.; Mellichamp, Duncan A.; Doherty, Michael F.** (2006): Choosing an operating policy for seeded batch crystallization. In *AIChE J.* 52 (6), pp. 2046–2054. DOI: 10.1002/aic.10808.

- Weir, Robert J.; Fisher, Russell S.** (1972): Toxicologic studies on borax and boric acid. In *Toxicology and Applied Pharmacology* 23 (3), pp. 351–364. DOI: 10.1016/0041-008X(72)90037-3.
- Williams, Paul M.; Ahmad, Mansour; Connolly, Benjamin S.; Oatley-Radcliffe, Darren L.** (2015): Technology for freeze concentration in the desalination industry. In *Desalination* 356, pp. 314–327. DOI: 10.1016/j.desal.2014.10.023.
- Witkamp, G. J.; van Spronsen, Jacob** (2010): Production of sodium bicarbonate from a basic process stream. Patent no. 4. 49.
- Wojciech, B.; Januez, W. (Eds.)** (2014): The Metastable Zone of aqueous solutions. X Conference Chances and possibilities of chemical industry in EU.
- Wolska, Joanna; Bryjak, Marek** (2013): Methods for boron removal from aqueous solutions — A review. In *Desalination* 310, pp. 18–24. DOI: 10.1016/j.desal.2012.08.003.
- Woods, W. G.** (1994): An introduction to boron: history, sources, uses, and chemistry. In *Environmental health perspectives* 102 Suppl 7, pp. 5–11. DOI: 10.1289/ehp.94102s75.
- Yamagishi, Yasushi; Takeuchi, Hiromi; Pyatenko, Alexander T.; Kayukawa, Naoyuki** (1999): Characteristics of microencapsulated PCM slurry as a heat-transfer fluid. In *AIChE J.* 45 (4), pp. 696–707. DOI: 10.1002/aic.690450405.
- Yang, Guangyu; Kubota, Noriaki; Sha, Zuoliang; Louhi-Kultanen, Marjatta; Wang, Jinfu** (2006): Crystal Shape Control by Manipulating Supersaturation in Batch Cooling Crystallization. In *Crystal Growth & Design* 6 (12), pp. 2799–2803. DOI: 10.1021/cg0603873.
- Yu-ting, Wu; Bin, Liu; Chong-fang, Ma; Hang, Guo** (2009): Convective heat transfer in the laminar–turbulent transition region with molten salt in a circular tube. In *Experimental Thermal and Fluid Science* 33 (7), pp. 1128–1132. DOI: 10.1016/j.expthermflusci.2009.07.001.
- Zachariassen, W. H.** (1954): The precise structure of orthoboric acid. In *Acta Cryst* 7 (4), pp. 305–310. DOI: 10.1107/S0365110X54000886.

Zeng, Ruolang; Wang, Xin; Chen, Binjiao; Zhang, Yiping; Niu, Jianlei; Wang, Xichun; Di, Hongfa (2009): Heat transfer characteristics of microencapsulated phase change material slurry in laminar flow under constant heat flux. In *Applied Energy* 86 (12), pp. 2661–2670. DOI: 10.1016/j.apenergy.2009.04.025.

Zijlema, Tjakko G.; Geertman, Rob M.; Witkamp, Geert-Jan; van Rosmalen, Gerda M.; Graauw, Jan de (2000): Antisolvent Crystallization as an Alternative to Evaporative Crystallization for the Production of Sodium Chloride. In *Ind. Eng. Chem. Res.* 39 (5), pp. 1330–1337. DOI: 10.1021/ie990221h.



Appendix A

Appendix A.1: Single crystal XRD Report

A colorless rod-like specimen of H_3BO_3 , approximate dimensions 0.010 mm x 0.020 mm x 0.400 mm, was used for the X-ray crystallographic analysis. The X-ray intensity data were measured. In Table A.1, the details of data collection for single XRD of boric acid crystal for EFC process is shown.

Table A.1: Data collection details for EFC

Axis	dx/mm	2 θ / $^\circ$	ω / $^\circ$	ϕ / $^\circ$	χ / $^\circ$	Width/ $^\circ$	Frames	Time/s	Wavelength/ \AA	Voltage/kV	Current/mA	Temperature/K
Omega	52.789	12.68	-170.01	51.00	54.70	1.00	185	8.00	0.71076	50	30.0	120
Omega	52.789	12.68	-170.01	-156.00	54.70	1.00	185	8.00	0.71076	50	30.0	120
Omega	52.789	12.68	-170.01	-54.00	54.70	1.00	185	8.00	0.71076	50	30.0	120
Omega	52.789	12.68	-170.01	102.00	54.70	1.00	185	8.00	0.71076	50	30.0	120
Omega	52.789	12.68	-170.01	-105.00	54.70	1.00	185	8.00	0.71076	50	30.0	120
Omega	52.789	12.68	-170.01	0.00	54.70	1.00	185	8.00	0.71076	50	30.0	120
Omega	52.789	12.68	-170.01	153.00	54.70	1.00	185	8.00	0.71076	50	30.0	120
Omega	52.789	12.68	-170.01	51.00	54.70	1.00	185	8.00	0.71076	50	30.0	120

A total of 1480 frames were collected. The total exposure time was 3.29 hours. The frames were integrated with the Bruker SAINT software package using a wide-frame algorithm. The integration of the data using a triclinic unit cell yielded a total of 3683 reflections to a maximum θ angle of 28.18° (0.75 \AA resolution), of which 1239 were independent (average redundancy 2.973, completeness = 96.6%, $R_{\text{int}} = 5.01\%$,

$R_{\text{sig}} = 6.38\%$) and 923 (74.50%) were greater than $2\sigma(F^2)$. The final cell constants of $a = 6.336(3) \text{ \AA}$, $b = 6.997(3) \text{ \AA}$, $c = 7.001(4) \text{ \AA}$, $\alpha = 119.933(12)^\circ$, $\beta = 90.919(15)^\circ$, $\gamma = 102.147(14)^\circ$, volume = $260.3(2) \text{ \AA}^3$, are based upon the refinement of the XYZ-centroids of 1818 reflections above $20 \sigma(I)$ with $6.752^\circ < 2\theta < 55.61^\circ$. Data were corrected for absorption effects using the Multi-Scan method (SADABS). The ratio of minimum to the maximum apparent transmission was 0.835.

The structure was solved and refined using the Bruker SHELXTL Software Package, using the space group P -1, with Z = 4 for the formula unit, H_3BO_3 . The final anisotropic full-matrix least-squares refinement on F^2 with 83 variables converged at $R1 = 13.89\%$, for the observed data and $wR2 = 41.47\%$ for all data. The goodness-of-fit was 1.682. The largest peak in the final difference electron density synthesis was $1.757 \text{ e}^-/\text{\AA}^3$ and the largest hole was $-0.673 \text{ e}^-/\text{\AA}^3$ with an RMS deviation of $0.383 \text{ e}^-/\text{\AA}^3$. On the basis of the final model, the calculated density was 1.578 g/cm^3 and $F(000)$, 128 e^- .

Appendix A.2: Metastable Zone Width (MSZW) calculations

In Figure 2.12, the natural logarithm of cooling rate r is presented versus natural logarithm of MSZW. The cooling rate r is the change of initial temperature of to the solution T_1 to the minimum temperature of the solution before the nucleation T_2 over time t . As mentioned above, MSWZ is the difference between the minimum temperature of the solution before the nucleation T_2 and the eutectic temperature of the solution T_{EUT} . In Table A.2, the calculation spreadsheet of Figure 2.12 is shown.

Table A.2: The calculation spread sheet of Figure 2.12

T_2 (°C)	T_1 (°C)	t (h)	T/t (°C.h ⁻¹)	T_{EUT} (°C)	T_2 (°C)	MSZW(°C)	LnMSZW(°C)	LnT/t (°C.h ⁻¹)
-3.64	9.17	0.33	38.59	-0.79	-3.64	2.85	1.047	-3.65
-2.97	28.33	0.60	52.06	-0.79	-2.97	2.18	0.78	-3.95
-2.73	19.49	0.34	64.37	-0.79	-2.73	1.94	0.66	-4.16
-2.16	19.76	0.19	112.45	-0.79	-2.15	1.37	0.31	-4.72
-1.96	20.92	0.15	149.22	-0.79	-1.96	1.17	0.15	-5.00

Appendix A.3: Crystal size determination

Crystal size determination was made using microscope and computer programs of Image-Pro Plus and Image J. Obtained crystal samples were placed on a microscope lamella in order to measure the crystal dimensions after crystallization. Crystals were analyzed with Olympus BX51 microscope and photos of salt crystals were taken using a 5X lens. The recorded photos were then transferred to the Image-Pro Plus program. After that, Image J program was used for characteristic radius calculations. For the characterization of the crystals, the dominant circle form was accepted and the characteristic radius was calculated accordingly. The characteristic radius of the salt crystals was recorded in the computer program as pixels and the actual magnitudes and growth rates were calculated at the ratio of 0,001188213 millimeters/pixel determined by the calibration. Approximately 400 crystals were randomly determined from the photographs taken under a microscope for each batch residence time after reaching the eutectic point in the crystallizer. The area of each of these randomly selected 400 crystals was counted manually by the help of Image J. Area of each crystal was used to find the characteristic radius of the crystals. In this work, assuming the crystal shape to be a circle, the circle radius was calculated and by averaging all the radiuses per measurement, a representative crystal radius was found.

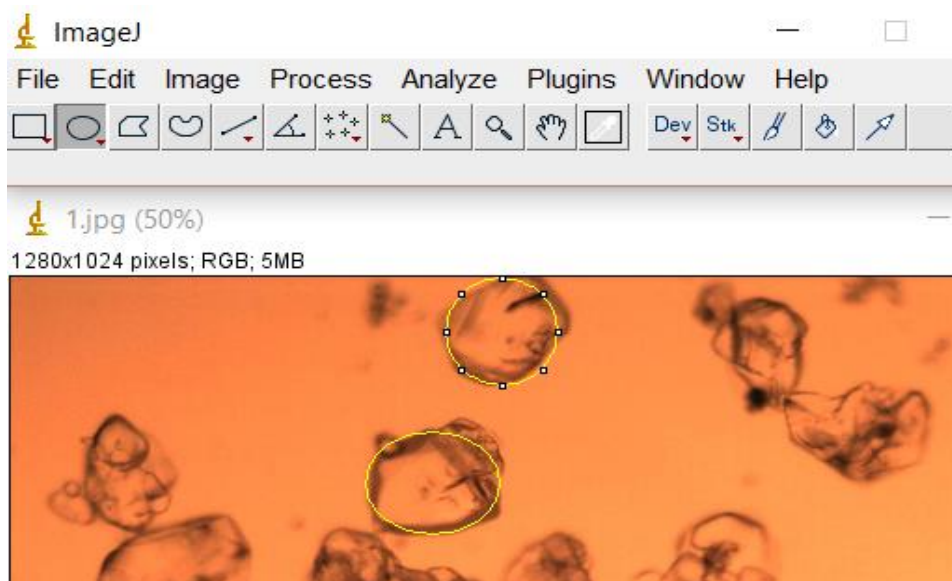


Figure A 3.1: Manual crystal counting with Image J.

Table A 3: Characteristic radius calculation from Image J results.

	Label	Area	Radius	R (mm)	R (μm)
1	1.jpg	1,80E+03	2,40E+01	2,85E-02	28,47
2	1.jpg	1,17E+03	1,93E+01	2,30E-02	22,95
3	1.jpg	8,12E+02	1,61E+01	1,91E-02	19,10

$$Radius = \sqrt{\frac{Area}{\pi}} \quad A.1$$

$$R(mm) = Radius \times 0.001188213 \text{ millimeters / pixel} \quad A.2$$

$$R(micrometers) = R(millimeters) \times 1000 \quad A.3$$

I.e. square roots of each area divided by pi number were calculated and multiplied by the ratio of 0.001188213 millimeters/pixel. The calculated value was converted to micrometers by multiplying with 1000. Average of approximately 400 radiuses were found to determine the characteristic radius of crystals.

Appendix A.4: Production rate and mass balance

In Section 2.3.4, the production rate of ice and boric acid crystals were presented. In this section, produced amount of ice and salt were considered in three different residence times; 2700s, 1800s and 900s. the coolant temperature was set -10°C for all of the experiments. In Table A.4.1, the result of initial mass transfer to determine amounts of extracted solid particles (ice+salt) is shown. According to this table, the total mass of solid particles for 2700s, 1800s and 900s residence time is achieved 76.51g, 74.47g and 62.02g.

Table A 4.1: The data spread sheet to determine the total mass of produced crystals.

Waiting time after EP (s)	2700	1800	900
Coolant temperature set (°C)	-10	-10	-10
Initial weight of solution (g)	834.32	839.78	842.28
Filtered crystal (g)	28.14	32.52	33.42
Passed solution (g)	751.94	760.84	777.82
Residual solution in bottom (g)	48.37	41.95	28.60
Total Crystals=filtered + residual (g)	76.51	74.47	62.02
Difference (weight)	5.87	4.47	2.44

After crystallization process, the boric acid can be found as either crystal or solution. In Table A.4.2, the weight percent of boric acid in (a) initial solution, (b) filtered crystal, (c) passed solution and (d) residual solution is shown. In this study, the concentration of boric acid was determined via titration. In the titration method, the concentration of the sample was determined using the following formulas.

$$C = \frac{N \times M_A \times V_2}{V_1} \quad \text{A.4}$$

In Equation A.4, C represents boric acid concentration, M_A molecular weight of boric acid, V_1 volume of sample, V_2 used the volume of 0.1M NaOH and N normality of 0.1M NaOH. The molecular weight of boric acid equals to 61.83 g.mol⁻¹. The volume

of sample for titration experiment was taken 10 ml and used volume of NaOH is presented in Table A.4.2. In Equation A.4, the normality of 0.1NaOH can be determined by standardization of NaOH solution. In the standardization experiment, potassium hydrogen phthalate ($C_8H_5KO_4$) was used to find the normality of 0.1 M NaOH solution. Approximately 1 g of potassium hydrogen phthalate ($C_8H_5KO_4$) is dissolved in 100 mL of distilled water. 3 drops of phenolphthalein are added to this solution and titrated with 0.1 M NaOH until the color change is observed. NaOH consumption is noted. The equation given in the formula calculates the normalization of the NaOH solution.

$$N = \frac{B}{0.20423 \times A} \quad A.5$$

In Equation A.5, N represents the normality of NaOH solution, B consumed amount of $C_8H_5KO_4$ and A consumed amount of NaOH.

Table A 4.2: The spreadsheet of weight percent calculation of boric acid in (a) initial solution (b) filtered crystal, (c) passed solution and (d) residual solution.

(a)

Waiting time after EP (s)	2700	1800	900
Consumed NaOH volume for 50% initial solution (ml)	21.59	21.28	21.51
Initial concentration of solution (g/l)	24.825	24.478	24.744
Weight percent of initial solution wt%	2.14	2.11	2.13

(b)

Waiting time after EP (s)	2700	1800	900
Consumed NaOH volume for 50% filtered crystal (ml)	30.61	24.05	10.43
Concentration of filtered crystal (g Boric Acid/litre)	35.36	27.78	12.05
Weight percent of filtered crystal wt%	3.51	2.76	1.20

(c)

Waiting time after EP (s)	2700	1800	900
Consumed NaOH volume for Passed solution (ml)	40.36	43.86	44.27
Concentration of passed solution (g/l)	23.47	25.33	25.58
Weight percent of filtered crystal wt%	2.33	2.51	2.54

(d)

Waiting time after EP (s)	2700	1800	900
Consumed NaOH volume for 50% Residual solution(ml)	20.71	15.74	14.68
Concentration of residual solution (g/l)	23.92	18.18	16.97
Weight percent of filtered crystal wt%	2.37	1.80	1.68

According to Table A.4.2, the amount of ice and boric acid crystals can be determined via mass balance. The amount of produced boric acid crystals is determined by the sum of filtered boric acid crystals and boric acid crystals in the residual solution. The relationship to calculate crystallized boric acid is shown below.

Crystallized $H_3BO_3 = (\text{Filtered crystal} * \text{concentration of filtered crystal} + \text{residual solution in bottom} * \text{concentration of residual solution}) / \text{Density of solution}$

The density of water and boric acid are 997 kg.m^{-3} and 1435 kg.m^{-3} . Therefore, the density of solution with 2.5% wt boric acid concentration is $1007.95 \text{ kg.m}^{-3}$. As mentioned, the total produced crystals are the sum of the crystallized ice and boric acid. Therefore, with determining the amount of produced boric acid, the amount of crystallized ice can be known. In Table A.4.3, the amount of produced ice and boric acid over time is presented. According to the values of this table, the production rate of ice and boric acid were calculated.

Table A 4.3: The amount of produced ice and boric acid over time.

Waiting time after EP (s)	2700	1800	900
Crystallized ice (g)_in fitted ice+residual	74.37	72.82	61.14
Crystallized H ₃ BO ₃ (g)_in filtred ice+residual	2.14	1.65	0.88



APPENDIX B

B.1 Calculations in non- crystalizing condition

In Table 3.3, the variation of the Reynolds number of solution is shown based on the scraper rotational speed. Re can be calculated as a function of N by Equation 3.7:

$$Re = \frac{\rho_s N d_r^2}{\mu_s} \quad 3.7$$

Table B.1: The variation of the Reynolds number of solution based on the scraper rotational speed

μ (cp)	d_r (m)	ρ_s (kg*m ⁻³)	N (rpm)	Re
4.342	$2 * 10^{-2}$	1089.42	50	5018.056
4.342	$2 * 10^{-2}$	1089.42	100	10036.11
4.342	$2 * 10^{-2}$	1089.42	150	15054.17
4.342	$2 * 10^{-2}$	1089.42	200	20072.22
4.342	$2 * 10^{-2}$	1089.42	250	25090.28

The calculations of P_s which are shown in Figure 3.15, for flat-blade turbine, pitched-blade impeller and marine-type propeller are shown below:

$$P_s = Ne \rho_s N^3 d_r^5 \quad A.1$$

for a baffled system with a flat-blade turbine Ne can be calculated by Equation 3.9 and Equation 3.10 (VDI Heat Atlas, 2010).

Table B.2 The scraper power consumption in non-crystallizing conditions as function of rotational speed for flat-blade turbine.

d_r (m)	ρ_s (kg*m ⁻³)	N (rpm)	Re	Ne	Ps (W)
$2 * 10^{-2}$	1089.42	50	5018.06	5	2.28
$2 * 10^{-2}$	1089.42	100	10036.11	5	18.24
$2 * 10^{-2}$	1089.42	150	15054.17	5	61.55
$2 * 10^{-2}$	1089.42	200	20072.22	5	145.90
$2 * 10^{-2}$	1089.42	250	25090.28	5	284.95

For a Pitched-blade impeller in a baffled crystallizer Ne is calculated by Equation 3.11 and Equation 3.12 (VDI Heat Atlas 2010).

Table B.3: The scraper power consumption in non-crystallizing conditions as function of rotational speed for pitched-blade impeller

d_r (m)	ρ_s (kg*m ⁻³)	N (rpm)	Re	Ne	Ps (W)
$2 * 10^{-2}$	1089.42	50	5018.06	3	1.31
$2 * 10^{-2}$	1089.42	100	10036.11	3	10.46
$2 * 10^{-2}$	1089.42	150	15054.17	3	35.30
$2 * 10^{-2}$	1089.42	200	20072.22	3	83.67
$2 * 10^{-2}$	1089.42	250	25090.28	3	163.41

According to Hirschberg's recommendation, the Newton number of a marine-type propeller is computed by Equation 3.13, Equation 3.14 and Equation 3.15 (VDI Heat Atlas 2010).

Table B.4: The scraper power consumption in non-crystallizing conditions as function of rotational speed for marine-type propeller.

d_r (m)	ρ_s (kg*m ⁻³)	N (rpm)	Re	Ne	Ps (W)
$2 * 10^{-2}$	1089.42	50	5018.06	0.44	0.19
$2 * 10^{-2}$	1089.42	100	10036.11	0.42	1.46
$2 * 10^{-2}$	1089.42	150	15054.17	0.41	4.80
$2 * 10^{-2}$	1089.42	200	20072.22	0.40	11.15
$2 * 10^{-2}$	1089.42	250	25090.28	0.40	21.44

To determine flow regime in the coolant, Equation 3.19 can be used to calculate Re . Also, according to Re , the equation to calculate Nu can be selected from Equation 3.23, Equation 3.24 and Equation 3.25. Finally, the coolant heat transfer coefficient can be calculated by Equation 3.26.

Table B.5: The relation between the volumetric flow rate and coolant heat transfer coefficient

Title	1 st point	2 nd point	3 rd point	4 th point	5 th point	6 th point	7 th point	8 th point
\dot{V} (m ³ *s ⁻¹)	0	$5*10^{-5}$	10^{-4}	$2*10^{-4}$	$3*10^{-4}$	$4*10^{-4}$	$8.5*10^{-4}$	10^{-3}
c_{pc} (kg*kJ ⁻¹ *K ⁻¹)	3.089	3.089	3.089	3.089	3.089	3.089	3.089	3.089
ρ_c (kg*m ⁻³)	1090.30	1090.30	1090.30	1090.30	1090.30	1090.30	1090.30	1090.30

μ (cp)	43.98	43.98	43.98	43.98	43.98	43.98	43.98	43.98
d_t (m)	10^{-2}	10^{-2}	10^{-2}	10^{-2}	10^{-2}	10^{-2}	10^{-2}	10^{-2}
L_t (m)	2	2	2	2	2	2	2	2
Pr	112.94	112.94	112.94	112.94	112.94	112.94	112.94	112.94
Re	0	578.74	1157.49	2314.98	3472.47	4629.96	9838.67	11574.90
Nu	3.65	11.18	14.53	18.75	18.02	115.08	148.57	169.2
α_{cool} ($W*m^{-2}*K^{-1}$)	119.72	366.82	615.08	1531.43	2696.20	3774.56	4873.12	5549.73

The solution heat transfer coefficient as a function of scraper rotational speed is calculated by Equation 3.33 which is drawn in Figure 3.17. Furthermore, the Reynolds number in the crystallizer is calculated by Equation 3.7. In Table B.6, the calculations of Figure 3.17 is shown.

Table B.6: The solution heat transfer coefficient as a function of the scraper rotational speed

Title	1 st point	2 nd point	3 rd point	4 th point	5 th point
N (rpm)	50	100	150	200	250
d_r (rpm)	$2 * 10^{-2}$	$2 * 10^{-2}$	$2 * 10^{-2}$	$2 * 10^{-2}$	$2 * 10^{-2}$
n	4	4	4	4	4
λ_s ($W*m^{-1}*K^{-1}$)	0.48	0.48	0.48	0.48	0.48
ρ_s ($kg*m^{-3}$)	1089.42	1089.42	1089.42	1089.42	1089.42

μ_s (cp)	4.34	4.34	4.34	4.34	4.34
c_{ps} (kJ*kg ⁻¹ *K ⁻¹)	3.1	3.1	3.1	3.1	3.1
Re	5018.06	10036.11	15054.17	20072.22	25090.28
α_s (W*m ⁻² *K ⁻¹)	20437.48	28902.94	35398.76	40874.97	45699.60

In Table B.7 the calculations spreadsheet of Figure 3.18 is shown.

Table B.7: The calculations spreadsheet of overall heat transfer coefficient as a function of the coolant volumetric flow rate.

Title	1 st point	2 nd point	3 rd point	4 th point	5 th point	6 th point	7 th point	8 th point
\dot{V} (m ³ *s ⁻¹)	0	5*10 ⁻⁵	10 ⁻⁴	2*10 ⁻⁴	3*10 ⁻⁴	4*10 ⁻⁴	8.5*10 ⁻⁴	10 ⁻³
α_{cool} (W*m ⁻² *K ⁻¹)	119.72	366.82	615.08	1531.42	2696.2	3774.56	4873.12	5549.73
N (rpm)	150	150	150	150	150	150	150	150
α_s (W*m ⁻² *K ⁻¹)	35398.76	35398.76	35398.76	35398.76	35398.76	35398.76	35398.76	35398.76
λ_{bottom} (W*m ⁻¹ *K ⁻¹)	13.9	13.9	13.9	13.9	13.9	13.9	13.9	13.9
δ (m)	0.003	0.003	0.003	0.003	0.003	0.003	0.003	0.003
α_{bottom} (W*m ⁻² *K ⁻¹)	4633.33	4633.33	4633.33	4633.33	4633.33	4633.33	4633.33	4633.33
$U_{overall}$ (W*m ⁻² *K ⁻¹)	116.32	336.68	426.95	534.79	1626.6	1964.54	2225.69	2356.92

In Figure 3.18, the overall heat transfer coefficient as a function of the coolant volumetric flow rate. $U_{overall}$ is calculated as a function of α_{cool} which is calculated as a function of Nu which can be calculated based on Re by Equation 3.23, Equation 3.24 and Equation 3.25. Re is calculated by Equation 3.19 as a function of u . u is a function of \dot{V} and is calculated by Equation 3.20. Furthermore, in Equation 3.18, α_s and α_{bottom} terms are calculated by Equation 3.33 and Equation 3.34, respectively. In Table A.2.8, the calculations spreadsheet of Figure 4.19 is shown.

Table B.8: The calculations spreadsheet of overall heat transfer coefficient as a function of the scraper rotational speed

Title	1 st point	2 nd point	3 rd point	4 th point	5 th point
N (rpm)	50	100	150	200	250
α_s (W*m ⁻² *K ⁻¹)	35398.76	35398.76	35398.76	35398.76	35398.76
\dot{V} (m ³ *s ⁻¹)	10 ⁻³	10 ⁻³	10 ⁻³	10 ⁻³	10 ⁻³
α_{cool} (W*m ⁻² *K ⁻¹)	5549.73	5549.73	5549.73	5549.73	5549.73
λ_{bottom} (W*m ⁻¹ *K ⁻¹)	13.9	13.9	13.9	13.9	13.9
δ (m)	3*10 ⁻³	3*10 ⁻³	3*10 ⁻³	3*10 ⁻³	3*10 ⁻³
α_{bottom} (W*m ⁻² *K ⁻¹)	4633.33	4633.33	4633.33	4633.33	4633.33
$U_{overall}$ (W*m ⁻² *K ⁻¹)	2247.386	2322.178	2356.93	2378.14	2392.84

In Figure 3.19, the overall heat transfer coefficient as a function of the scraper rotational speed. $U_{overall}$ is calculated as a function of α_s which is calculated as a function of N by Equation 3.33, based on Equation 3.18. Furthermore, in Equation 3.18, α_{cool} and α_{bottom} terms are calculated by Equation 3.26 and Equation 3.34, respectively.

Table B.9 is calculation spreadsheet of T_{out} , \dot{Q}_{cool} and the temperature of T_b as a function of T_{in} .

Table B.9: The calculations spreadsheet of the coolant outlet temperature, the heat flux from the coolant to the solution and the temperature of the inner bottom of crystallizer as a function of the coolant inlet temperature.

Title	1 st point	2 nd point	3 rd point	4 th point	5 th point
T_{in} (°C)	-22	-24	-26	-28	-30
c_{pc} (kJ*kg ⁻¹ *K ⁻¹)	3.09	3.09	3.09	3.09	3.09
ρ_c (kg*m ⁻³)	1090.3	1090.3	1090.3	1090.3	1090.3
\dot{V} (m ³ *s ⁻¹)	0.01	0.01	0.01	0.01	0.01
T_{EUT} (°C)	-21.1	-21.1	-21.1	-21.1	-21.1
N (rpm)	150	150	150	150	150
$U_{overall}$ (W*m ⁻² *K ⁻¹)	3667.7	3667.7	3667.7	3667.7	3667.7
α_s (W*m ⁻² *K ⁻¹)	35398.76	35398.76	35398.76	35398.76	35398.76
T_{out} (°C)	-21.98	-23.99	-25.99	-27.99	-29.99

ΔT_{LN} (°C)	0.89	2.90	4.89	6.89	8.89
\dot{Q}_{cool} (W)	47.89	154.32	260.77	367.32	473.81
T_b (°C)	-21.26	-21.61	-21.97	-22.32	-22.67

Table B.10: The calculations spreadsheet of the coolant outlet temperature, the heat flux from the coolant to the solution and the temperature of the inner bottom of crystallizer as a function of the coolant volumetric flow rate.

Title	1 st point	2 nd point	3 rd point	4 th point	5 th point	6 th point	7 th point	8 th point
\dot{V} (m ³ *s ⁻¹)	5*10 ⁻⁵	10 ⁻⁴	2*10 ⁻⁴	3*10 ⁻⁴	4*10 ⁻⁴	8.5*10 ⁻⁴	10 ⁻³	10 ⁻²
α_{cool} (W*m ⁻² *K ⁻¹)	366.82	476.62	615.08	2696.2	3774.57	4873.12	5549.73	35016.4
ρ_c (kg*m ⁻³)	1090.3	1090.3	1090.3	1090.3	1090.3	1090.3	1090.3	1,090.3
c_{pc} (kJ*kg ⁻¹ *K ⁻¹)	3.09	3.09	3.09	3.09	3.09	3.09	3.09	3.09
A_{cryst} (m)	10 ⁻²	10 ⁻²	10 ⁻²	10 ⁻²	10 ⁻²	10 ⁻²	10 ⁻²	10 ⁻²
T_{in} (°C)	-30	-30	-30	-30	-30	-30	-30	-30
T_{EUT}	-21.1	-21.1	-21.1	-21.1	-21.1	-21.1	-21.1	-21.1

(°C)									
N (rpm)	150	150	150	150	150	150	150	150	150
α_s (W*m ⁻² *K ⁻¹)	35398	35398	35398	35398	35398	35398	35398	35398	35398
T_{out} (°C)	-29.74	-29.84	-29.90	-29.79	-29.81	-29.90	-29.91	-29.91	-29.98
ΔT (°C)	0.25	0.16	0.10	0.20	0.18	0.10	0.09	0.09	0.013
\dot{Q}_{cool} (W)	42.66	54.28	68.20	207.46	249.70	282.84	301.14	301.14	441.93
T_b (°C)	-21.24	-21.28	-21.33	-21.79	-21.93	-22.04	-22.10	-22.10	-22.57

In Table B.10, T_{out} is calculated as a function of \dot{V} by Equation 3.64. According to Equation 3.35, \dot{Q}_{cool} is calculated as function of \dot{V} . T_b which is calculated by Equation 3.65, is a function of \dot{Q}_{cool} which is influenced by \dot{V} .

Table B.11 is calculation spreadsheet of T_{out} , \dot{Q}_{cool} and the temperature of T_b as a function of N .

Table B.11: The calculations spreadsheet of the coolant outlet temperature, the heat flux from the coolant to the solution and the temperature of the inner bottom of crystallizer as a function of the scraper rotational speed

Title	1 st point	2 nd point	3 rd point	4 th point	5 th point
N (rpm)	50	75	100	150	200
α_s (W*m ⁻² *K ⁻¹)	20437.48	25030.7	28902.97	35398.76	40874.97
\dot{V} (m ³ *s ⁻¹)	10 ⁻²	10 ⁻²	10 ⁻²	10 ⁻²	10 ⁻²

ρ_c (kg*m ⁻³)	1090.3	1090.3	1090.3	1090.3	1090.3
c_{pc} (kJ*kg ⁻¹ *K ⁻¹)	3.09	3.09	3.09	3.09	3.09
$U_{overall}$ (W*m ⁻² *K ⁻¹)	1426.67	1445.19	1456.45	1470.04	1478.27
A_{cryst} (m)	10 ⁻²	10 ⁻²	10 ⁻²	10 ⁻²	10 ⁻²
T_{in} (°C)	-30	-30	-30	-30	-30
T_{EUT} (°C)	-21.1	-21.1	-21.1	-21.1	-21.1
T_{out} (°C)	-29.988	-29.9875	-29.9873	-29.987	-29.9868
\dot{Q}_{cool} (W)	405.73	419.59	428.33	439.18	445.81
T_b (°C)	-23.44	-23.07	-22.84	-22.56	-22.38

In Table B.11, T_{out} is calculated as a function of $U_{overall}$ which is influenced by N through α_s , according to Equation 3.64 α_s is computed as a function of N by Equation 3.33. \dot{Q}_{cool} which is a function of logarithmic average of the inlet and outlet temperature of coolant, calculated by 3.32 T_b which is calculated by Equation 3.65, is a function of \dot{Q}_{cool} which is influenced by N .

In Table B.12- B.15, the calculations spreadsheet of Figure 3.23 are shown.

Table B.12: The calculations spreadsheet of the time required to cool down the solution at T=-30°C

Title	1 st point	2 nd point	3 rd point	4 th point	5 th point	6 th point	7 th point	8 th point	9 th point	10 th point
T_{sol} (°C)	20	15	10	5	0	-5	-10	-15	-20	-21.1
T_{cool} (°C)	-30	-30	-30	-30	-30	-30	-30	-30	-30	-30
\dot{V} (m ³ *s ⁻¹)	10 ⁻³	10 ⁻³	10 ⁻³	10 ⁻³	10 ⁻³	10 ⁻³	10 ⁻³	10 ⁻³	10 ⁻³	10 ⁻³
N (rpm)	150	150	150	150	150	150	150	150	150	150
A_{cryst} (m)	10 ⁻²	10 ⁻²	10 ⁻²	10 ⁻²	10 ⁻²	10 ⁻²	10 ⁻²	10 ⁻²	10 ⁻²	10 ⁻²
m (kg)	1	1	1	1	1	1	1	1	1	1
c_{ps} (kJ*kg ⁻¹ *K ⁻¹)	3.10	3.10	3.10	3.10	3.10	3.10	3.10	3.10	3.10	3.10
$U_{overall}$ (W*m ⁻² *K ⁻¹)	2.36	2.36	2.36	2.36	2.36	2.36	2.36	2.36	2.36	2.36
T_{EUT} (°C)	-21.1	-21.1	-21.1	-21.1	-21.1	-21.1	-21.1	-21.1	-21.1	-21.1
t (s)	0	9.93	21.08	33.80	48.60	66.29	88.30	117.41	160.57	173.62

Table B.13: The calculations spreadsheet of the time required to cool down the solution at $T=-29^{\circ}\text{C}$

Title	1 st point	2 nd point	3 rd point	4 th point	5 th point	6 th point	7 th point	8 th point	9 th point	10 th point
T_{sol} ($^{\circ}\text{C}$)	20	15	10	5	0	-5	-10	-15	-20	-21.1
T_{cool} ($^{\circ}\text{C}$)	-29	-29	-29	-29	-29	-29	-29	-29	-29	-29
\dot{V} ($\text{m}^3 \cdot \text{s}^{-1}$)	10^{-3}	10^{-3}	10^{-3}	10^{-3}	10^{-3}	10^{-3}	10^{-3}	10^{-3}	10^{-3}	10^{-3}
N (rpm)	150	150	150	150	150	150	150	150	150	150
A_{cryst} (m)	10^{-2}	10^{-2}	10^{-2}	10^{-2}	10^{-2}	10^{-2}	10^{-2}	10^{-2}	10^{-2}	10^{-2}
m (kg)	1	1	1	1	1	1	1	1	1	1
c_{ps} ($\text{kJ} \cdot \text{kg}^{-1} \cdot \text{K}^{-1}$)	3.10	3.10	3.10	3.10	3.10	3.10	3.10	3.10	3.10	3.10
$U_{overall}$ ($\text{W} \cdot \text{m}^{-2} \cdot \text{K}^{-1}$)	2.36	2.36	2.36	2.36	2.36	2.36	2.36	2.36	2.36	2.36
T_{EUT} ($^{\circ}\text{C}$)	-21.1	-21.1	-21.1	-21.1	-21.1	-21.1	-21.1	-21.1	-21.1	-21.1
t (s)	0	10.15	21.58	34.67	49.97	68.38	91.52	122.65	170.46	185.48

Table B.14: The calculations spreadsheet of the time required to cool down the solution at $T=-28^{\circ}\text{C}$

Title	1 st point	2 nd point	3 rd point	4 th point	5 th point	6 th point	7 th point	8 th point	9 th point	10 th point
T_{sol} ($^{\circ}\text{C}$)	20	15	10	5	0	-5	-10	-15	-20	-21.1
T_{cool} ($^{\circ}\text{C}$)	-28	-28	-28	-28	-28	-28	-28	-28	-28	-28
\dot{V} ($\text{m}^3 \cdot \text{s}^{-1}$)	10^{-3}	10^{-3}	10^{-3}	10^{-3}	10^{-3}	10^{-3}	10^{-3}	10^{-3}	10^{-3}	10^{-3}
N (rpm)	150	150	150	150	150	150	150	150	150	150
A_{cryst} (m)	10^{-2}	10^{-2}	10^{-2}	10^{-2}	10^{-2}	10^{-2}	10^{-2}	10^{-2}	10^{-2}	10^{-2}
m (kg)	1	1	1	1	1	1	1	1	1	1
c_{ps} ($\text{kJ} \cdot \text{kg}^{-1} \cdot \text{K}^{-1}$)	3.10	3.10	3.10	3.10	3.10	3.10	3.10	3.10	3.10	3.10
$U_{overall}$ ($\text{W} \cdot \text{m}^{-2} \cdot \text{K}^{-1}$)	2.36	2.36	2.36	2.36	2.36	2.36	2.36	2.36	2.36	2.36
T_{EUT} ($^{\circ}\text{C}$)	-21.1	-21.1	-21.1	-21.1	-21.1	-21.1	-21.1	-21.1	-21.1	-21.1

Table B.15: The calculations spreadsheet of the time required to cool down the solution at $T=-27^{\circ}\text{C}$

Title	1 st point	2 nd point	3 rd point	4 th point	5 th point	6 th point	7 th point	8 th point	9 th point	10 th point
T_{sol} ($^{\circ}\text{C}$)	20	15	10	5	0	-5	-10	-15	-20	-21.1
T_{cool} ($^{\circ}\text{C}$)	-27	-27	-27	-27	-27	-27	-27	-27	-27	-27
N (rpm)	150	150	150	150	150	150	150	150	150	150
m	1	1	1	1	1	1	1	1	1	1

(kg)										
c_{ps} (kJ*kg ⁻¹ *K ⁻¹)	3.10	3.10	3.10	3.10	3.10	3.10	3.10	3.10	3.10	3.10
$U_{overall}$ (W*m ⁻² *K ⁻¹)	2.36	2.36	2.36	2.36	2.36	2.36	2.36	2.36	2.36	2.36
T_{EUT} (°C)	-21.1	-21.1	-21.1	-21.1	-21.1	-21.1	-21.1	-21.1	-21.1	-21.1
t (s)	0	10.62	22.67	36.56	52.97	73.02	98.80	134.96	196.02	217.564

In Table B.12- B.15, at different T_{cool} , the calculations spreadsheet of T_{sol} over the cooling time which is calculated by Equation 3.40, are shown.

In Table B.16- B.19 the calculations spreadsheet of Figure 4.24 is shown.

Table B.16: The calculations spreadsheet of the time required to cool down the solution at $\dot{V} = 10^{-3} \text{m}^3 \cdot \text{s}^{-1}$

Title	1 st point	2 nd point	3 rd point	4 th point	5 th point	6 th point	7 th point	8 th point	9 th point	10 th point
T_{sol} (°C)	20	15	10	5	0	-5	-10	-15	-20	-21.1
\dot{V} (m ³ *s ⁻¹)	10 ⁻³	10 ⁻³	10 ⁻³	10 ⁻³	10 ⁻³	10 ⁻³	10 ⁻³	10 ⁻³	10 ⁻³	10 ⁻³
T_{cool} (°C)	-30	-30	-30	-30	-30	-30	-30	-30	-30	-30
N (rpm)	150	150	150	150	150	150	150	150	150	150
A_{cryst} (m)	10 ⁻²	10 ⁻²	10 ⁻²	10 ⁻²	10 ⁻²	10 ⁻²	10 ⁻²	10 ⁻²	10 ⁻²	10 ⁻²
m (kg)	1	1	1	1	1	1	1	1	1	1
c_{ps} (kJ*kg ⁻¹ *K ⁻¹)	3.10	3.10	3.10	3.10	3.10	3.10	3.10	3.10	3.10	3.10
T_{EUT}	-21.1	-21.1	-21.1	-21.1	-21.1	-21.1	-21.1	-21.1	-21.1	-21.1

(°C)										
$U_{overall}$ (W*m ⁻² *K ⁻¹)	2357	2357	2357	2357	2357	2357	2357	2357	2357	2357
t (s)	0	9.93	21.08	33.80	48.60	66.29	88.30	117.41	160.57	173.62

Table B.17: The calculations spreadsheet of the time required to cool down the solution at $\dot{V}=5*10^{-3} \text{ m}^3*\text{s}^{-1}$

Title	1 st point	2 nd point	3 rd point	4 th point	5 th point	6 th point	7 th point	8 th point	9 th point
T_{sol} (°C)	20	15	10	0	-5	-10	-15	-20	-21.1
\dot{V} (m ³ *s ⁻¹)	$5*10^{-3}$	$5*10^{-3}$	$5*10^{-3}$	$5*10^{-3}$	$5*10^{-3}$	$5*10^{-3}$	$5*10^{-3}$	$5*10^{-3}$	$5*10^{-3}$
T_{cool} (°C)	-30	-30	-30	-30	-30	-30	-30	-30	-30
N (rpm)	150	150	150	150	150	150	150	150	150
A_{cryst} (m)	10^{-2}	10^{-2}	10^{-2}	10^{-2}	10^{-2}	10^{-2}	10^{-2}	10^{-2}	10^{-2}
m (kg)	1	1	1	1	1	1	1	1	1
c_{ps} (kJ*kg ⁻¹ *K ⁻¹)	3.10	3.10	3.10	3.10	3.10	3.10	3.10	3.10	3.10
T_{EUT} (°C)	-21.1	-21.1	-21.1	-21.1	-21.1	-21.1	-21.1	-21.1	-21.1
$U_{overall}$ (W*m ⁻² *K ⁻¹)	3403	3403	3403	3403	3403	3403	3403	3,403	3,403
t (s)	0	6.79	14.4	33.15	45.14	59.98	79.45	107.81	116.24

Table B.18: The calculations spreadsheet of the time required to cool down the solution at $\dot{V}=0.01 \text{ m}^3*\text{s}^{-1}$

Title	1 st point	2 nd point	3 rd point	4 th point	5 th point	6 th point	7 th point	8 th point	9 th point	10 th point
T_{sol} (°C)	20	15	10	5	0	-5	-10	-15	-20	-21.1

\dot{V} ($\text{m}^3\cdot\text{s}^{-1}$)	10^{-2}	10^{-2}	10^{-2}	10^{-2}	10^{-2}	10^{-2}	10^{-2}	10^{-2}	10^{-2}	10^{-2}
T_{cool} ($^{\circ}\text{C}$)	-30	-30	-30	-30	-30	-30	-30	-30	-30	-30
N (rpm)	150	150	150	150	150	150	150	150	150	150
A_{cryst} (m)	10^{-2}	10^{-2}	10^{-2}	10^{-2}	10^{-2}	10^{-2}	10^{-2}	10^{-2}	10^{-2}	10^{-2}
m (kg)	1	1	1	1	1	1	1	1	1	1
c_{ps} ($\text{kJ}\cdot\text{kg}^{-1}\cdot\text{K}^{-1}$)	3.10	3.10	3.10	3.10	3.10	3.10	3.10	3.10	3.10	3.10
T_{EUT} ($^{\circ}\text{C}$)	-21.1	-21.1	-21.1	-21.1	-21.1	-21.1	-21.1	-21.1	-21.1	-21.1
$U_{overall}$ ($\text{W}\cdot\text{m}^{-2}\cdot\text{K}^{-1}$)	3,667	3,667	3,667	3,667	3,667	3,667	3,667	3,667	3,667	3,667
t (s)	0	6.29	13.35	21.37	30.69	41.78	55.50	73.45	99.56	107.30

Table B.19: The calculations spreadsheet of the time required to cool down the solution at $\dot{V}=5\cdot 10^{-2} \text{ m}^3\cdot\text{s}^{-1}$

Title	1 st point	2 nd point	3 rd point	4 th point	5 th point	6 th point	7 th point	8 th point	9 th point	10 th point
T_{sol} ($^{\circ}\text{C}$)	20	15	10	5	0	-5	-10	-15	-20	-21.1
\dot{V} ($\text{m}^3\cdot\text{s}^{-1}$)	$5\cdot 10^{-2}$	$5\cdot 10^{-2}$	$5\cdot 10^{-2}$	$5\cdot 10^{-2}$	$5\cdot 10^{-2}$	$5\cdot 10^{-2}$	$5\cdot 10^{-2}$	$5\cdot 10^{-2}$	$5\cdot 10^{-2}$	$5\cdot 10^{-2}$
T_{cool} ($^{\circ}\text{C}$)	-30	-30	-30	-30	-30	-30	-30	-30	-30	-30
N (rpm)	150	150	150	150	150	150	150	150	150	150
A_{cryst} (m)	10^{-2}	10^{-2}	10^{-2}	10^{-2}	10^{-2}	10^{-2}	10^{-2}	10^{-2}	10^{-2}	10^{-2}
m (kg)	1	1	1	1	1	1	1	1	1	1
c_{ps} ($\text{kJ}\cdot\text{kg}^{-1}\cdot\text{K}^{-1}$)	3.10	3.10	3.10	3.10	3.10	3.10	3.10	3.10	3.10	3.10
T_{EUT} ($^{\circ}\text{C}$)	-21.1	-21.1	-21.1	-21.1	-21.1	-21.1	-21.1	-21.1	-21.1	-21.1
$U_{overall}$ ($\text{W}\cdot\text{m}^{-2}\cdot\text{K}^{-1}$)	3,969	3,969	3,969	3,969	3,969	3,969	3,969	3,969	3,969	3,969
t (s)	0	5.80	12.31	19.71	28.29	38.51	51.13	67.64	91.57	98.65

The time required to cool down the solution is calculated by Equation 3.40. In Equation 3.40, $U_{overall}$ which is influenced by \dot{V} through α_s , is the only variable to control the cooling time of solution at different \dot{V} .

In Table B.20- B.22 the calculations spreadsheet of Figure 3.251 is shown.

Table B.20: The calculations spreadsheet of the time required to cool down the solution at $N=50$ rpm

Title	1 st point	2 nd point	3 rd point	4 th point	5 th point	6 th point	7 th point	8 th point	9 th point	10 th point
$T_{sol}/^{\circ}\text{C}$	20	15	10	5	0	-5	-10	-15	-20	-21.1
$\dot{V}(\text{m}^3\cdot\text{s}^{-1})$	10^{-3}	10^{-3}	10^{-3}	10^{-3}	10^{-3}	10^{-3}	10^{-3}	10^{-3}	10^{-3}	10^{-3}
N (rpm)	50	50	50	50	50	50	50	50	50	50
T_{cool} ($^{\circ}\text{C}$)	-30	-30	-30	-30	-30	-30	-30	-30	-30	-30
A_{cryst} (m)	10^{-2}	10^{-2}	10^{-2}	10^{-2}	10^{-2}	10^{-2}	10^{-2}	10^{-2}	10^{-2}	10^{-2}
m (kg)	1	1	1	1	1	1	1	1	1	1
c_{ps} ($\text{kJ}\cdot\text{kg}^{-1}\cdot\text{K}^{-1}$)	3.10	3.10	3.10	3.10	3.10	3.10	3.10	3.10	3.10	3.10
T_{EUT} ($^{\circ}\text{C}$)	-21.1	-21.1	-21.1	-21.1	-21.1	-21.1	-21.1	-21.1	-21.1	-21.1
$U_{overall}/(\text{W}\cdot\text{m}^{-2}\cdot\text{K}^{-1})$	2,247	2,247	2,247	2,247	2,247	2,247	2,247	2,247	2,247	2,247
t (s)	0	10.03	21.25	33.97	48.66	66.04	87.3	114.79	153.56	164.7

Table B.21: The calculations spreadsheet of the time required to cool down the solution at $N=100$ rpm

Title	1 st point	2 nd point	3 rd point	4 th point	5 th point	6 th point	7 th point	8 th point	9 th point	10 th point
T_{sol} ($^{\circ}\text{C}$)	20	15	10	5	0	-5	-10	-15	-20	-21.1
$\dot{V}(\text{m}^3\cdot\text{s}^{-1})$	10^{-3}	10^{-3}	10^{-3}	10^{-3}	10^{-3}	10^{-3}	10^{-3}	10^{-3}	10^{-3}	10^{-3}
N (rpm)	100	100	100	100	100	100	100	100	100	100
T_{cool} ($^{\circ}\text{C}$)	-30	-30	-30	-30	-30	-30	-30	-30	-30	-30
A_{cryst} (m)	10^{-2}	10^{-2}	10^{-2}	10^{-2}	10^{-2}	10^{-2}	10^{-2}	10^{-2}	10^{-2}	10^{-2}
m (kg)	1	1	1	1	1	1	1	1	1	1
c_{ps} ($\text{kJ}\cdot\text{kg}^{-1}\cdot\text{K}^{-1}$)	3.10	3.10	3.10	3.10	3.10	3.10	3.10	3.10	3.10	3.10
T_{EUT} ($^{\circ}\text{C}$)	-21.1	-21.1	-21.1	-21.1	-21.1	-21.1	-21.1	-21.1	-21.1	-21.1

$U_{overall}/(W*m^{-2}*K^{-1})$	2322	2322	2322	2322	2322	2322	2322	2322	2322	2322
t (s)	0	9.81	20.79	33.3	47.7	64.8	85.84	113	152.2	163.60

Table B.22: The calculations spreadsheet of the time required to cool down the solution at $N=150$ rpm

Title	1 st point	2 nd point	3 rd point	4 th point	5 th point	6 th point	7 th point	8 th point	9 th point	10 th point
T_{sol} (°C)	20	15	10	5	0	-5	-10	-15	-20	-21.1
\dot{V} (m ³ *s ⁻¹)	10 ⁻³	10 ⁻³	10 ⁻³	10 ⁻³	10 ⁻³	10 ⁻³	10 ⁻³	10 ⁻³	10 ⁻³	10 ⁻³
N (rpm)	150	150	150	150	150	150	150	150	150	150
T_{cool} (°C)	-30	-30	-30	-30	-30	-30	-30	-30	-30	-30
A_{cryst} (m)	10 ⁻²	10 ⁻²	10 ⁻²	10 ⁻²	10 ⁻²	10 ⁻²	10 ⁻²	10 ⁻²	10 ⁻²	10 ⁻²
m (kg)	1	1	1	1	1	1	1	1	1	1
c_{ps} (kJ*kg ⁻¹ *K ⁻¹)	3.10	3.10	3.10	3.10	3.10	3.10	3.10	3.10	3.10	3.10
T_{EUT} (°C)	-21.1	-21.1	-21.1	-21.1	-21.1	-21.1	-21.1	-21.1	-21.1	-21.1
$U_{overall}$ (W*m ⁻² *K ⁻¹)	2,357	2,357	2,357	2,357	2,357	2,357	2,357	2,357	2,357	2,357
t (s)	0	9.93	21.1	33.8	48.6	66.2	88.3	117.4	160.6	173.6

In Equation 3.40, the time required to cool down the solution is influenced by P_s and $U_{overall}$. P_s is calculated based on Equation B.1 as a function of N . $U_{overall}$ is calculated by Equation 3.18 and as a function of α_s which is calculated according to Equation 3.33 and as a function of N .

B.2 Calculations In Crystallizing Condition

In Table B.23 the calculations spreadsheet of Figure 3.26 is shown.

Table B.23: The calculations spreadsheet of the solution physical properties as a function of ice mass fraction

Title	1 st point	2 nd point	3 rd point	4 th point	5 th point	6 th point	7 th point	8 th point
ϕ_m	0	0.05	0.1	0.15	0.2	0.3	0.4	0.5
ρ_i (Kg*m ⁻³)	917	917	917	917	917	917	917	917
ρ_s (Kg*m ⁻³)	1,089	1,089	1,089	1,089	1,089	1,089	1,089	1,089
ρ_{sl} (Kg*m ⁻³)	1089	1,079	1,069	1,059	1,050	1,031	1,013	996
ϕ_v	0	0.06	0.12	0.17	0.23	0.34	0.44	0.54
λ_i (W*m ⁻¹ *K ⁻¹)	2.22	2.22	2.22	2.22	2.22	2.22	2.22	2.22
λ_s (W*m ⁻¹ *K ⁻¹)	0.48	0.48	0.48	0.48	0.48	0.48	0.48	0.48
λ_{sl} (W*m ⁻¹ *K ⁻¹)	0.48	0.53	0.583	0.64	0.69	0.81	0.94	1.09
μ_s (cp)	4.34	4.34	4.342	4.34	4.34	4.34	4.34	4.34
μ_{sl} (cp)	4.34	5.15	6.27	7.73	9.63	16.17	35.85	120.42
c_{pi} (kJ*kg ⁻¹ *K ⁻¹)	2.32	2.32	2.32	2.32	2.32	2.32	2.32	2.32
c_{ps} (kJ*kg ⁻¹ *K ⁻¹)	3.10	3.10	3.10	3.10	3.10	3.10	3.10	3.10
c_{psl} (kJ*kg ⁻¹ *K ⁻¹)	3.10	3.06	3.03	2.99	2.95	2.87	2.79	2.71

In Table B.21, ϕ_m is calculated by Equation 3.42, ρ_{sl} by Equation 3.43, ϕ_v by Equation 3.45, λ_{sl} by Equation 3.46, μ_{sl} by Equation 3.50 and c_{psl} by Equation 3.48.

In Table A.2.24 the calculations spreadsheet of Figure 3.27 is shown.

Table B.24: The calculations spreadsheet of the Reynolds number, Prandtl number, Nusselt number solution heat transfer coefficient and overall heat transfer coefficient as a function of ice mass fraction

Title	1 st point	2 nd point	3 rd point	4 th point	5 th point	6 th point	7 th point	8 th point
ϕ_m	0	0.05	0.1	0.15	0.2	0.3	0.4	0.5
N (rpm)	150	150	150	150	150	150	150	150
\dot{V} (m ³ *s ⁻¹)	10 ⁻³	10 ⁻³	10 ⁻³	10 ⁻³	10 ⁻³	10 ⁻³	10 ⁻³	10 ⁻³
Re_{sl}	271,376	226,600	184,417	148,198	117,866	68,994	30,564	8,943
Pr_{sl}	27.79	29.62	32.53	36.30	41.05	57.15	105.89	298.55
Nu_{sl}	2,814.4	2588.57	2367.31	2,159.85	1,966.8	1,600.6	1,210.9	820.27
α_{sl} (W*m ⁻² *K ⁻¹)	13,125	13,268	13,281	13,215	13,084	12,494	11,004	8,630
$U'_{overall}$ (W*m ⁻² *K ⁻¹)	2,117	2,121	2,121	2,120	2,116	2,100	2,053	1,953

In Table B.24, ϕ_m is calculated by Equation 3.32, Re_{sl} by Equation 3.53, Pr_{sl} by Equation 3.22, Nu_{sl} by Equation 3.55, α_{sl} by Equation 3.56 and $U'_{overall}$ by Equation 3.57.

In Table A.2.25, the calculations spreadsheet of Figure 3.28 is given.

Table B.25: The calculations spreadsheet of the heat flux from the coolant to the solution, the scraper power consumption and the slurry enthalpy as a function of the ice mass fraction.

Title	1 st point	2 nd point	3 rd point	4 th point	5 th point	6 th point	7 th point	8 th point
-------	-----------------------	-----------------------	-----------------------	-----------------------	-----------------------	-----------------------	-----------------------	-----------------------

ϕ_m	0	0.05	0.1	0.15	0.2	0.3	0.4	0.5
N (rpm)	150	150	150	150	150	150	150	150
ρ_{sl} (Kg*m ⁻³)	1089	1,079	1,069	1,059	1,050	1,031	1,013	996
Ne	5	5	5	5	5	5	5	5
d_s (m)	$2 * 10^{-2}$	$2 * 10^{-2}$	$2 * 10^{-2}$	$2 * 10^{-2}$	$2 * 10^{-2}$	$2 * 10^{-2}$	$2 * 10^{-2}$	$2 * 10^{-2}$
\dot{V} (m ³ *s ⁻¹)	10^{-3}	10^{-3}	10^{-3}	10^{-3}	10^{-3}	10^{-3}	10^{-3}	10^{-3}
T_{cool} (°C)	-30	-30	-30	-30	-30	-30	-30	-30
T_{EUT} (°C)	-21.1	-21.1	-21.1	-21.1	-21.1	-21.1	-21.1	-21.1
A (m ²)	10^{-2}	10^{-2}	10^{-2}	10^{-2}	10^{-2}	10^{-2}	10^{-2}	10^{-2}
$U'_{overall}$ (W*m ⁻² *K ⁻¹)	2,117	2,121	2,122	2,120	2,117	2,101	2,054	1,953
H_{fs} (J*g ⁻¹)	50	50	50	50	50	50	50	50
H_{fi} (J*g ⁻¹)	364.5	364.5	364.5	364.5	364.5	364.5	364.5	364.5
\dot{Q}_{cool} (W)	283.22	283.63	283.67	283.48	283.11	281.34	276.17	264.95
P_s (W)	58.83	58.28	57.74	57.21	56.70	55.69	54.71	53.77
H_{fsl} (J*g ⁻¹)	-50	-65.72	-81.45	-97.17	-112.9	-144.35	-175.8	-207.25

In Table B.25, \dot{Q}_{cool} is calculated by Equation 3.38 at the eutectic temperature, P_s by Equation B.1 and H_{fsl} by Equation 3.47.

B.3 Effect of coolant temperature, coolant volumetric flow rate and scraper rotational speed on ice production

In Table B.26- B.29, the calculations spreadsheet of Figure 3.29 is shown.

Table B.26: The time required to produce various amounts of ice crystals at $T_{cool}=-30^\circ\text{C}$

Title	1 st point	2 nd point	3 rd point	4 th point	5 th point	6 th point	7 th point	8 th point
m_c (g)	0	50	100	150	200	300	400	500
m_t (g)	1000	1000	1000	1000	1000	1000	1000	1000

T_{cool} (°C)	-30	-30	-30	-30	-30	-30	-30	-30	-30
N (rpm)	150	150	150	150	150	150	150	150	150
ρ_{sl} (Kg*m ⁻³)	1048	1048	1048	1048	1048	1048	1048	1048	1048
Ne	5	5	5	5	5	5	5	5	5
d_s (m)	$2 * 10^{-2}$	$2 * 10^{-2}$	$2 * 10^{-2}$	$2 * 10^{-2}$	$2 * 10^{-2}$	$2 * 10^{-2}$	$2 * 10^{-2}$	$2 * 10^{-2}$	$2 * 10^{-2}$
\dot{V} (m ³ *s ⁻¹)	10^{-3}	10^{-3}	10^{-3}	10^{-3}	10^{-3}	10^{-3}	10^{-3}	10^{-3}	10^{-3}
A (m ²)	10^{-2}	10^{-2}	10^{-2}	10^{-2}	10^{-2}	10^{-2}	10^{-2}	10^{-2}	10^{-2}
$U'_{overall}$ (W*m ⁻² *K ⁻¹)	2120	2120	2120	2120	2120	2120	2120	2120	2120
T_{EUT} (°C)	-21.1	-21.1	-21.1	-21.1	-21.1	-21.1	-21.1	-21.1	-21.1
\dot{Q}_{cool} (W)	279.94	279.94	279.94	279.94	279.94	279.94	279.94	279.94	279.94
P_s (W)	56.62	56.62	56.62	56.62	56.62	56.62	56.62	56.62	56.62
H_{fs} (J*g ⁻¹)	50	50	50	50	50	50	50	50	50
H_{fi} (J*g ⁻¹)	364.5	364.5	364.5	364.5	364.5	364.5	364.5	364.5	364.5
t (s)	0	7.36	18.23	32.63	50.55	96.95	157.43	232	

Table B.27: the time required to produce various amounts of ice crystals at $T_{cool}=-29^\circ\text{C}$

Title	1 st point	2 nd point	3 rd point	4 th point	5 th point	6 th point	7 th point	8 th point
m_c (g)	0	50	100	150	200	300	400	500
m_t (g)	1000	1000	1000	1000	1000	1000	1000	1000
T_{cool} (°C)	-29	-29	-29	-29	-29	-29	-29	-29
N (rpm)	150	150	150	150	150	150	150	150
ρ_{sl} (kg*m ⁻³)	1048	1048	1048	1048	1048	1048	1048	1048
Ne	5	5	5	5	5	5	5	5
d_s (m)	$2 * 10^{-2}$	$2 * 10^{-2}$	$2 * 10^{-2}$	$2 * 10^{-2}$	$2 * 10^{-2}$	$2 * 10^{-2}$	$2 * 10^{-2}$	$2 * 10^{-2}$
\dot{V} (m ³ *s ⁻¹)	0.001	0.001	0.001	0.001	0.001	0.001	0.001	0.001

A / m^2	10^{-2}	10^{-2}	10^{-2}	10^{-2}	10^{-2}	10^{-2}	10^{-2}	10^{-2}
$U'_{overall}/(\text{W}*\text{m}^{-2}*\text{K}^{-1})$	2120	2120	2120	2120	2120	2120	2120	2120
$T_{EUT}(\text{°C})$	-21.1	-21.1	-21.1	-21.1	-21.1	-21.1	-21.1	-21.1
$H_{fs} (\text{J}*\text{g}^{-1})$	50	50	50	50	50	50	50	50
$H_{fI} (\text{J}*\text{g}^{-1})$	364.5	364.5	364.5	364.5	364.5	364.5	364.5	364.5
$\dot{Q}_{cool}(\text{W})$	257.87	257.87	257.87	257.87	257.87	257.87	257.87	257.87
$P_s (\text{W})$	56.62	56.62	56.62	56.62	56.62	56.62	56.62	56.62
t (s)	0	8.56	21.227	37.98	58.84	112.85	183.24	270.03

Table B.28: The time required to produce various amounts of ice crystals at $T_{cool}=-28\text{°C}$.

Title	1 st point	2 nd point	3 rd point	4 th point	5 th point	6 th point	7 th point	8 th point
m_c (g)	0	50	100	150	200	300	400	500
m_t (g)	1000	1000	1000	1000	1000	1000	1000	1000
T_{cool} (°C)	-28	-28	-28	-28	-28	-28	-28	-28
N (rpm)	150	150	150	150	150	150	150	150
ρ_{sl} ($\text{Kg}*\text{m}^{-3}$)	1048	1048	1048	1048	1048	1048	1048	1048
Ne	5	5	5	5	5	5	5	5
d_s (m)	$2 * 10^{-2}$	$2 * 10^{-2}$	$2 * 10^{-2}$	$2 * 10^{-2}$	$2 * 10^{-2}$	$2 * 10^{-2}$	$2 * 10^{-2}$	$2 * 10^{-2}$
\dot{V} (m^3*s^{-1})	10^{-3}	10^{-3}	10^{-3}	10^{-3}	10^{-3}	10^{-3}	10^{-3}	10^{-3}
A (m^2)	10^{-2}	10^{-2}	10^{-2}	10^{-2}	10^{-2}	10^{-2}	10^{-2}	10^{-2}
$U'_{overall}(\text{W}*\text{m}^{-2}*\text{K}^{-1})$	2120	2120	2120	2120	2120	2120	2120	2120
$T_{EUT}(\text{°C})$	-21.1	-21.1	-21.1	-21.1	-21.1	-21.1	-21.1	-21.1
$\dot{Q}_{cool}(\text{W})$	225.23	225.23	225.23	225.23	225.23	225.23	225.23	225.23
$P_s (\text{W})$	56.62	56.62	56.62	56.62	56.62	56.62	56.62	56.62
$H_{fs} (\text{J}*\text{g}^{-1})$	50	50	50	50	50	50	50	50

H_{fI} (J*g ⁻¹)	364.5	364.5	364.5	364.5	364.5	364.5	364.5	364.5
t (s)	0	10.24	25.39	45.43	70.38	134.97	219.17	322.98

Table B.29: The time required to produce various amounts of ice crystals at $T_{cool}=-27^{\circ}\text{C}$.

Title	1 st point	2 nd point	3 rd point	4 th point	5 th point	6 th point	7 th point	8 th point
m_c (g)	0	50	100	150	200	300	400	500
m_i (g)	1000	1000	1000	1000	1000	1000	1000	1000
T_{cool} (°C)	-27	-27	-27	-27	-27	-27	-27	-27
N /rpm	150	150	150	150	150	150	150	150
ρ_{sl} (Kg*m ⁻³)	1048	1048	1048	1048	1048	1048	1048	1048
Ne	5	5	5	5	5	5	5	5
d_s (m)	$2 * 10^{-2}$	$2 * 10^{-2}$	$2 * 10^{-2}$	$2 * 10^{-2}$	$2 * 10^{-2}$	$2 * 10^{-2}$	$2 * 10^{-2}$	$2 * 10^{-2}$
\dot{V} (m ³ *s ⁻¹)	10^{-3}	10^{-3}	10^{-3}	10^{-3}	10^{-3}	10^{-3}	10^{-3}	10^{-3}
A (m ²)	10^{-2}	10^{-2}	10^{-2}	10^{-2}	10^{-2}	10^{-2}	10^{-2}	10^{-2}
$U'_{overall}$ (W*m ⁻² *K ⁻¹)	2120	2120	2120	2120	2120	2120	2120	2120
T_{EUT} (°C)	-21.1	-21.1	-21.1	-21.1	-21.1	-21.1	-21.1	-21.1
\dot{Q}_{cool} (W)	192.58	192.58	192.58	192.58	192.58	192.58	192.58	192.58
P_s (W)	56.62	56.62	56.62	56.62	56.62	56.62	56.62	56.62
H_{fs} (J*g ⁻¹)	50	50	50	50	50	50	50	50
H_{fI} (J*g ⁻¹)	364.5	364.5	364.5	364.5	364.5	364.5	364.5	364.5
t (s)	0	12.74	31.58	56.51	87.54	167.89	272.63	401.75

In Table B.26- B.29, the time required to produce the specific amounts of ice crystals is calculated at different T_{cool} by Equation 3.63. In Equation 3.63, \dot{Q}_{cool} is calculated by Equation 3.38 at the eutectic temperature and P_s by Equation A.2.1. Also, $U'_{overall}$ is computed by Equation 3.57.

In Table A.2.30-A.2.33, the calculations spreadsheet of Figure 3.30 is shown.

Table B.30: Time required to produce various amounts of ice crystals at $\dot{V}=10^{-3}\text{m}^3\text{s}^{-1}$

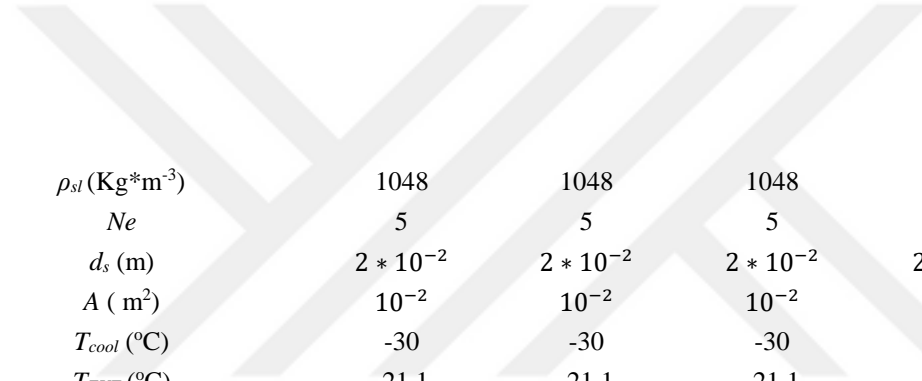
Title	1 st point	2 nd point	3 rd point	4 th point	5 th point	6 th point	7 th point	8 th point
m_c (g)	0	50	100	150	200	300	400	500
m_i (g)	1000	1000	1000	1000	1000	1000	1000	1000
\dot{V} (m^3s^{-1})	10^{-3}	10^{-3}	10^{-3}	10^{-3}	10^{-3}	10^{-3}	10^{-3}	10^{-3}
N (rpm)	150	150	150	150	150	150	150	150
ρ_{sl} ($\text{Kg}\cdot\text{m}^{-3}$)	1048	1048	1048	1048	1048	1048	1048	1048
Ne	5	5	5	5	5	5	5	5
d_s (m)	$2 * 10^{-2}$	$2 * 10^{-2}$	$2 * 10^{-2}$	$2 * 10^{-2}$	$2 * 10^{-2}$	$2 * 10^{-2}$	$2 * 10^{-2}$	$2 * 10^{-2}$
A (m^2)	10^{-2}	10^{-2}	10^{-2}	10^{-2}	10^{-2}	10^{-2}	10^{-2}	10^{-2}
T_{cool} ($^{\circ}\text{C}$)	-30	-30	-30	-30	-30	-30	-30	-30
T_{EUT} ($^{\circ}\text{C}$)	-21.1	-21.1	-21.1	-21.1	-21.1	-21.1	-21.1	-21.1
H_{f1} ($\text{J}\cdot\text{g}^{-1}$)	364.5	364.5	364.5	364.5	364.5	364.5	364.5	364.5
H_{fs} ($\text{J}\cdot\text{g}^{-1}$)	50	50	50	50	50	50	50	50
α_{cool} ($\text{W}\cdot\text{m}^{-2}\cdot\text{K}^{-1}$)	5549	5549	5549	5549	5549	5549	5549	5549
$U'_{overall}$ ($\text{W}\cdot\text{m}^{-2}\cdot\text{K}^{-1}$)	2357	2357	2357	2357	2357	2357	2357	2357
\dot{Q}_{cool} (W)	304.73	304.73	304.73	304.73	304.73	304.73	304.73	304.73
P_s (W)	56.62	56.62	56.62	56.62	56.62	56.62	56.62	56.62
t (s)	0	7.36	18.23	32.63	50.55	96.95	157.43	232

Table B.31: The time required to produce various amounts of ice crystals at $\dot{V}=5*10^{-3}\text{m}^3\text{s}^{-1}$

Title	1 st point	2 nd point	3 rd point	4 th point	5 th point	6 th point	7 th point	8 th point
m_c (g)	0	50	100	150	200	300	400	500
m_i (g)	1000	1000	1000	1000	1000	1000	1000	1000
\dot{V} (m ³ *s ⁻¹)	5*10 ⁻³	5*10 ⁻³	5*10 ⁻³	5*10 ⁻³	5*10 ⁻³	5*10 ⁻³	5*10 ⁻³	5*10 ⁻³
N (rpm)	150	150	150	150	150	150	150	150
ρ_{sl} (Kg*m ⁻³)	1048	1048	1048	1048	1048	1048	1048	1048
Ne	5	5	5	5	5	5	5	5
d_s (m)	2 * 10 ⁻²	2 * 10 ⁻²	2 * 10 ⁻²	2 * 10 ⁻²	2 * 10 ⁻²	2 * 10 ⁻²	2 * 10 ⁻²	2 * 10 ⁻²
A (m ²)	10 ⁻²	10 ⁻²	10 ⁻²	10 ⁻²	10 ⁻²	10 ⁻²	10 ⁻²	10 ⁻²
T_{cool} (°C)	-30	-30	-30	-30	-30	-30	-30	-30
T_{EUT} (°C)	-21.1	-21.1	-21.1	-21.1	-21.1	-21.1	-21.1	-21.1
H_{fI} (J*g ⁻¹)	364.5	364.5	364.5	364.5	364.5	364.5	364.5	364.5
H_{fS} (J*g ⁻¹)	50	50	50	50	50	50	50	50
α_{cool} (W*m ⁻² *K ⁻¹)	20111	20111	20111	20111	20111	20111	20111	20111
$U'_{overall}$ (W*m ⁻² *K ⁻¹)	3404	3404	3404	3404	3404	3404	3404	3404
\dot{Q}_{cool} (W)	440.1	440.1	440.1	440.1	440.1	440.1	440.1	440.1
P_s (W)	56.62	56.62	56.62	56.62	56.62	56.62	56.62	56.62
t (s)	0	4.92	12.20	21.84	33.84	64.89	105.38	155.29

Table B.32: The time required to produce various amounts of ice crystals at $\dot{V}=0.01$ m³*s⁻¹

Title	1 st point	2 nd point	3 rd point	4 th point	5 th point	6 th point	7 th point	8 th point
m_c (g)	0	50	100	150	200	300	400	500
m_i (g)	1000	1000	1000	1000	1000	1000	1000	1000
\dot{V} (m ³ *s ⁻¹)	10 ⁻²	10 ⁻²	10 ⁻²	10 ⁻²	10 ⁻²	10 ⁻²	10 ⁻²	10 ⁻²
N (rpm)	150	150	150	150	150	150	150	150



ρ_{sl} (Kg*m ⁻³)	1048	1048	1048	1048	1048	1048	1048	1048
Ne	5	5	5	5	5	5	5	5
d_s (m)	$2 * 10^{-2}$	$2 * 10^{-2}$	$2 * 10^{-2}$	$2 * 10^{-2}$	$2 * 10^{-2}$	$2 * 10^{-2}$	$2 * 10^{-2}$	$2 * 10^{-2}$
A (m ²)	10^{-2}	10^{-2}	10^{-2}	10^{-2}	10^{-2}	10^{-2}	10^{-2}	10^{-2}
T_{cool} (°C)	-30	-30	-30	-30	-30	-30	-30	-30
T_{EUT} (°C)	-21.1	-21.1	-21.1	-21.1	-21.1	-21.1	-21.1	-21.1
H_{f1} (J*g ⁻¹)	364.5	364.5	364.5	364.5	364.5	364.5	364.5	364.5
H_{fs} (J*g ⁻¹)	50	50	50	50	50	50	50	50
α_{cool} (W*m ⁻² *K ⁻¹)	35016	35016	35016	35016	35016	35016	35016	35016
$U'_{overall}$ (W*m ⁻² *K ⁻¹)	3,668	3,668	3,668	3,668	3,668	3,668	3,668	3,668
\dot{Q}_{cool} (W)	474.23	474.23	474.23	474.23	474.23	474.23	474.23	474.23
P_s (W)	56.62	56.62	56.62	56.62	56.62	56.62	56.62	56.62
t (s)	0	4.56	11.30	20.23	31.33	60.09	97.58	143.80

Table B. 33: The time required to produce various amounts of ice crystals at $\dot{V}=0.05 \text{ m}^3\text{s}^{-1}$

Title	1 st point	2 nd point	3 rd point	4 th point	5 th point	6 th point	7 th point	8 th point
m_c (g)	0	50	100	150	200	300	400	500
m_t (g)	1000	1000	1000	1000	1000	1000	1000	1000
\dot{V} (m ³ *s ⁻¹)	$5*10^{-2}$	$5*10^{-2}$	$5*10^{-2}$	$5*10^{-2}$	$5*10^{-2}$	$5*10^{-2}$	$5*10^{-2}$	$5*10^{-2}$
N (rpm)	150	150	150	150	150	150	150	150
ρ_{sl} (Kg*m ⁻³)	1048	1048	1048	1048	1048	1048	1048	1048
Ne	5	5	5	5	5	5	5	5
d_s (m)	$2 * 10^{-2}$	$2 * 10^{-2}$	$2 * 10^{-2}$	$2 * 10^{-2}$	$2 * 10^{-2}$	$2 * 10^{-2}$	$2 * 10^{-2}$	$2 * 10^{-2}$
A (m ²)	10^{-2}	10^{-2}	10^{-2}	10^{-2}	10^{-2}	10^{-2}	10^{-2}	10^{-2}

T_{cool} (°C)	-30	-30	-30	-30	-30	-30	-30	-30
T_{EUT} (°C)	-21.1	-21.1	-21.1	-21.1	-21.1	-21.1	-21.1	-21.1
H_{fI} (J*g ⁻¹)	364.5	364.5	364.5	364.5	364.5	364.5	364.5	364.5
H_{fs} (J*g ⁻¹)	50	50	50	50	50	50	50	50
$\alpha_{cool}/W*m^{-2}*K^{-1}$	126896	126896	126896	126896	126896	126896	126896	126896
$U'_{overall}(W*m^{-2}*K^{-1})$	3969	3969	3969	3969	3969	3969	3969	3969
$\dot{Q}_{cool}(W)$	513.14	513.14	513.14	513.14	513.14	513.14	513.14	513.14
P_s (W)	56.62	56.62	56.62	56.62	56.62	56.62	56.62	56.62
t (s)	0	4.21	10.44	18.68	28.94	55.50	90.12	132.8

In Table B.30- B.33, the time required to produce the specific amounts of ice crystals is calculated at different \dot{V} by Equation 3.63. In Equation 3.63, \dot{Q}_{cool} is calculated by Equation 3.38 at the eutectic temperature and P_s by Equation B.1. Also, $U'_{overall}$ is computed by Equation 3.57.

In Table B.34- B.36, the calculations spreadsheet of Figure 3.31 is shown.

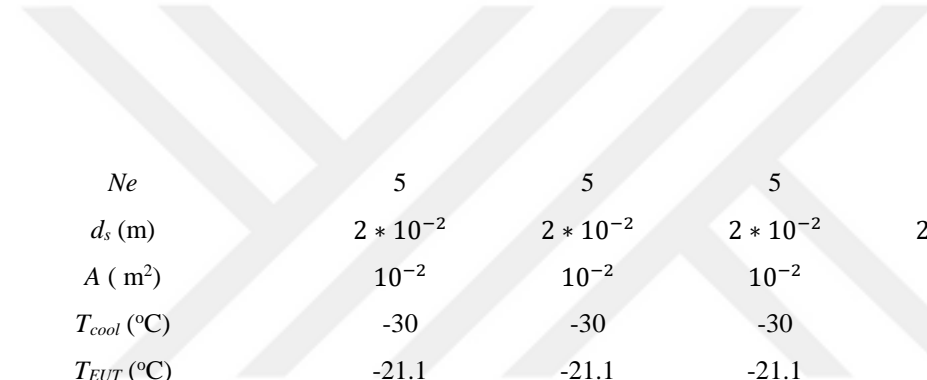
Table B.34: The time required to produce various amounts of ice crystals at $N=150$ rpm

Title	1 st point	2 nd point	3 rd point	4 th point	5 th point	6 th point	7 th point	8 th point
m_c (g)	0	50	100	150	200	300	400	500
m_t (g)	1000	1000	1000	1000	1000	1000	1000	1000
N (rpm)	150	150	150	150	150	150	150	150
$\dot{V}(m^3*s^{-1})$	10^{-3}	10^{-3}	10^{-3}	10^{-3}	10^{-3}	10^{-3}	10^{-3}	10^{-3}
$\rho_{sl}(Kg*m^{-3})$	1048	1048	1048	1048	1048	1048	1048	1048

Ne	5	5	5	5	5	5	5	5
d_s (m)	$2 * 10^{-2}$	$2 * 10^{-2}$	$2 * 10^{-2}$	$2 * 10^{-2}$	$2 * 10^{-2}$	$2 * 10^{-2}$	$2 * 10^{-2}$	$2 * 10^{-2}$
A (m ²)	10^{-2}	10^{-2}	10^{-2}	10^{-2}	10^{-2}	10^{-2}	10^{-2}	10^{-2}
T_{cool} (°C)	-30	-30	-30	-30	-30	-30	-30	-30
T_{EUT} (°C)	-21.1	-21.1	-21.1	-21.1	-21.1	-21.1	-21.1	-21.1
H_{fI} (J*g ⁻¹)	364.5	364.5	364.5	364.5	364.5	364.5	364.5	364.5
H_{fS} (J*g ⁻¹)	50	50	50	50	50	50	50	50
α_{cool} (W*m ⁻² *K ⁻¹)	5,549	5,549	5,549	5,549	5,549	5,549	5,549	5,549
α_{sl} (W*m ⁻² *K ⁻¹)	35016	35016	35016	35016	35016	35016	35016	35016
$U'_{overall}$ (W*m ⁻² *K ⁻¹)	2,357	2,357	2,357	2,357	2,357	2,357	2,357	2,357
\dot{Q}_{cool} (W)	474.23	474.23	474.23	474.23	474.23	474.23	474.23	474.23
P_s (W)	56.62	56.62	56.62	56.62	56.62	56.62	56.62	56.62
t (s)	0	7.36	18.23	32.63	50.55	96.95	157.43	232

Table B.35: The time required to produce various amounts of ice crystals at $N=100$ rpm

Title	1 st point	2 nd point	3 rd point	4 th point	5 th point	6 th point	7 th point	8 th point
m_c (g)	0	50	100	150	200	300	400	500
m_t (g)	1000	1000	1000	1000	1000	1000	1000	1000
N (rpm)	100	100	100	100	100	100	100	100
\dot{V} (m ³ *s ⁻¹)	10^{-3}	10^{-3}	10^{-3}	10^{-3}	10^{-3}	10^{-3}	10^{-3}	10^{-3}
ρ_{sl} (kg*m ⁻³)	1048	1048	1048	1048	1048	1048	1048	1048



Ne	5	5	5	5	5	5	5	5
d_s (m)	$2 * 10^{-2}$	$2 * 10^{-2}$	$2 * 10^{-2}$	$2 * 10^{-2}$	$2 * 10^{-2}$	$2 * 10^{-2}$	$2 * 10^{-2}$	$2 * 10^{-2}$
A (m ²)	10^{-2}	10^{-2}	10^{-2}	10^{-2}	10^{-2}	10^{-2}	10^{-2}	10^{-2}
T_{cool} (°C)	-30	-30	-30	-30	-30	-30	-30	-30
T_{EUT} (°C)	-21.1	-21.1	-21.1	-21.1	-21.1	-21.1	-21.1	-21.1
H_{f1} (J*g ⁻¹)	364.5	364.5	364.5	364.5	364.5	364.5	364.5	364.5
H_{fs} (J*g ⁻¹)	50	50	50	50	50	50	50	50
α_{cool} (W*m ⁻² *K ⁻¹)	5,549	5,549	5,549	5,549	5,549	5,549	5,549	5,549
α_{sl} (W*m ⁻² *K ⁻¹)	28902	28902	28902	28902	28902	28902	28902	28902
$U'_{overall}$ (W*m ⁻² *K ⁻¹)	2,322	2,322	2,322	2,322	2,322	2,322	2,322	2,322
\dot{Q}_{cool} (W)	300.20	300.20	300.20	300.20	300.20	300.20	300.20	300.20
P_s (W)	16.77	16.77	16.77	16.77	16.77	16.77	16.77	16.77
t (s)	0	6.489	16.08	28.78	44.59	85.51	138.86	204.63

Table B.36: The time required to produce various amounts of ice crystals at $N=50$ rpm

Title	1 st point	2 nd point	3 rd point	4 th point	5 th point	6 th point	7 th point	8 th point
m_c (g)	0	50	100	150	200	300	400	500
m_t (g)	1000	1000	1000	1000	1000	1000	1000	1000
N (rpm)	50	50	50	50	50	50	50	50
\dot{V} (m ³ *s ⁻¹)	10^{-3}	10^{-3}	10^{-3}	10^{-3}	10^{-3}	10^{-3}	10^{-3}	10^{-3}
ρ_{sl} (Kg*m ⁻³)	1048	1048	1048	1048	1048	1048	1048	1048
Ne	5	5	5	5	5	5	5	5

d_s (m)	$2 * 10^{-2}$	$2 * 10^{-2}$	$2 * 10^{-2}$	$2 * 10^{-2}$	$2 * 10^{-2}$	$2 * 10^{-2}$	$2 * 10^{-2}$	$2 * 10^{-2}$
A (m ²)	10^{-2}	10^{-2}	10^{-2}	10^{-2}	10^{-2}	10^{-2}	10^{-2}	10^{-2}
T_{cool} (°C)	-30	-30	-30	-30	-30	-30	-30	-30
T_{EUT} (°C)	-21.1	-21.1	-21.1	-21.1	-21.1	-21.1	-21.1	-21.1
H_{fI} (J*g ⁻¹)	364.5	364.5	364.5	364.5	364.5	364.5	364.5	364.5
H_{fs} (J*g ⁻¹)	50	50	50	50	50	50	50	50
α_{cool} (W*m ⁻² *K ⁻¹)	5,549	5,549	5,549	5,549	5,549	5,549	5,549	5,549
α_{sl} (W*m ⁻² *K ⁻¹)	20,437	20,437	20,437	20,437	20,437	20,437	20,437	20,437
$U'_{overall}$ (W*m ⁻² *K ⁻¹)	2,247	2,247	2,247	2,247	2,247	2,247	2,247	2,247
\dot{Q}_{cool} (W)	290.51	290.51	290.51	290.51	290.51	290.51	290.51	290.51
P_s (W)	2.10	2.10	2.10	2.10	2.10	2.10	2.10	2.10
t (s)	0	6.65	16.48	29.50	45.69	87.63	142.30	209.69

In Table B.33- B.35, the time required to produce the specific amounts of ice crystals is calculated at different N by Equation 3.63. In Equation 3.63, \dot{Q}_{cool} is calculated by Equation 3.38 at the eutectic temperature and P_s by Equation B.1. Also, $U'_{overall}$ is computed by Equation 3.57.

CURRICULUM VITAE



Name Surname : **Mohammadreza AKBARKERMANI**

Place and Date of Birth : **Tabriz / 14.05.1992**

E-Mail : **akbarkermani15@itu.edu.tr**
mohammadreza.kermani@gmail.com

EDUCATION :

- **B.Sc.** : 2015, Sahand University of Technology, Chemical Engineering Department
- **M.Sc** : 2019, Istanbul Technical University, Chemical Engineering Department

PROFESSIONAL EXPERIENCE AND REWARDS:

- 2016-2019 ISTANBUL Technical University at the Chemical engineering department, Crystallization Research Center
- 2019 Completed Master at Istanbul Technical University
- Erasmus student at Karlsruhe Institute of Technology (master thesis)
- Supervisor of an undergraduate student in Eutectic Freeze Crystallization of synthetic boric acid project
- Supervisor of an undergraduate student in Evaporative Crystallization of synthetic boric acid project
- Supervisor of two undergraduate student in Eutectic Freeze Crystallization of industrial borax project
- B.Sc. project: Elimination of emerging pollutants from sewage (Case study of Pharmaceutical sewage)
- Internship in Daana Pharmaceutical Company